

RPC User Guide Version 3

RPC_USER_GUIDE.PDF

Prepared by:

Arnaud BETH (coordinator)

Marina GALAND (coordinator)

RPC-ICA

Hans NILSSON (PI)

RPC-IES

Ray GOLDSTEIN
Prachet MOKASHI

RPC-LAP

Anders ERIKSSON (PI)
Fredrik JOHANSSON

RPC-MAG

Ingo RICHTER
Charlotte GOETZ

RPC-MIP

Pierre HENRI (PI)
Xavier VALLIÈRES

RPC-PIU

Chris CARR (PI)
Tony ALLEN

Last revision or compilation: 28/09/2019

Contents

Complementary documentation to the RPC User Guide	3
1 Brief overview of the sensors	4
1.1 The Ion Composition Analyzer (RPC-ICA)	5
1.2 The Ion and Electron Sensor (RPC-IES)	6
1.3 The Langmuir Probe (RPC-LAP)	7
1.4 The Mutual Impedance Probe (RPC-MIP)	8
1.5 The Magnetometer (RPC-MAG)	10
1.6 The Plasma Interface Unit (RPC-PIU)	11
2 Description of the data present in the PSA	13
2.1 Ion energy spectra (RPC-IES and RPC-ICA)	13
2.2 Electron energy spectra (RPC-IES)	16
2.3 Plasma number density (RPC-LAP, RPC-MIP, RPC-ICA and RPC-IES)	16
2.3.1 List of dataset	20
2.3.2 Cross-calibrated products	22
2.3.3 Which solar wind number density should be used?	24
2.3.4 Which cometary plasma number density should be used?	25
2.4 Plasma (ion and electron) velocity and speed (RPC-ICA, RPC-LAP/MIP and RPC-IES)	28
2.4.1 List of dataset	30
2.4.2 Which solar wind velocity should be used?	31
2.4.3 Which cometary ion speed should be used?	35
2.5 Plasma (ion and electron) temperature (RPC-IES and RPC-LAP/MIP)	36
2.5.1 List of dataset	37
2.5.2 Which electron temperature should be used?	38
2.6 Electric field (RPC-LAP and RPC-MIP)	39
2.6.1 List of dataset	40
2.7 Spacecraft potential V_{SC} (RPC-LAP)	40
2.7.1 List of dataset	41
2.8 Magnetic field (RPC-MAG)	41
2.8.1 List of dataset	41
2.9 Illumination maps (RPC-PIU)	43
2.9.1 List of dataset	43
2.9.2 Additional information	45
3 Data, examples and caveats	47
3.1 The Ion Composition Analyzer (RPC-ICA)	47
3.1.1 Science use of the data	47
3.1.2 Example of the dataset	48
3.1.3 List of caveats	50

3.2	The Ion and Electron Sensor (RPC-IES)	50
3.2.1	Science use of the data	50
3.2.2	Example of dataset	50
3.2.3	List of caveats	53
3.3	The Langmuir probe instrument (RPC-LAP)	58
3.3.1	Science use of the data	58
3.3.2	Example of the dataset	59
3.3.3	List of caveats	62
3.4	The Mutual Impedance Probe (RPC-MIP)	64
3.4.1	Science use of the data	64
3.4.2	Example of the dataset	65
3.4.3	List of caveats	67
3.5	The Magnetometer (RPC-MAG)	67
3.5.1	Science use of the data	67
3.5.2	Example of the dataset	69
3.5.3	List of caveats	70
3.6	The Plasma Interface Unit (RPC-PIU): Illumination maps	77
3.6.1	Science use of the data	77
3.6.2	Example of the dataset	77
3.6.3	List of caveats	79
3.7	Rosetta Orbiter Spectrometer for Ion and Neutral Analysis (ROSINA)-Comet Pressure Sensor (COPS)	80
4	Software for visualisation/analysis	82
4.1	Data Formats	82
4.2	AMDA	84
4.3	QSAS	87
4.4	Matlab code for visualisation of illumination maps	96

Complementary documentation to the RPC-User Guide

Table 1: List of relevant documents for each sensor in addition to the RPC User Guide

List of key-documentation (filenames)	Brief description
ICA	
ICA_EAICD.PDF ICA_USER_GUIDE.PDF	Detailed description of the RPC-ICA instrument and data archiving RPC-ICA User Guide
IES	
10991-IES-EAICD-*.PDF FLUX_CALCULATION.PDF MOMENTS_CALCULATION.PDF RPC_IES_UG.PDF	Detailed description of the RPC-IES instrument and data archiving Description of Level 3 flux data and the process used to convert Level 2 counts to flux. Description of Level 5 moments data and the process used to convert Level 3 flux to moments. RPC-IES User Guide
LAP	
RO-IRFU-LAP-EAICD-*.PDF RO-IRFU-LAP-UG.PDF	Detailed description of the RPC-LAP instrument and data archiving RPC-LAP User Guide
MAG	
RO_IGEP_TR0009_EAICD.PDF RO_IGEP_TR0028_CALPROC.PDF RO_IGEP_TR0074_RPCMAG_USERGUIDE.PDF	Detailed description of the RPC-MAG instrument and data archiving Calibration procedure RPC-MAG User Guide
MIP	
RPC-MIP-UG-LPC2E_V*.PDF	RPC-MIP User Guide
MIP-LAP	
RPCMIP_RPCCLAP_CROSSCAL_REPORT.PDF	RPCMIP/RPCLAP Cross-Calibration Report
PIU	
ILLUMINATION_UG.PDF	Detailed description of the illumination maps and their use

Chapter 1

Brief overview of the sensors

The Rosetta Plasma Consortium (RPC) includes five sensors: the Ion and Electron Sensor (IES; Burch et al., 2007), the Ion Composition Analyser (ICA; Nilsson et al., 2007), the Langmuir Probe (LAP; Eriksson et al., 2007), the Mutual Impedance Probe (MIP; Trotignon et al., 2007) and the Magnetometer (MAG; Glassmeier, K.-H. et al., 2007). The joint Plasma Interface Unit (PIU; Carr et al., 2007) acted as instrument control, spacecraft interface, and power management unit.

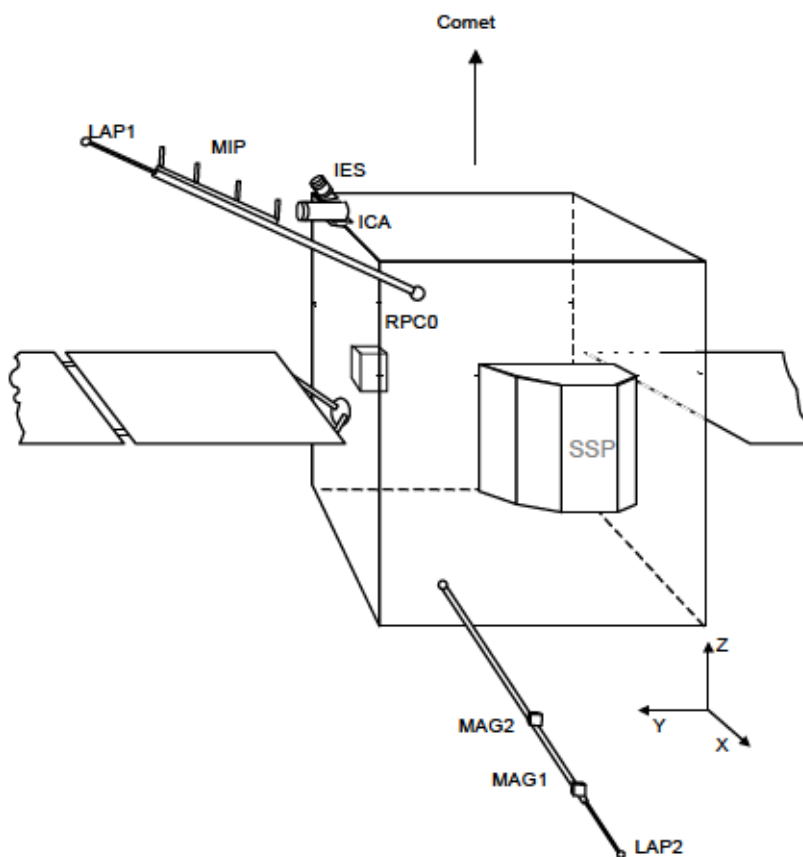


Figure 1.1: Mounting of the RPC sensors on the Rosetta spacecraft. The two LAP probes are seen at the boom tips (updated from Eriksson et al., 2007, courtesy of F. Johansson).

1.1 The Ion Composition Analyzer (RPC-ICA)

RPC-ICA is an ion spectrometer with limited mass resolving capabilities operating in an energy from a few eV up to 40 keV. The instrument has a limited three-dimensional field of view covering approximately 2π sr. RPC-ICA can distinguish between H^+ , He^+ , He^{2+} , and heavy ions of cometary origin with a mass corresponding to water group ions and above. RPC-ICA is described in the instrument paper (Nilsson et al., 2007), though the information in that paper is somewhat outdated. The most important aspects not covered by the instrument paper are:

- The lower energy limit of RPC-ICA is a few eV, not 25 eV as stated in the instrument paper, see also Nilsson et al. (2015a,b) and Odelstad et al. (2017).
- A new way of operating the instrument was introduced during the mission, where RPC-ICA provided two-dimensional data in a restricted energy range of a few eV up to about 100 eV with a temporal resolution of 1 s or 4 s. These modes are described in more detail in Stenberg Wieser et al. (2017).
- In the first few months of the active mission, ICA suffered shut-offs due to high instrument temperature events, which led the team to strongly restrict the operation time of the instrument. Furthermore, RPC-ICA suffered from data corruption leading to lost data and therefore intermittent data coverage. Both these aspects improved with time, so the later in the mission, the less data gaps and better coverage (Nilsson et al., 2015b, 2017).
- For low instrument temperatures, the energy scale may drift (Nilsson et al., 2017).

RPC-ICA has basically only one operational mode. It scans energy and angular space and records detection of ions of different masses. What is called a mode on ICA only relates to the on-board binning of the ion data, which is done in order to reduce the telemetry rate. The data binning is automatically adjusted so that data production stays within available telemetry limits. The data binning in burst mode could be chosen to prioritise mass or angular resolution. Once it was found out that the data corruption giving rise to data loss did not occur for the high angular resolution mode, this was mostly used from summer 2015 onward. The instrument modes of RPC-ICA are described in Table 3 of the RPC-ICA User Guide and in Tables 3 to 5 in the instrument paper (Nilsson et al., 2007).

Independent of the instrument mode, RPC-ICA could also be run using different on-board tables, known internally as different software versions. Of these two stand out, software versions 7 and 8. These two software versions use repeating patterns in the energy table reaching only up to about 100 eV, and fixed elevation values, to achieve two-dimensional data with 32 and 8 energy steps, respectively. This corresponds to 4 s and 1 s temporal resolutions as compared to the standard full energy range 3D distribution in 192 s. Therefore software versions 7 and 8 are necessary to use when studying fast variations in the relatively low energy cometary plasma, whereas they cannot be used to study solar wind dynamics because of the limited energy and angular range. The high time resolution modes were described in Stenberg Wieser et al. (2017). An overview of the full energy and angular range data from the full mission was given in Nilsson et al. (2017). The high time resolution data was regularly used from June 2015 and onward. The ICA mode is a variable in the PSA data, and varies all the time depending on the efficiency of onboard lossless compression and available telemetry. Apart from modes prioritizing mass resolution being used up to May 2015 and thereafter mostly modes prioritizing angular resolution, the use of different modes was just determined by available telemetry, and is not related to any particular mission phases or science goals.

Working with the data is described in more detail in the RPC-ICA User Guide.

1.2 The Ion and Electron Sensor (RPC-IES)

The IES for Rosetta is designed to measure the ion and electron flux as function of energy and direction (Burch et al., 2007). The instrument is an electrostatic analyzer (ESA), featuring electrostatic angular deflection to obtain a field of view of $90^\circ \times 360^\circ$. The instrument objective is to obtain ion and electron distribution functions over the energy range extending from $4.32 \text{ eV}\cdot\text{q}^{-1}$ up to $17.67 \text{ keV}\cdot\text{q}^{-1}$. The angular resolution for electrons is $5^\circ \times 22.5^\circ$ (16 azimuthal and 16 polar-angle sectors). For ions, the angular resolution is $5^\circ \times 45^\circ$ (16 azimuthal and 8 polar-angle sectors) with additional segmentation to $5^\circ \times 5^\circ$ in the 45° polar-angle sector most likely to contain the solar wind (giving a total of 16 polar-angle sectors for ions). The back-to-back top hat geometry of the IES electrostatic analyser allows it to analyse both electrons and positive ions with a single entrance aperture. The IES top hat analysers have toroidal geometry with a smaller radius of curvature in the deflection plane than in the orthogonal plane. This toroidal feature results in a flat deflection plate geometry at the poles of the analysers and has the advantage that the focal point is located outside the analysers rather than within them, as is the case with spherical top hat analysers. Particles within a narrow 8% energy pass band will pass through the analysers and be focused onto the electron and ion microchannel plates (MCPs), which produce charge pulses on 16 discrete anodes, which define the azimuth acceptance angles. In addition, the IES entrance aperture contains electrostatic deflection electrodes, which expand its elevation angle field of view to $\pm 48^\circ$. With the typical top hat polar-angle field of view of 360° , the IES acquires a total solid angle of $4\pi \sin(48^\circ) \approx 2.97 \pi$ steradians.

Operation of IES is controlled by its on-board software in conjunction with sets of (selectable) look up tables. A table in one set determines the sequence of voltages applied to the electrostatic analyzer, thereby selecting the energy/charge of electrons and ions entering the sensor. Likewise, a table in another set determines the sequence of voltages applied to the deflector plates, thereby defining the acceptance angle of the particles. In the typical operating mode, for each deflector voltage chosen the ESA is stepped over its range, the deflector voltage is stepped to its next value, and so on. A complete 2-voltage sequence thus determines a complete measurement cycle. Several versions of each table are stored in the instrument so different operating modes can be easily chosen. In addition, new tables can be uploaded if desired.

During a measurement cycle the instrument obtains a full measurement of ion and electron flux within 16 azimuthal bins, 16 elevation bins and 128 energy bins, for a total of 65536 values ($2 \times 16 \times 16 \times 128$) per measurement. To fit within the data volume allocated to IES, blocks of adjacent angle/energy bins are summed together. The details of this summation are mode-dependent, but this collapse and the 128 or 1024 s accumulation time are the only differences between IES operations in different modes.

During a measurement cycle, the RPC-IES instrument obtains a full measurement of ion and electron counts by sweeping the electrostatic analyzers through 128 energy steps. Within each energy step, the deflectors sweep through 16 elevation steps, and at each step, counts from 16 anodes are recorded simultaneously from the ion and electron detectors. The complete cycle duration takes one of four values – 128 s, 256 s, 512 s or 1024 s with the integration time at each step varying with the cycle duration increases. Additional contingency modes with 96 energy steps were developed and tested in flight, but were not used for acquiring science data.

To fit within the data rates allocated to the instrument, even though data are always acquired over the complete measurement cycle, the range of energy steps for which the counts are returned may be limited. Additionally, counts acquired at discrete adjacent energy steps, elevation

steps and azimuths are summed together and telemetered. The Mode ID of the cycle determines cycle duration, accumulation time, energy range and collapse, elevation range, and azimuth range, and collapse. Mode IDs have three non-zero characters and are specified for each cycle within the data files. Details for each mode are listed as tables in DOCUMENT/IES_MODES directory and CALIB directory which are located in any data IES folder in the RPC-IES folder. The tables list all modes used in flight including modes that were used only for commissioning and special in flight tests. Mode tables were updated during the cruise phase as well as comet phase as needs were realized. The last sets of tables were uplinked on 29 April 2015.

In Level 2 products, cycles with Mode IDs that have four non-zero characters may appear. These infrequently appearing cycles are called transition cycles and are not listed explicitly in mode tables. A transition cycle mode is constructed in-flight when IES switches from a longer duration mode to a shorter mode. It is identified by a four character mode ID. It has the duration of the preceding longer cycle and collapse properties of the following shorter cycle.

Details of IES can be found in the Instrument paper by Burch et al. (2007) and in the EAICD.

1.3 The Langmuir Probe (RPC-LAP)

The purpose of the dual Langmuir probe instrument LAP is the measurement of the plasma density, electron temperature, ion flow speed, spacecraft potential and wave electric field in the plasma around comet 67P and the other targets of the Rosetta mission (Eriksson et al., 2007). Not all these quantities can be accessed at the same time, depending on instrument settings as well as on the plasma parameters.

LAP uses two spherical Langmuir probes (diameter 50 mm) mounted at the tips of the two solid booms protruding non symmetrically from the spacecraft (Figure 1.1). Details of the boom mounting, including coordinates, can be found in the LAP instrument description (Eriksson et al., 2007), together with other technical documentation. The fundamental principle of a Langmuir probe is that the more charged particles there are in the plasma, the more can the probe collect, so the current flowing to the probe is proportional to the plasma density. However, as the probe currents also depend on the energy distribution in the plasma, on the applied bias voltage and on the spacecraft potential (which in turn depends on the density), the interpretation of the data is not always straightforward. It is the prime intention of the LAP sections of this document to guide a prospective user in the art of selecting the most suitable data set for the purpose at hand.

Figure 1.1 shows the mounting of the LAP probes as well as the other RPC sensors on Rosetta and the coordinate axes of the spacecraft coordinate system. The nominal nucleus direction is indicated. To keep the solar panels orthogonal to the Sun, the solar direction is almost always perpendicular to the spacecraft Y axis but may vary in the X-Z plane. This means that LAP2 can sometimes come into shadow behind the spacecraft body or the high gain antenna, and LAP1 behind the solar panels.

The LAP electronics, located inside the RPC common electronics box inside the spacecraft body, can either apply a voltage to each of the probes and measure the resulting current due to plasma particles hitting the probes (or photo- and secondary electrons leaving it), or send a bias current to the probe and measure its voltage. In bias voltage mode, the voltage can be stepped over some range from -30 to $+30$ V in what is known as a probe bias sweep, usually done in a few seconds at intervals which are multiples of 32 s (160 s being the most common). Between these

sweeps, the probes are kept at constant bias voltage, sampling the current at various rates. In an ideal case, the plasma density, electron temperature, ion flow speed, spacecraft potential and photo-electron emission can all be derived from the bias sweeps, and then the current sampled between sweeps can be used to monitor variations of the plasma density at high time resolution (Eriksson et al., 2017; Johansson et al., 2017). The range of currents that can be measured is usually $\pm 10 \mu\text{A}$. A low gain range was sometimes used close to perihelion, spanning $\pm 200 \mu\text{A}$.

The other bias mode, in which a bias current is sent to a probe and its voltage is measured, can be used to monitor the spacecraft potential at high time resolution (Odelstad et al., 2015, 2017). The spacecraft potential depends on the plasma density and can thus be used as a density proxy, with calibration to density values from other sources, like bias voltage sweeps on the other probe or (more typically) the mutual impedance probe instrument RPC-MIP (Engelhardt et al., 2018b; Odelstad et al., 2015). When both probes are in this mode, the difference of their voltages equals the line integral of the electric field between them, so division by the interprobe distance of 5 m gives this component of the electric field. At lowest frequencies, this will be dominated by spurious fields induced by the spacecraft-plasma interaction. There is no firm frequency limit always applicable, but at least for floating probes (zero bias current) in the relatively dense plasma around perihelion the signal appears dominated by the real electric field in the plasma down to surprisingly (given the asymmetry of the boom mounting) low frequencies, below 1 Hz (André et al., 2017; Karlsson et al., 2017). There are no bias current sweeps implemented in the flight software, but the bias currents to the probes were a few times stepped by time-tagged commands.

The LAP electronics allow sampling of all signals at rates up to 18.75 kHz. Due to telemetry (TM) limitations, such high frequency (HF) sampling is available only in short snapshots. Low frequency (LF) sampling can be (almost) continuous, at down-sampled from 57.8 Hz to fit TM availability. LAP has two TM modes: normal mode (NM, 55 bits·s⁻¹) and burst mode (BM, 2.2 kbit·s⁻¹). Resolution is always 16 bits in HF, but some of the LF data at 57.8 Hz have 20 bit resolution. The LAP probes could be operated independently of each other, with the limitation that simultaneous sweeps were not possible. LAP2 could be handed over to MIP for its Long Debye Length mode (LDL), useful for MIP measurements in the plasma density range 50-300 cm⁻³.

1.4 The Mutual Impedance Probe (RPC-MIP)

The purpose of the Mutual Impedance Probe (RPC-MIP) onboard Rosetta is to measure in situ the plasma density (Trotignon et al., 2007).

RPC-MIP is an active electric sensor that measures the transfer impedance between a transmitter (monopole or dipole) and a receiving dipole. The instrument operates at different time resolutions and in different frequency bands comprised in the [7-3500] kHz frequency range. RPC-MIP was operated either in passive mode, i.e., with transmitter(s) off thus acting as a passive electric antenna, or in active mode with transmitter(s) actually stimulates the surrounding plasma. In active mode, different electrodes can be used as a transmitter: 1) two dedicated electrodes on the RPC-MIP bar can be used independently (as monopoles) or conjointly (as a dipole), such operational modes are called SDL (Short Debye Length), 2) the RPC-LAP probe LAP2 can also serve as a monopole transmitter, in such a case the operational modes are then called LDL (Long Debye Length). This latter mode of operations, while preventing RPC-LAP to fully operate, enables to trigger the plasma from a farther distance from the receivers in order to scan larger spatial scales and therefore access plasma densities lower than those measurable

in SDL mode. Reception is always performed by the two receiving dipoles at the edges of the RPC-MIP bar mounted on the upper spacecraft boom.

Measuring the transmission properties of the electric field in the plasma better constrains bulk plasma parameters. From the on-ground analysis of the mutual impedance frequency spectra acquired on-board and depending on plasma conditions (among which the plasma Debye length), one may retrieve plasma bulk properties, such as the electron plasma density and potentially the electron temperature. Given the characteristic plasma conditions encountered by Rosetta and the design of the MIP sensor, while the electron density can be derived from the characteristic features of the RPC-MIP electric spectra (in particular the identification of the electron plasma frequency, upon considerations on the instrument response and hypotheses on the shape of the electron velocity distribution function), it is less straightforward to derive the electron temperature from the MIP active spectra only.

The RPC-MIP instrument can operate in active mode (when transmitting) or in passive mode (no transmission):

- in active mode, a sinusoidal signal is transmitted through one or two electrodes at a given frequency while the potential difference is acquired simultaneously on the dedicated receiving electrodes pair and Fourier transformed at the same frequency as the transmission (through a DFT). Several different transmitting frequencies are then scanned following a frequency table, previously chosen by telecommand. The resulting electric spectra (amplitude and phase) are then fully or partly transferred to data packets. Several transmitting configurations have been implemented:
 - dipole transmission in phase on both RPC-MIP transmitters
 - dipole transmission in phase opposition on both RPC-MIP transmitters
 - monopole transmission on one of the RPC-MIP transmitters
 - monopole transmission on RPC-LAP probe LAP2

Active mode with transmitting RPC-MIP electrodes are referred as SDL (Short Debye Length) modes. Active mode with RPC-LAP probe LAP2 transmission are designated as LDL (Long Debye Length). In SDL mode, the physical length of the RPC-MIP bar prevents from measuring plasma density in plasmas with Debye lengths larger than ~ 50 cm. The LDL mode has been designed to overshoot this limit and access smaller densities.

- in passive mode, no signal is injected and the measured potential difference is processed on-board by a FFT, then obtaining an amplitude spectrum over the whole bandwidth at a 7 kHz frequency resolution. As in active mode, full or part of the information is transmitted to data packets.

Active and passive sub-modes have been designed to adapt on allowed resources or scientific strategies. They result in transferring full or part of the acquired spectra in the telemetry packets and are combined to construct an RPC-MIP sequence with a fixed duration of 32 s (PIU cycle) and a data volume depending on the telemetry mode. A complete description of RPC-MIP sequences, modes and sub-modes is given in the RPC-MIP User Guide.

The frequency range of the RPC-MIP instrument depends on the operating mode. In LDL, spectra are acquired over the [7 - 168] kHz interval while in SDL, spectra can be acquired on several frequency tables, the larger frequency range being [28 - 3472] kHz. The frequency table is selected by telecommand. This results in a working frequency range that can vary with time

(i.e., when changing operating parameters). To prevent users from having a precise knowledge of the instrument operating concepts and parameters, RPC-MIP spectra are always given with the corresponding frequency values in the data files available at PSA. The available frequency tables in the different modes (passive, active: SDL and LDL) are given in the RPC-MIP User Guide.

As different sub-modes can be combined in different ways to construct fixed-length sequences of 32 s, idle periods can exist within a RPC-MIP sequence. This leads to an irregular time resolution that depends on telemetry mode and RPC-MIP operational parameters. Typical values for time resolution for different sub-modes are given in Table 1.1:

Table 1.1: RPC-MIP operational sub-modes and associated time resolution.

	normal TM rate [s]	burst TM rate [s]
survey full	32	~ 4.4
LDL full	~ 10.6	~ 2.6
passive full	32	~ 4.4

All the RPC-MIP operational parameters are described in the RPC-MIP User Guide and can also be found in dedicated files of the PSA archive.

RPC-MIP is fully described in the instrument paper (Trotignon et al., 2007). Working with data is described in details in the RPC-MIP User Guide.

1.5 The Magnetometer (RPC-MAG)

The purpose of the magnetometer is the measurement of the interplanetary magnetic field close to different targets visited by the Rosetta spacecraft.

To measure the magnetic field, a system of two ultra light tri-axial fluxgate magnetometers (about 28 grams each) is used: the outboard (OB) sensor mounted close to the tip of the about 1.55 m long spacecraft boom pointing away from the spacecraft and the inboard (IB) sensor on the same boom about 15 cm closer to the spacecraft body (see Figure 1.1). The OB position on the boom is at 1.48 m, the IB position is at 1.33 m distance from the spacecraft.

In order to provide an exact timing, 6 A/D converters (one for each of the six sensor channels) are used synchronously. The A/D converters have a resolution of 20 bits each. MAG can be operated with a maximum temporal resolution of about 20 vectors-s⁻¹ outboard and 1 vector-s⁻¹ inboard. The raw vectors are transmitted from MAG to PIU with this constant vector rate. PIU is under-sampling and filtering the raw vectors according to the current mode which is set according to the actual telemetry budget available.

RPC-MAG can be characterised by the following features:

- Fluxgate-Magnetometer with a resolution of 31 pT
- Measurement Range: ± 16384 nT
- 2 Sensors: Outboard (OB) / Inboard (IB)
- 6×20 Bit ADCs

- Measuring B-Field in 3 components with a maximum vector rate of 20 Hz.
- The temperature at Outboard and Inboard sensors is monitored in MAG housekeeping data.
- The instrument delivers time series of the 3 dimensional magnetic field components.

The magnetometer is a simple instrument in terms of modes. There are two sensors, the inboard sensor IB and the outboard sensor OB, which are sampled with different sample rates.

All possible operational modes are listed in section 3.4 of the RPC-MAG User Guide. Although there are 6 science modes we only used the NORMAL mode (SID2) and the BURST mode (SID3) during the scientific phases of the mission. This means that the data of the OB sensor are available at a vector rate of 1 Hz (normal mode) or 20 Hz (burst mode). Accordingly, the IB data are sampled at 1/32 Hz and 1 Hz, respectively.

The modes are reflected in the filenames of our data products. Thus a “M2” in the filename means NORMAL mode data and “M3” designates BURST mode data. There is always one data file per sensor per day per mode (if data are available). This means that data files can contain data gaps if mode switches have occurred. If, e.g., the instrument was in NORMAL mode from 07:00–09:00 and from 13:00–24:00 and in BURST mode from 04:00–07:00 and from 09:00–13:00 then the NORMAL mode file contains a gap from 09:00–13:00, whereas the BURST mode file has a gap from 07:00–09:00. All data are there, but they are written to different files in order to avoid mixing different sampling rates and getting wrong results in spectral analyses.

The OB sensor is always sampled with the higher sample rate as this sensor is located further out and should be the one suffering less spacecraft noise.

More details of the RPC-MAG instrument can be found in the Instrument Paper in Glassmeier, K.-H. et al. (2007) and information on how to use (or not) the magnetometer data is described in details in the RPC-MAG User Guide.

1.6 The Plasma Interface Unit (RPC-PIU)

The RPC consortium approach was chosen to simplify the technical interfaces between the five RPC sensors and the spacecraft whilst also minimising the overall mass and power resources. The Plasma Interface Unit (RPC-PIU) provides power-conversion and data-processing functions which are shared by all of the five sensors (Carr et al., 2007). PIU also provides a single-point interface to the spacecraft such that, with regard to telemetry and tele-commanding, the RPC is operated as a single instrument with multiple sub-instruments, each of which can be separately powered, controlled, and operated in numerous sensor-specific modes.

Technical Overview

The Block diagram of the PIU is shown in Figure 4 from Carr et al. (2007). Spacecraft-provided primary power (nominally +28 V) is converted to regulated secondary voltages as required by the sensor units. Per sensor, each voltage line is individually controlled on/off by a switch which senses the current-draw and switches off the entire sensor unit in case of over-current. The switches are also controlled by telecommand. Thus by controlling the power-status of the sensors, the overall power consumption of the RPC can be adjusted to meet operational and

scientific needs.

The PIU processor receives telecommands from the spacecraft on-board data-handling system and – depending on the destination ‘application ID’ in the packet header – either forwards the commands onto the relevant sensor for further processing, or executes the commands within the PIU. Command acknowledgements are returned to the spacecraft. The packet-services protocol is implemented within the PIU, including the patching of instrument (or PIU) onboard software. Telemetry data (housekeeping and science) received from the sensor units is assembled and formatted into packets and transmitted to the spacecraft at a 32 s cadence.

Due to the centralisation of these essential services the PIU design criterion was to avoid any single-point failure-mode propagating to (or from) more than one sensor unit. This required duplication of the power conversion and data-processing units, but not the power switches. At the commissioning of RPC the redundant power converter was tested and found to be non-operational. Consequently, the main power converter (and main data-processor) was used throughout the mission, and this failure had no operational impact.

More details on the PIU design and the consortium approach may be found in the RPC instrument paper (Carr et al., 2007).

Illumination maps on the cometary surface

RPC-PIU provides a quite uncommon dataset: the illumination maps. Over the two-year escort phase, the images from the navigation camera NAVCAM have been used to create a shape model of 67P, i.e., a polyhedron of which the shape is the closest one of 67P shape. From this shape model, the RPC-PIU team has been able to reproduce the conditions of illumination, met at 67P because a continuous visual monitoring of the comet was not possible. This tool allows to visualise for example which part of the comet was illuminated at a given time of observation. This dataset is of particular interest when the neutral density is not available as it shows which parts of the comet are active and quantitative information on the percentage of the area which is illuminated is provided. There is no current publications about the generation of this dataset but a few papers have used them.

Further information on the shape model, illumination maps (format, filename) and data products is provided in Section 2.9 and the Illumination map User Guide (located in the NAVCAM directory of the PSA).

Chapter 2

Description of the data present in the PSA

The full RPC-IES dataset is available here:

<ftp://psa.esac.esa.int/pub/mirror/INTERNATIONAL-ROSETTA-MISSION/RPCIES/>

The full RPC-ICA dataset is available here:

<ftp://psa.esac.esa.int/pub/mirror/INTERNATIONAL-ROSETTA-MISSION/RPCICA/>

The full RPC-LAP dataset is available here:

<ftp://psa.esac.esa.int/pub/mirror/INTERNATIONAL-ROSETTA-MISSION/RPCLAP/>

The full RPC-MAG dataset is available here:

<ftp://psa.esac.esa.int/pub/mirror/INTERNATIONAL-ROSETTA-MISSION/RPCMAG/>

The full RPC-MIP dataset is available here:

<ftp://psa.esac.esa.int/pub/mirror/INTERNATIONAL-ROSETTA-MISSION/RPCMIP/>

The full RPC-PIU illumination map dataset is available here:

<ftp://psa.esac.esa.int/pub/mirror/INTERNATIONAL-ROSETTA-MISSION/NAVCAM/>

2.1 Ion energy spectra (RPC-IES and RPC-ICA)

RPC-IES: the range and the resolution of ion data acquired by the RPC-IES instrument are described below. The actual range and the resolution of the data within the data files listed in this section are mode-dependent and may be restricted due the telemetry limitations as described in Section 1.2. Further details can be found in the EAICD and the instrument paper (Burch et al., 2007). Note that the ion energy is also influenced by the spacecraft potential; negative values for the latter yield a shift towards higher energies for the positive ions.

Overview of RPC-IES ion spectrometer:

- Energy range: $4.32 \text{ eV}\cdot\text{q}^{-1}$ to $17.67 \text{ keV}\cdot\text{q}^{-1}$ using 124 steps with 4 additional steps for flyback
- Energy resolution ($\Delta E/E$): 8% at each step
- Elevation range: -45° to $+45^\circ$ from midpoint to midpoint (or -48° to $+48^\circ$ from the minimum of the first bin to maximum of the last bin) over 16 bins (cf. CALIB/ELEVATION_ANGLES.TAB)
- Elevation resolution: 5° nominal, more likely 6° (cf. CALIB/ELEVATION_ANGLES.TAB)

Table 2.1: List of IES deliverables from ion data.

Ion energy distribution				
Name	Unit	Sensor	Level	Brief description
IES Ion counts	counts (ions)	IES/ION	L2	Raw ion counts PSA folder: RO-{TT}-RPCIES-2-{pppp}-V{v}.0 Data files: RPCIES{YYYYDOY}_ION_V{v}.TAB
IES Ion Differential Energy Flux	ions·m ⁻² ·s ⁻¹ ·sr ⁻¹ ·(eV·eV ⁻¹)	IES/ION	L3	Calibrated differential energy flux of ions PSA folder: RO-{TT}-RPCIES-3-{pppp}-V{v}.0 Data files: RPCIES{YYYYDOY}_L3ION_FLUX_V{v}.TAB
Uncertainty in ion differential energy flux	ions·m ⁻² ·s ⁻¹ ·sr ⁻¹ ·(eV·eV ⁻¹)	IES/ION	L3	Uncertainty in the calculation of differential energy flux of ions PSA folder: RO-{TT}-RPCIES-3-{pppp}-V{v}.0 Data files: RPCIES{YYYYDOY}_L3ION_FXUN_V{v}.TAB

- Azimuthal range: 0° to 360° using 16 anodes read simultaneously (cf. CALIB/AZIMUTHAL_ANGLES.TAB)
- Azimuthal resolution: 5° for fine anodes (3 to 11) and 45° for coarse anodes (0 to 2 and 12 to 15) (cf. CALIB/AZIMUTHAL_ANGLES.TAB)

Some of these values may differ from those listed in Burch et al. (2007). The values listed here are based on the instrument as built.

RPC-ICA: measures ions in the energy range from a few eV up to 40 keV per charge (eV·q⁻¹). RPC-ICA can distinguish ions of a mass per charge of 1, 2, 4, 8 and 16 and above. The energy resolution ($\Delta E/E$) is 7%. The angular resolution is 22.5° × 5°. ICA has a 360° field of view in its central plane, and electrostatic deflection provides angular coverage of about ±45° out of that plane in 16 steps of about 5.6°. The 3D temporal resolution of RPC-ICA is 192 s. The instrument can also be used to obtain 2D data with an energy range up to about 100 eV with 1 s or 4 s resolution.

Table 2.3: List of ICA deliverables

Ion energy distribution				
Name	Unit	Sensor	Level	Brief description
ICA raw data	counts per acquisition period	ICA	L2	Raw energy spectrograms for different mass channels, and angular directions. Time resolution: 1, 4 or 192 s. PSA folder: RAW Data files: RPCICA{YYYYMMDD}T{hh}_{xxx}_L2.TAB where xxx is a running number increasing if there are several data files for the same hour, usually due to a change of software version.
ICA differential flux	$\text{ions}\cdot\text{cm}^{-2}\cdot\text{s}^{-1}\cdot\text{sr}^{-1}\cdot\text{eV}^{-1}$	ICA	L3	Calibrated energy spectrograms for different mass channels, and angular directions. Time resolution: 1, 4 or 192 s. PSA folder: CALIBRATED Data files: RPCICA{YYYYMMDD}T{hh}_{xxx}_L3.TAB
ICA cleaned differential energy spectra	$\text{ions}\cdot\text{cm}^{-2}\cdot\text{s}^{-1}\cdot\text{sr}^{-1}\cdot\text{eV}^{-1}$	ICA	L4	Calibrated energy spectrograms for different mass channels, and angular directions. Corrected for cross talk, different on-board noise reduction settings. Time resolution: 1, 4 or 192 s. PSA folder: L4 CORR Data files: RPCICA{YYYYMMDD}T{hh}_{xxx}_L4.TAB
ICA mass separated data	$\text{ions}\cdot\text{cm}^{-2}\cdot\text{s}^{-1}\cdot\text{sr}^{-1}\cdot\text{eV}^{-1}$	ICA	L4	Calibrated energy spectrograms for different physical ion mass ranges, and angular directions. A conservative approach was used, so if there was any uncertainty in the ion mass, the corresponding data was removed. Time resolution: 1, 4 or 192 s. PSA folder: L4 PHYS-MASS Data files RPCICA{YYYYMMDD}T{hh}_{xxx}_L4_{l}.TAB Index {l} indicates the ion mass, H, He2, He or HVY (for heavy or cometary ions).

2.2 Electron energy spectra (RPC-IES)

The range and the resolution of electron data acquired by the IES instrument are described below. The actual range and the resolution of the data within the data files listed in this section are mode-dependent and may be restricted due the telemetry limitations as described in Section 1.2. Further details can be found in the EAICD and the instrument paper (Burch et al., 2007). Note that the electron energy is also influenced by the spacecraft potential; negative values for the latter yield a shift towards lower energies for the electrons. Correction for the spacecraft potential on both the electron energy and energy flux is described in Section 3.2.3.

Overview of RPC-IES electron spectrometer:

- Energy range: $4.32 \text{ eV}\cdot\text{q}^{-1}$ to $17.67 \text{ keV}\cdot\text{q}^{-1}$ using 124 steps with 4 additional steps for flyback
- Energy resolution ($\Delta E/E$): 8% at each step
- Elevation range: from -48° (minimum elevation of the first bin) to $+48^\circ$ (maximum elevation of the last bin) using 16 steps (cf. CALIB/ELEVATION_ANGLES.TAB)
- Elevation resolution: 5° nominal, more likely 6° (cf. CALIB/ELEVATION_ANGLES.TAB)
- Azimuthal range: 0° to 360° using 16 anodes read simultaneously (cf. CALIB/AZIMUTHAL_ANGLES.TAB)
- Azimuthal resolution: 22.5° (cf. CALIB/AZIMUTHAL_ANGLES.TAB)

Some of these values may differ from those listed in Burch et al. (2007). The values listed here are based on the instrument as built.

2.3 Plasma number density (RPC-LAP, RPC-MIP, RPC-ICA and RPC-IES)

This section summarises and clarifies the measurements from the different plasma instruments. Each RPC instrument probes different plasma populations (e.g., cold/warm electrons, energetic electrons, cometary ions, solar wind ions) which are associated with different energy ranges. The goal is to identify which sensor (or combination of sensors) is the most suitable for a given data period.

Below is a brief summary of the pros and cons of the different sensors:

- **RPC-MIP:** it provides the electron number density by identifying the plasma resonance frequency f_p in the mutual impedance spectrum, i.e., the response of the plasma to a weak transmitted electric signal. As f_p depends on no other plasma parameter than the number density, this method is considered to provide the most accurate RPC density estimate, for the density range in which MIP can operate. These are limitation at both high and low number density. When the Debye length gets smaller or close to the distance between the transmitters and the receivers, the RPC-MIP experiment becomes blind to the plasma. For instance, in the case of 7 eV electrons and in LDL mode, this lower threshold is $\sim 50 \text{ cm}^{-3}$. The operating frequency range of the instrument is also limited (see Section 1.4). For instance, in LDL mode limited to [7; 168] kHz, plasma densities higher than $\sim 350 \text{ cm}^{-3}$ cannot be detected.

Table 2.5: List of IES deliverables from electron data

Electron energy distribution				
Name	Unit	Sensor	Level	Brief description
IES Electron counts	counts (electrons)	IES/ELC	L2	Raw electron counts PSA folder: RO-{TT}-RPCIES-2-{pppp}-V{v} Data files: RPCIES{YYYYDOY}_ELC_V{v}.TAB
IES Electron Differential Energy Flux	electrons· $m^{-2}·s^{-1}·sr^{-1}·$ (eV·eV ⁻¹)	IES/ELC	L3	Calibrated differential energy flux of electrons (not corrected for the spacecraft potential) PSA folder: RO-{TT}-RPCIES-3-{pppp}-V{v} Data files: RPCIES{YYYYDOY}_L3ELC_FLUX_V{v}.TAB
Uncertainty in electron differential energy flux	electrons· $m^{-2}·s^{-1}·sr^{-1}·$ (eV·eV ⁻¹)	IES/ELC	L3	Uncertainty in the calculation of differential energy flux of ions PSA folder: RO-{TT}-RPCIES-3-{pppp}-V{v} Data files: RPCIES{YYYYDOY}_L3ELC_FXUN_V{v}.TAB

- **Major strength:** Absolute number density values; not sensitive to V_{SC}
- **Major limitation:** Operational over a range of n_e (both lower and upper bounded)
- **RPC-LAP:** it has several methods to derive the number electron density. Only the bias voltage sweeps provide an absolute value, based on the collection of electrons, as electron temperature can be independently measured if in a suitable range (eV). Continuous sampling of probe current or voltage between sweeps needs absolute calibration by sweeps or MIP on case by case basis to bring uncertainty down to a factor-of-two level. The spacecraft potential V_{SC} can be determined also in very tenuous plasmas, but needs calibration to other density measurements to provide absolute values.
 - **Major strength:** Wide dynamic range, from a few to ten of thousands of cm^{-3} by various methods
 - **Major limitation:** Uncertainties in the absolute values (growing large outside the 10-1000 cm^{-3} range)
- **RPC-MIP/LAP:** it provides the plasma number density by cross-calibrating the RPC-LAP ion current and floating potential measurements to the RPC-MIP plasma densities. This dataset overcomes the instrumental and/or operational limits of RPC-MIP and RPC-LAP and enables reaching a much higher time resolution (up to 17 ms, corresponding to RPC-LAP ion current or floating potential measurements) than densities derived from RPC-MIP mutual impedance spectra (up to 2.5 s) or from RPC-LAP I-V sweeps (64 s). This RPCMIP/RPCLAP dataset is obtained through a dedicated procedure described in the RPCMIP/RPCLAP cross-calibration report.
 - **Major strength:** High time resolution density measurements (17 ms)

- **Major limitation:** Measurements obtained by making assumptions on the plasma behavior
- **RPC-LAP/MIP** two products are available. See Section 2.3.1 and 2.3.4.
- **RPC-ICA:** It is possible to calculate the different moments of the ion distribution function (esp., number density, moment of order 0) from ICA observations for velocities above about 4 eV kinetic drift energy. As the instrument is not boom-mounted like LAP and MIP, the negative (typically -10 – -20 V) spacecraft potential V_{SC} complicates the observations of low energy ions, in particular concerning the direction which may be strongly affected by the spacecraft potential. ICA number densities are best in tenuous plasmas like the solar wind, provided that a directed ion stream falls within the instrument field of view (FoV). This is often but not always the case, as the spacecraft itself blocked the Sun or the comet a few times.
 - **Major strength:** Number density estimates at low density; best for cometary or solar wind ions at large cometocentric distances.
 - **Major limitation:** Field of view and V_{SC} issues
- **RPC-IES:** It is possible to calculate the different moments of the electron and ion distribution functions (esp., number density, moment of order 0) from the electron or ion sensor. For L5 dataset, the method to derive the different moments (e.g., number density, velocity, and temperature) is a simple numerical integration of the distribution function probed by IES (refer to the documentation in the IES dataset). The ion sensor has FoV issues (see Fig. 3.6) often stronger than ICA as the Sun and nucleus often are at the edge of the FoV. When the spacecraft potential V_{SC} is low (in absolute value), i.e., in tenuous plasmas like the solar wind, the IES electron sensor should be able to acquire the full plasma density. When V_{SC} is more negative (during most of the escort phase), electrons at low energy cannot reach IES so the electron number density is underestimated and uncertainty grows large. Here the moments have been derived from electron differential energy fluxes not corrected to the spacecraft potential
 - **Major strength:** Number density estimates at low electron density (assuming low magnitude for the spacecraft potential)
 - **Major limitation:** Field of view and V_{SC} issues, limitation on the detection of low energy ions/electrons. Different electron populations (solar wind, cometary, etc.) are not separated in the moments data files.

Fig. 2.1 and 2.2 provide a rough overview between instruments in terms of the working range or where most of observations have been made. For instance:

- **RPC-MIP:** the electron number density from RPC-MIP results from the full escort phase analysis, on the basis of two different operational modes: SDL and LDL. In SDL, RPC-MIP accesses the plasma (electron) density in the range $[10-10^5] \text{ cm}^{-3}$, in the limit of $T_e[\text{eV}] < 0.05 n_e [\text{cm}^{-3}]$. In LDL, the instrument access the plasma (electron) density in the range $[1-350] \text{ cm}^{-3}$ in the limit of $T_e[\text{eV}] < 0.15 n_e [\text{cm}^{-3}]$. These instrumental limits are indicated in Fig. 2.2.
- **RPC-LAP** The large magenta box in Fig. 2.2 corresponds to the data in the NPL.TAB files, with limits derived from comparison to MIP for densities above 10 cm^{-3} and to solar wind statistics at lower values. The two small boxes refer to the plasma density derived from probe bias sweeps in the ASW.TAB files, with the upper box corresponding to a nominal

$T_e = 5$ eV assumption and the lower box to $T_e = 0.1$ eV used in case cold electrons are detected.

- **RPC-IES:** The limits are instrumental. The lower bound is estimated from the noise, depending on the MCP efficiency, and the upper bound from the maximum count-rate that the system can deliver. Moreover, there is a strong limitation due to the spacecraft potential which limits the detection of low energy electrons.
- **RPC-ICA** is directly constrained from the instrument performance and gives the limits at which ICA is reliable. The spacecraft potential affects however the energy and flux of (low energy) cometary ions (though not their detection).

The spacecraft potential has been over-plotted to highlight the associated limits of some instruments (e.g., RPC-IES and RPC-ICA). Indeed, during the escort phase, most of the time, the spacecraft potential was negative. A negative spacecraft potential: 1) repels and prevents electrons of energy E lower than $|qV_{SC}|$ to reach the instrument, 2) accelerates ions and provides an additional kinetic energy to the ions of the order of $|qV_{SC}|$.

We would also like to point out that the definition of energy is not the same for ions and electrons:

- for ions, “energy” mainly corresponds to the mean kinetic energy from the mean velocity vector, or bulk velocity
- for electrons, “energy” mainly corresponds to the mean thermal energy or the dispersion around the mean velocity vector.

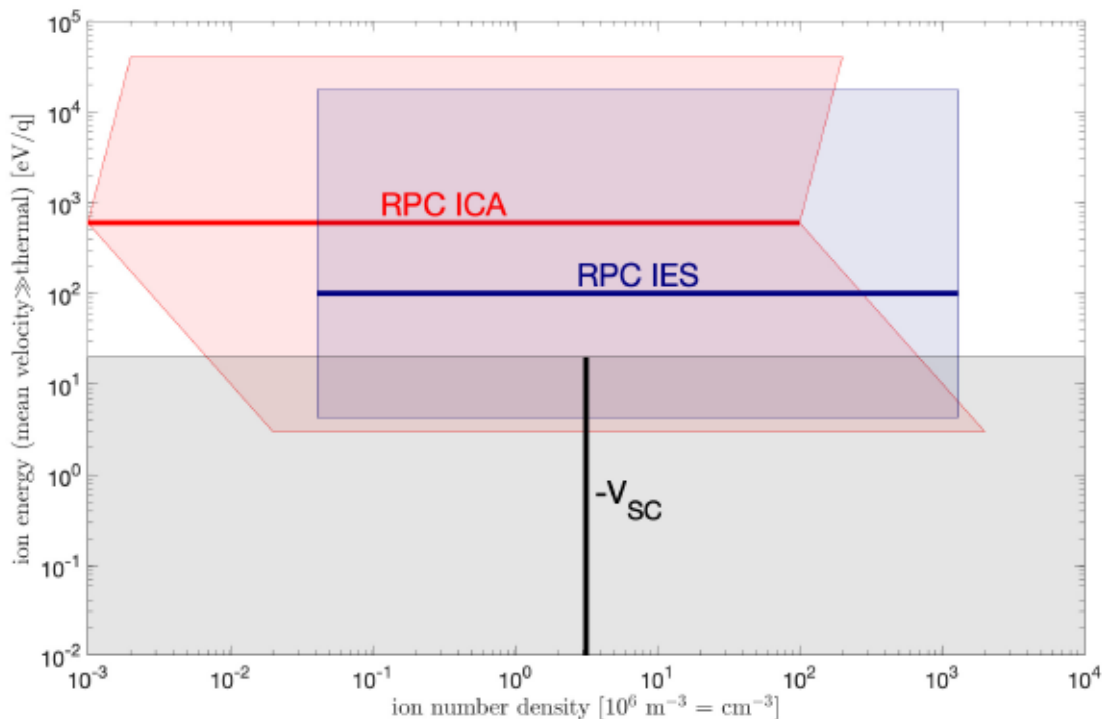


Figure 2.1: (Red) ICA: limits are based on the instrument abilities (lowest reliable count on the lower side, risk of saturation on the upper side), though ICA never reached saturation. (Blue) IES: limits have been derived from the instrumental performance. A typical value of the spacecraft potential has been over-plotted in grey (-20 V) but it is not representative of its variability or largest value throughout the mission.

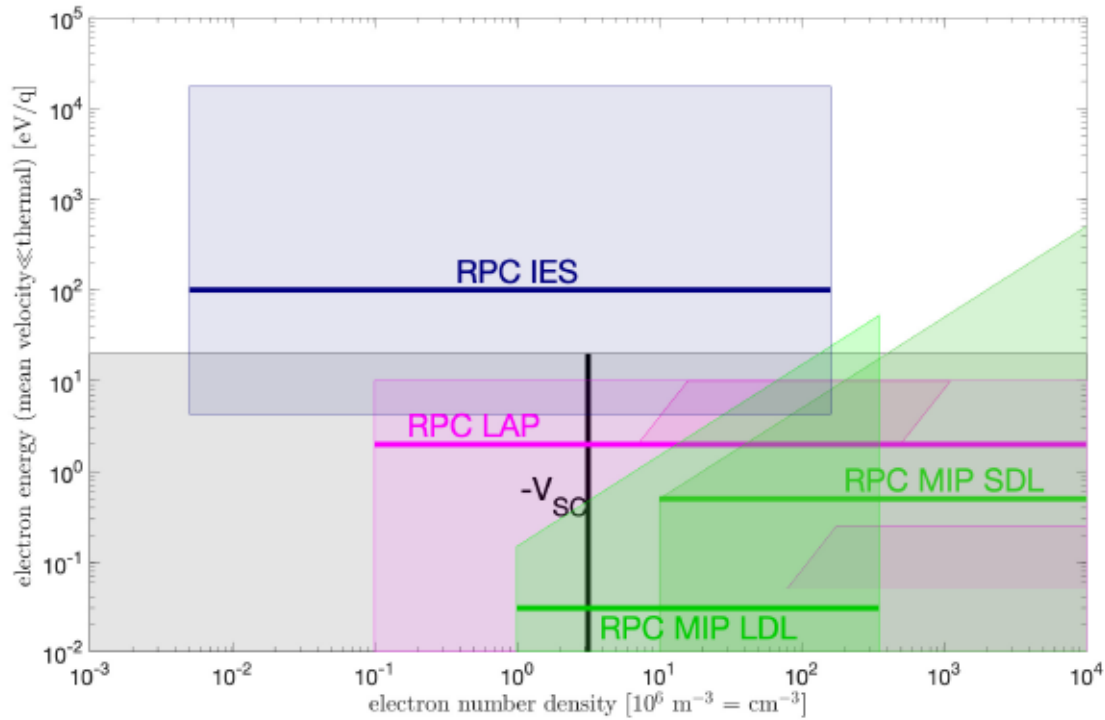


Figure 2.2: (Blue) IES: limits have been derived from instrumental performance. (Green) MIP: limits from the limits of detection of the instruments stated above in section 2.3. (Magenta) LAP: The small LAP parallelograms refer to the plasma density from the probe sweeps given in the ASW.TAB files. The upper one refers to the nominal case when no cold e^- are detected and we then use $T_e = 5$ eV. The lower refers to when cold e^- are detected, in which case we use $T_e = 5$ eV. The density ranges for these boxes are set by the range of the LAP current measurement. The large box corresponds the plasma number density based on V_{SC} in the NPL.TAB files. For any temperature within a box, the resulting density is good to within 50%. A typical value of the spacecraft potential has been over-plotted in grey (-20 V) but it is not representative of its variability or largest value throughout the mission.

2.3.1 List of dataset

Table 2.7: List of available dataset regarding the plasma (positive ion or electron) number density, along with H^- number density.

Name	Unit	Sensor	Level	Brief description
Solar wind number density				
ICA Solar wind ion densities	cm^{-3}	ICA	L5	0 th order moment. May be strongly affected by instrument field of view for H^+ , He^+ and He^{2+} . Delivered for active mission as part of enhanced archive effort (currently not ingested in PSA). PSA folder: RO-C-RPCICA-5-EXT2-MOMENT-V1.0 Data files: RPCICA{YYYYMMDD}T{hh}_000_L5_MOM.xxx

IES Solar Wind Ion densities	cm^{-3}	IES/ION	L5	Solar wind proton, alpha, and He^+ densities PSA folder: RO-{TT}-RPCIES-5-{pppp}-V{v}.0 Data files: RPCIES{YYYYDOY}_L5ION_MOM_V{v}.TAB
Cometary ion density				
ICA Cometary Ion density	cm^{-3}	ICA	L5	0 th order moment from ions fo energies <60 eV. Affected by the limited instrument field-of-view. Strongly affected by spacecraft potential for low energy population. Typically only a small fraction of the total low energy density is seen (see RPC example case). Delivered for active mission as part of enhanced archive effort (currently not ingested in PSA). PSA folder: RO-C-RPCICA-5-EXT2-MOMENT-V1.0 Data files: RPCICA{YYYYMMDD}T{hh}_000_L5_MOM.xxx
Negative ion density				
IES Negative Ion densities	cm^{-3}	IES/ELC	L5	Densities of H- resulting from charge exchange in the coma PSA folder: RO-{TT}-RPCIES-5-{pppp}-V{v}.0 Data files: RPCIES{YYYYDOY}_L5ELC_MOM_V{v}.TAB
Electron number density				
MIP density (RPCMIP)	cm^{-3}	MIP	L5	Electron number density, derived from RPC-MIP spectra analysis. PSA folder: RO-C-RPCMIP-5-{pppp}-V{v} Data files: RPCMIPS5D{mo}{YMMDDmm}{xxxxx}.TAB where {mo} describes the mode/sub-mode and {xxxxx}, the duration in minutes (see RPC-MIP User Guide for details)
LAP density (N_E_FIX_T_E)	cm^{-3}	LAP	L5	Electron number density derived from electron current in LAP sweeps assuming $T_e = 5$ eV. PSA folder: RO-C-RPCLAP-5-{pppp}-DERIV2-Vv.0 Dataset files: LAP_{YYYYMMDD}_{hhmmss}_{xxx}_ASW.TAB where {xxx} is the corresponding LAP operational mode.
IES Electron density	cm^{-3}	IES/ELC	L5	Mixed population electron density PSA folder: RO-{TT}-RPCIES-5-{pppp}-V{v}.0 Dataset files: RPCIES{YYYYDOY}_L5ELC_MOM_V{v}.TAB

Cross-calibrated plasma number density				
MIP-LAP plasma density (RPCMI- P/RPCLAP)	cm ⁻³	MIP, LAP	L5	High time resolution (up to 17 ms) electron number density, derived on selected periods from the cross-calibration of RPCMIP electron density and RPCLAP floating potential or ion current (see RPCMIP/RPCLAP cross-calibration report). PSA folder: RO-C-RPCMIP_RPCLAP-5-{pppp}-V{v} Data files: RPCMIPLAPS5{YYMMDDhh}{xxxxx}.TAB
LAP-MIP electron density (N_ED)	cm ⁻³	LAP, MIP	L5	Electron number density derived from spacecraft potential proxy V_{SC} at low time resolution (32-160 s) calibrated to RPCMIP data when available, otherwise RPCLAP. PSA folder: RO-C-RPCLAP-5-{pppp}-DERIV2-V{v}.0 Data files: LAP_{YYYYMMDD}_{hhmmss}_{xxx}_NED.TAB
LAP-MIP electron density (N_EL)	cm ⁻³	LAP, MIP	L5	Electron number density (16 ms to a few seconds). In 2014 and during the nightside excursion, a joint dataset of MIP and LAP densities is used for cross-calibration purposes – combining the MIP dataset with scaled LAP densities allowing T_E estimate to vary or alternatively, compensating for the density depletion in the sheath of the spacecraft –, otherwise it is “purely” calibrated with MIP densities. The width of the calibration window is 3-5 days for N_EL (to be compared to 20 s for the MIP-LAP electron density). PSA folder: RO-C-RPCLAP-5-{pppp}-NPL-V{v}.0 Data files: LAP_{YYYYMMDD}_{hhmmss}_{xxx}_NEL.TAB

2.3.2 Cross-calibrated products

As part of cross-calibration activities mainly MIP-LAP, measurements of the same physical quantity (e.g., plasma number density) from different instruments have been combined together to generate additional science product. Moreover, it provided the opportunity to assess the reliability of the different dataset, depending on the plasma conditions.

A first example is given by Fig. 2.3 showing the comparison between RPCMIP and RPCLAP for the plasma number density. A second example is shown in Fig. 2.6 and compared with other dataset.

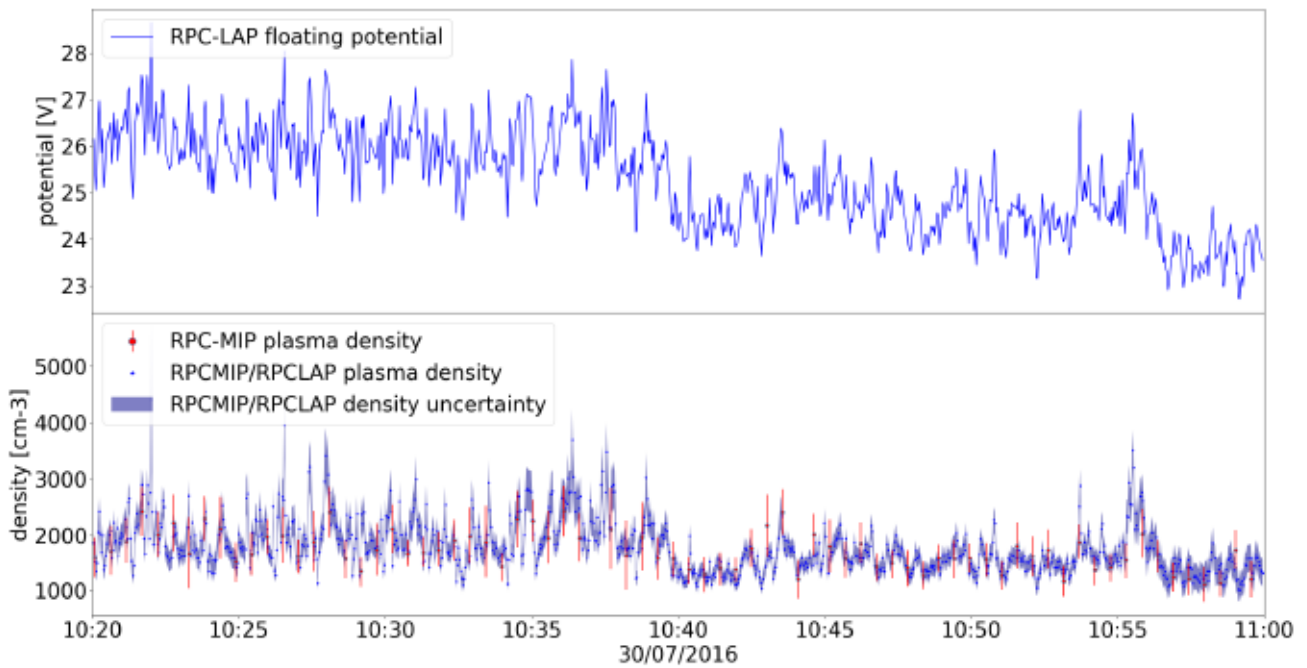


Figure 2.3: Example of RPCMIP/RPCLAP cross-calibrated densities over 20 minutes for 30 July 2016, from top to bottom: (i) RPC-LAP MIP floating potential used as input to the cross-calibration procedure, (ii) RPC-MIP plasma density (Level 3) used as input to the cross-calibration procedure and resulting RPCMIP/RPCLAP cross-calibrated plasma densities with associated uncertainties (Level 5).

Another cross-calibration product is RPCLAP-RPCMIP and a comparison of this product with the other dataset is provided in Section. 2.3.4 and details are given in Table 2.7.

2.3.3 Which solar wind number density should be used?

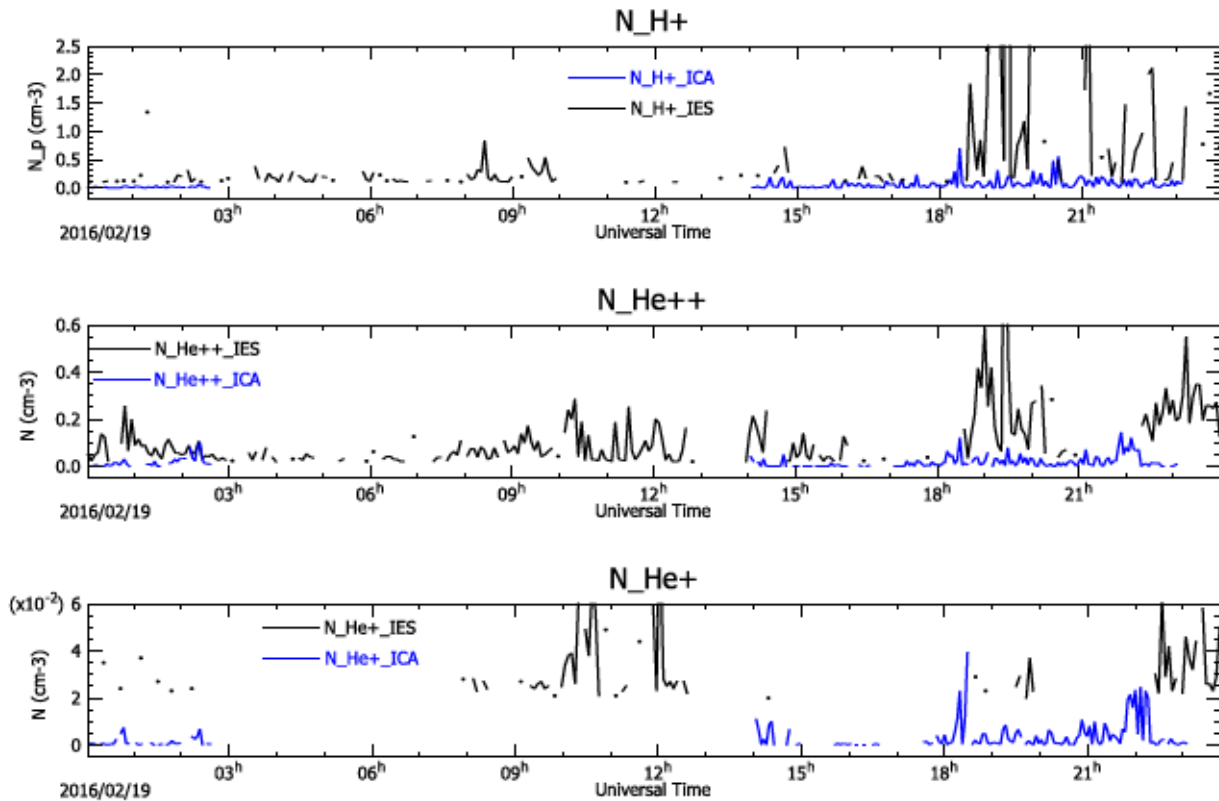


Figure 2.4: Proton (upper panel), alpha (middle panel) and He^+ (lower panel) number density from RPC-ICA and RPC-IES the 19th of February 2016

The user may consider combining RPC-ICA and RPC-IES for the solar wind. Comparison has been done between IES and ICA for the solar wind (see Fig. 2.5 and 2.7). IES and ICA both provide ion data, with to some extent complementary fields of view. In Fig. 2.5, we show the solar wind proton density from both instruments and in Fig. 2.7, the speed of the solar wind protons. The densities from the two instruments show similar statistical characteristics but are not always the same for a given time. This is an effect of the different field of view of the two instruments. The moment data sets can be joined in a simple way by choosing the moments from the instrument indicating the highest density. One should however note that IES does not have mass-discrimination and may mistake pick-up cometary ions for solar wind ions. These frequently overlap in energy range, but usually not in flow direction. The relation between the ICA density and the solar wind density from the OMNI database is discussed in the RPC-ICA User Guide. In short, the upper envelope agrees very well, but there is a considerable scatter towards lower density for ICA. This is a combination of the limited field of view, enhancement and rarefaction of the solar wind caused by the observed deflection, as well as charge-exchange loss of protons.

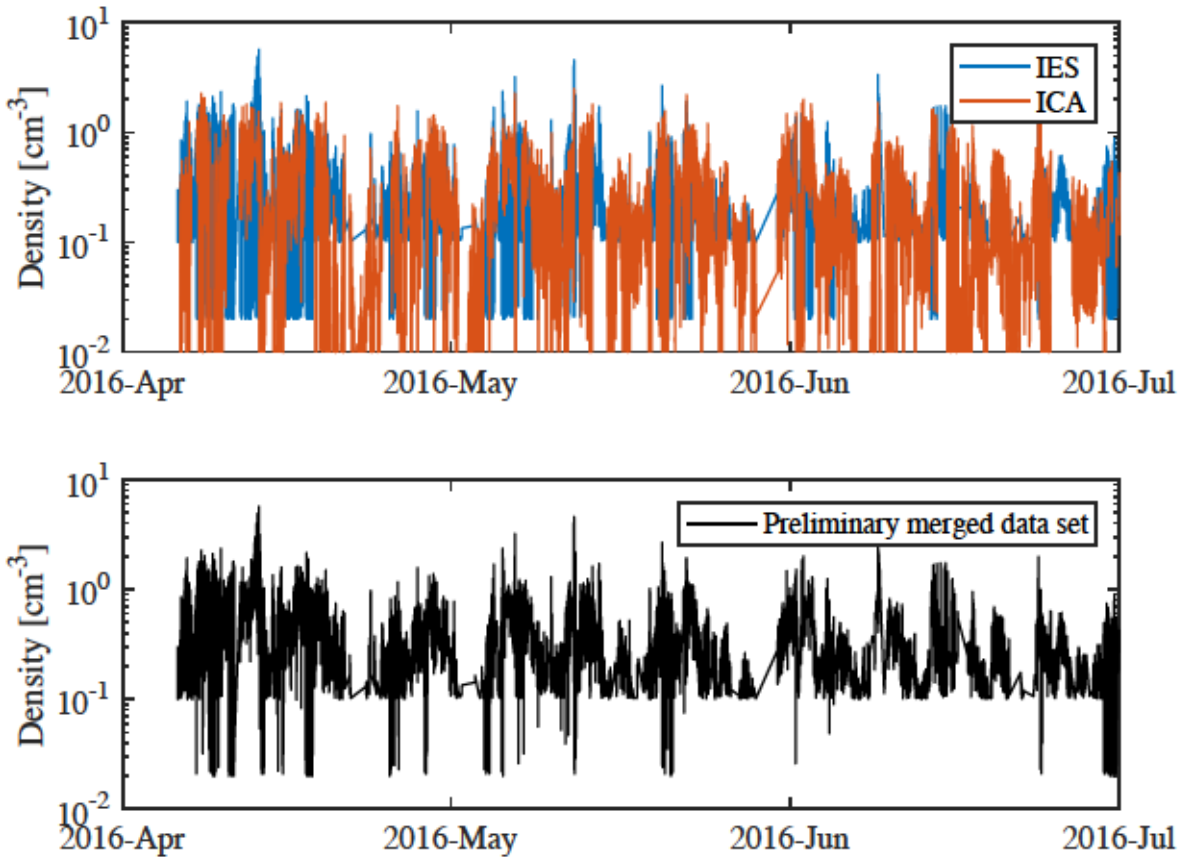


Figure 2.5: Upper panel: Solar wind proton density from both instruments. Lower panel: a preliminary merged data set where ICA data has been interpolated to the times of IES measurements and the data with the highest density has been used in the merged dataset. The combined dataset is preliminary and is not part of the current delivery.

2.3.4 Which cometary plasma number density should be used?

Plasma density for a given time interval of the order of hours or shorter: First check if your interval of interest is available in the cross-calibrated MIP-LAP dataset in the MIP archive. If so, this will provide high-time resolution (16 ms to a few seconds) data of high quality. If there are no such data, use if available the LAP-MIP density data products N_{ED} (time resolution 32 s to few minutes) or N_{EL} (16 ms to a few seconds). Note that N_{EL} is N_{ED} with a high time resolution cross-calibration of LAP ion current to densities (mostly, MIP). In parallel, check also for MIP-only densities, keeping in mind that MIP has upper/lower boundaries in retrievable densities that depend on operational mode, which might result in some bias if used blindly.

Plasma density for intervals of days or more: The most consistent dataset for long term studies is the low time resolution LAP-MIP cross calibrated data product known as N_{ED} , available in the NED.TAB files in the LAP data. This is the dataset with a high dynamic range and the broadest coverage over all the mission. The homogeneity of this dataset is particularly important for statistical studies. The N_{ED} time resolution varies between 32 s and a few minutes and the accuracy of any individual data point is less than in the MIP densities, but the wider dynamic range means less of systematic bias towards high or low densities.

High dynamic range density data: The dataset with the largest dynamic range is LAP-MIP N_EL which is based on the N_ED with a better time resolution (which improves the range) and a cross-calibration using ion currents (which improves the performance for the very lower densities).

High time resolution density data: If you need better time resolution than about a second, LAP needs to be in burst mode (BM). Data are available either as MIP-LAP cross-calibrated data in the MIP dataset, or as the cross-calibrated LAP-MIP data product N_EL in the NEL.TAB files of the LAP archive. If you need better time resolution than about a second, LAP needs to be in burst mode (BM). Data are available either as MIP-LAP cross-calibrated data in the MIP dataset, or as the cross-calibrated LAP-MIP data product N_EL in the NEL.TAB files of the LAP archive. The former is detailed in the RPCMIP/RPCLAP Cross-Calibration Report. The latter uses a calibration to available MIP data over a period of days, and to the LAP N_E_FIX_T_E data product if MIP data are not sufficient.

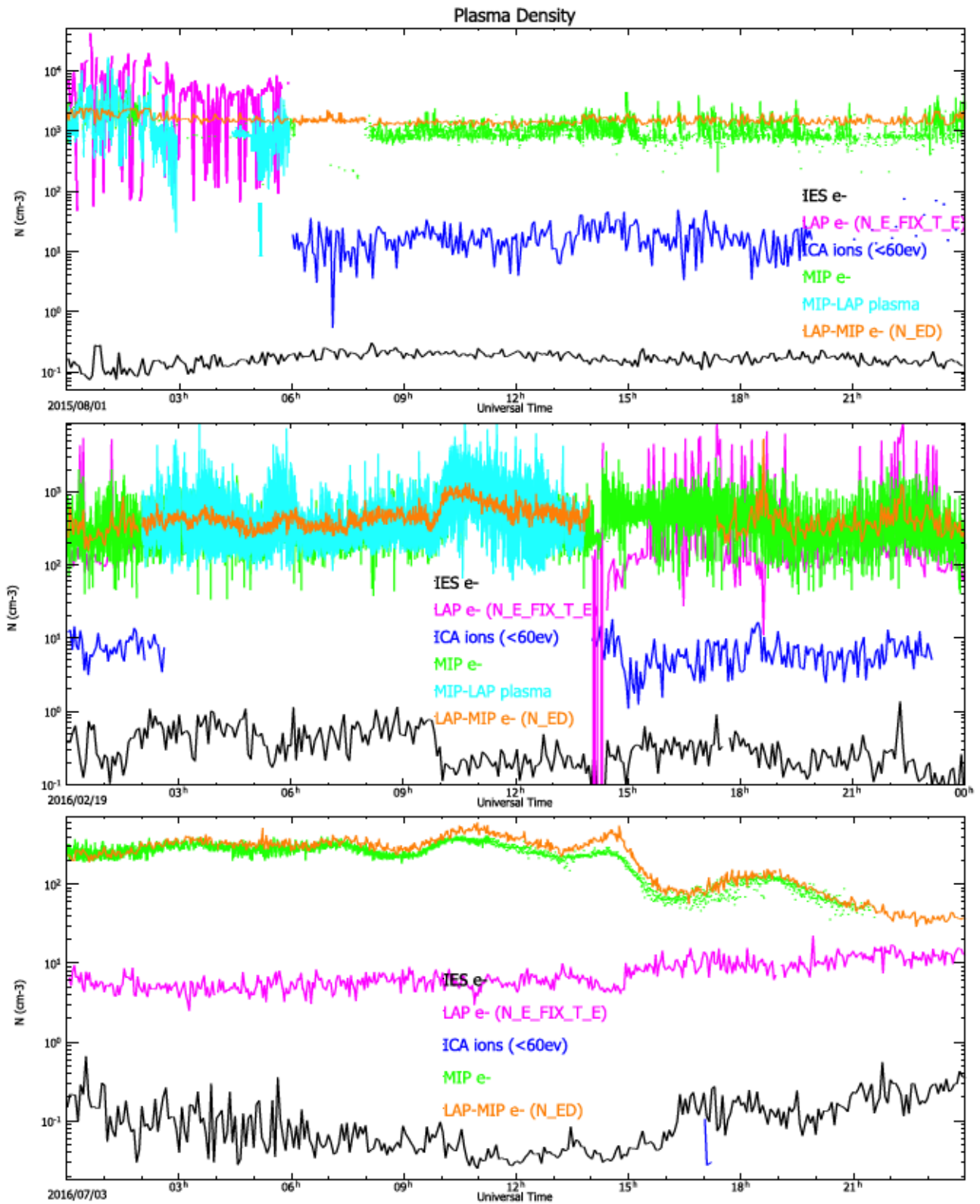


Figure 2.6: Plasma (electron or ion) number densities from RPC-MIP, RPC-LAP, RPC-ICA, RPC-IES and cross-calibrations between MIP and LAP the 1st of August 2015 (upper panel), the 19th of February 2016 (middle panel), and the 3rd of July 2016 (bottom panel). The ion number density from RPC-ICA has been derived from cometary ions at energies between a few eVs (not 0) and 60 eV.

Table 2.8: Hierarchy between the dataset available for the cometary plasma number density

What is the user interested in?	Which product should the user use?
High time (down to 16 ms) total plasma density	MIP-LAP plasma density If not available, LAP-MIP electron density (N_EL) If neither, MIP electron density
Statistical study (large time coverage) of total plasma density	LAP-MIP electron density (N_ED)
High dynamic range total plasma density	LAP-MIP electron density (N_EL) and if not available, N_ED
Study of a specific day, medium time resolution of the total plasma density	MIP-LAP plasma density If not available, LAP-MIP (N_EL or N_ED, down to 32-second time resolution) If neither, MIP
Positive ion density of the solar wind	ICA or IES solar wind number density (to check both)

2.4 Plasma (ion and electron) velocity and speed (RPC-ICA, RPC-LAP/MIP and RPC-IES)

- **RPC-ICA:** The numerically integrated first order moment is delivered as a velocity. This works generally very well for solar wind ions, when the ion beam is within the field of view of the instrument. Lower energy (cometary) ions can be significantly affected by the spacecraft potential as well, which may make the direction unreliable.
 - **Major strength:** Direct estimate of the numerically integrated velocity of observed ions. Good dynamic range from several $\text{km}\cdot\text{s}^{-1}$ to several $100 \text{ km}\cdot\text{s}^{-1}$.
 - **Major limitation:** Angular coverage, in particular at low energy. Low energy ions affected by spacecraft potential.
- **RPC-LAP:** `V_ION_EFF_XCAL` in the `LAP_{YYYYMMDD}_{hhmmss}_XXX_ASW.TAB` files is an estimate of the cometary ion effective speed from the ion slope and the RPCMIP density estimates. It is derived from the slope of the LAP sweeps in the ion saturation region. The slope is proportional to density and inversely proportional to ion momentum, so by assuming all ions are H_3O^+ (mass 19 u) and with use of a simultaneous MIP density, it is possible to derive an effective flow speed. For a plasma with a distribution of ion energies, as should most often be the case, `V_ION_EFF_XCAL` is not the arithmetic mean but a harmonic mean (the inverse of the mean of inverses) and so is weighted toward the lowest energies.
 - **Major strength:** Availability over large part of the mission.
 - **Major limitation:** At large velocities or low densities the error in the fit procedure becomes very large, ions are water ions
- **RPC-IES:**
 - **Major strength:** Availability over large part of the mission.

- **Major limitation:** for electrons, population is a mixture of solar wind, cometary, secondaries, affected by S/C potential. For ions, includes only solar wind. For both, sometimes affected by limited FOV.

2.4.1 List of dataset

Table 2.10: List of available dataset regarding the plasma (ion or electron) velocity and speed

Name	Unit	Sensor	Level	Brief description
Solar wind velocity				
ICA Solar wind velocity	km·s ⁻¹	ICA	L5	1 st order moment, integrated over the field-of-view and energy range of the instrument for H ⁺ , He ⁺ and He ²⁺ . PSA folder: RO-C-RPCICA-5-EXT2-MOMENT-V1.0 Data files: RPCICA{YYYYMMDD}T{hh}_000_L5_MOM.xxx
IES Solar wind velocity	km·s ⁻¹	IES/ION	L5	Solar wind H ⁺ , He ⁺ and He ²⁺ velocities in CSEQ coordinates PSA folder: RO-{TT}-RPCIES-5-{pppp}-V{v}.0 Data files: RPCIES{YYYYDOY}_L5ION_MOM_V{v}.TAB
Cometary ion velocity				
ICA Cometary ion velocity	km·s ⁻¹	ICA	L5	1 st order moment, integrated over the field-of-view and energy range of the instrument. PSA folder: RO-C-RPCICA-5-EXT2-MOMENT-V1.0 Data files: RPCICA{YYYYMMDD}T{hh}_000_L5_MOM.xxx
LAP-MIP effective ion speed (V_ION_EFF_XCAL)	km·s ⁻¹	LAP, MIP	L5	Effective ion speed derived from RPCLAP sweeps and simultaneous RPCMIP density assuming $m_i/q = 19 \text{ u} \cdot \text{q}^{-1}$ weighted towards low energies. PSA folder: RO-C-RPCLAP-5-{pppp}-DERIV2-Vv.0 Data files: LAP_{YYYYMMDD}_{hhmmss}_{xxx}_ASW.TAB
Negative ion velocity				
IES Negative ion velocity	km·s ⁻¹	IES/ELC	L5	H ⁻ (from charge exchange in the coma) velocity in CSEQ coordinates PSA folder: RO-{TT}-RPCIES-5-{pppp}-V{v}.0 Data files: RPCIES{YYYYDOY}_L5ELC_MOM_V{v}.TAB
Electron velocity				
IES Electron velocity	km·s ⁻¹	IES/ELC	L5	1 st order moment. Mixed population electron velocity. PSA folder: RO-{TT}-RPCIES-5-{pppp}-V{v}.0 Data files: RPCIES{YYYYDOY}_L5ELC_MOM_V{v}.TAB

2.4.2 Which solar wind velocity should be used?

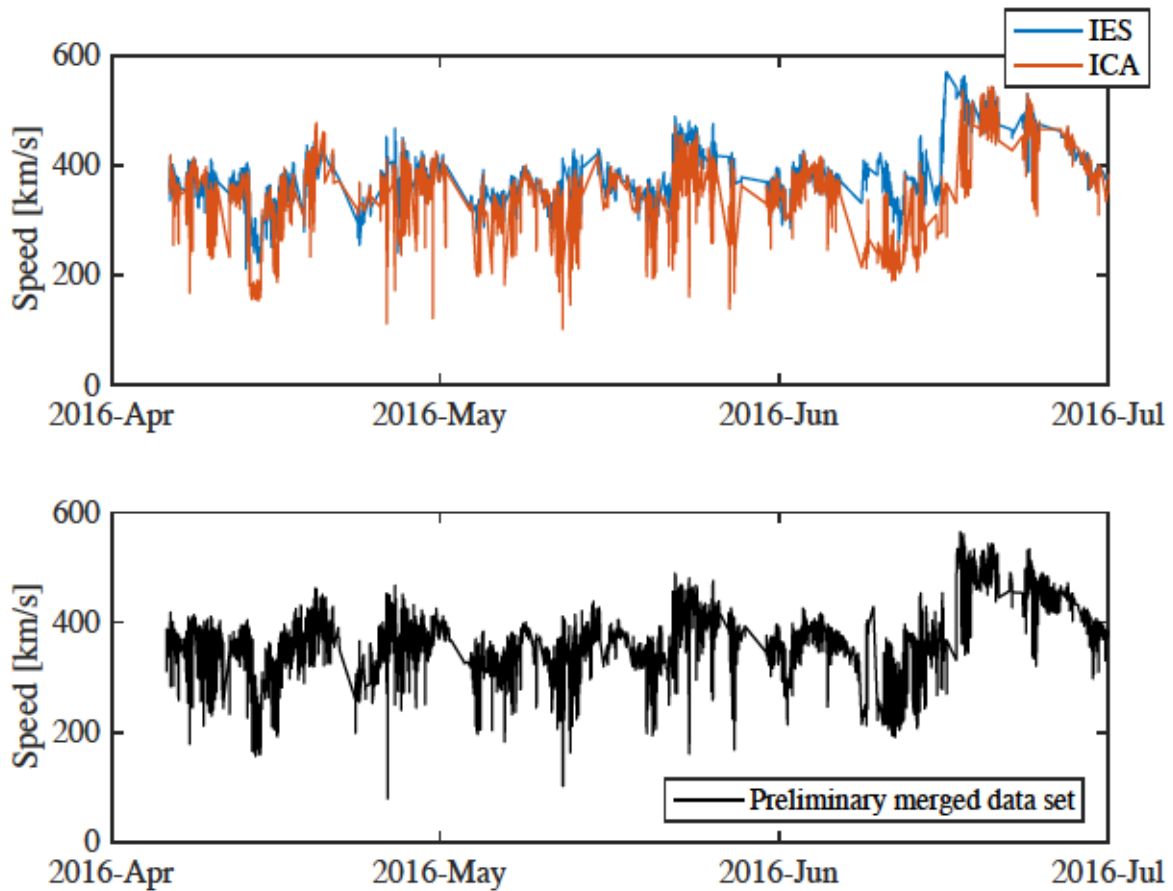


Figure 2.7: Same as Fig. 2.5 for the Solar wind proton speed.

Further comparison has been done between ICA and IES. As shown by Fig. 2.7, the speed determined from IES and ICA agree quite well, but the direction does not. The ICA derived velocity agrees well with the deflection reported in Behar et al. (2017) and Nilsson et al. (2017) which were derived from the same data but with different data processing. The reason for the discrepancy between the solar wind ion flow direction as determined by IES and ICA is not yet identified.

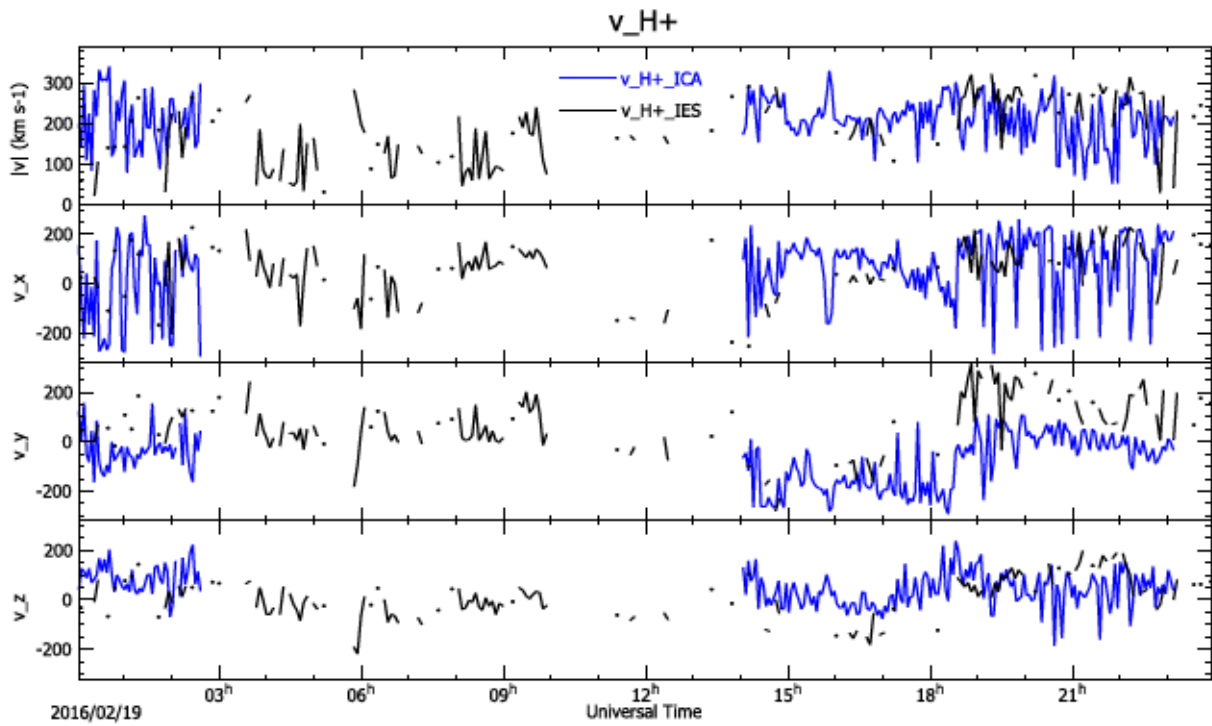


Figure 2.8: Proton velocity from RPC-ICA and RPC-IES the 19th of February 2016

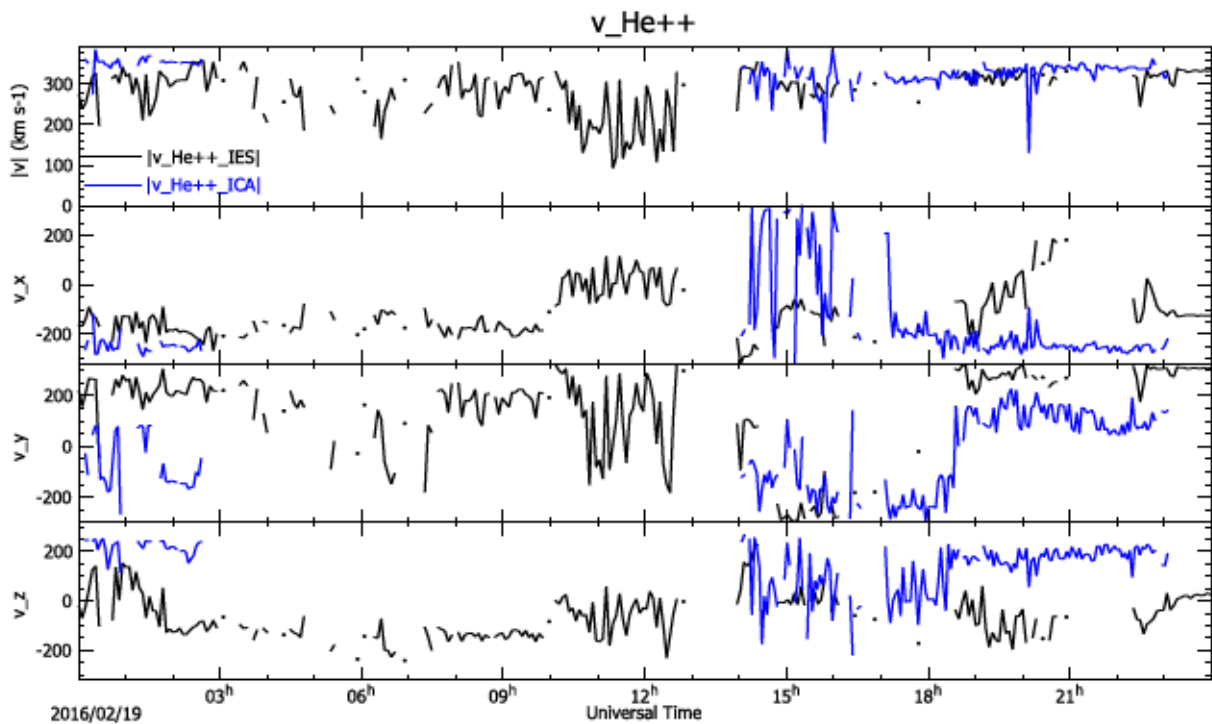


Figure 2.9: Alpha velocity from RPC-ICA and RPC-IES the 19th of February 2016

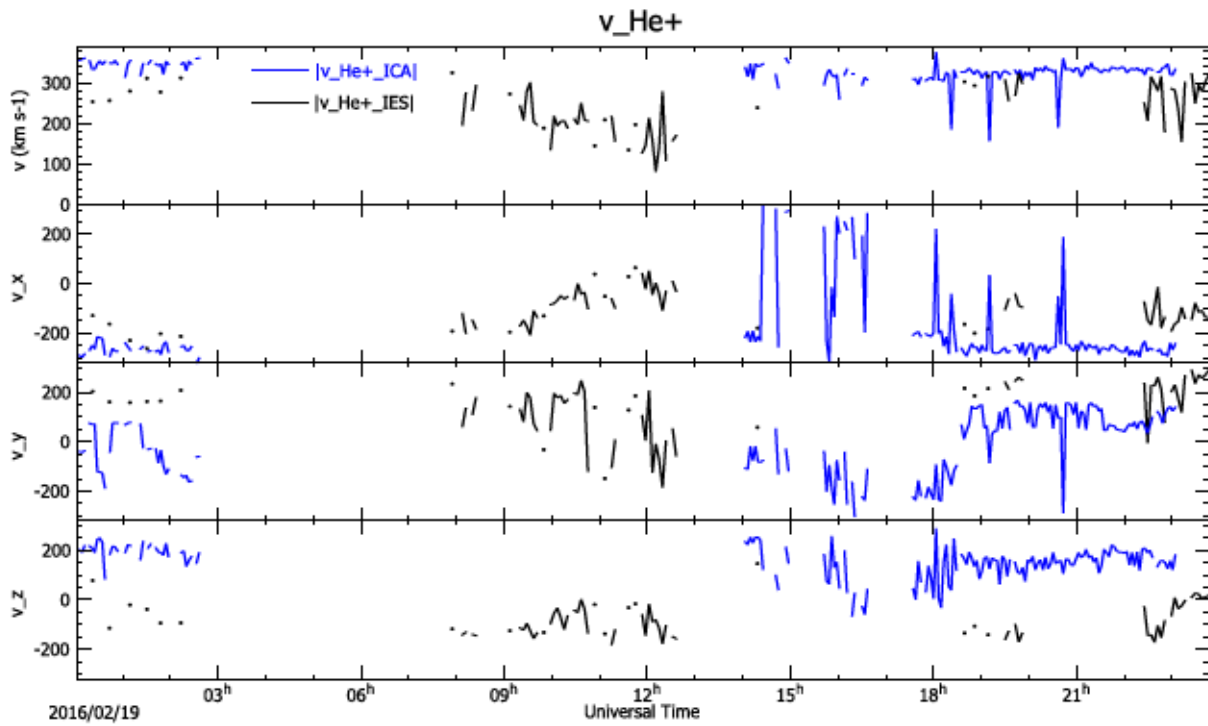


Figure 2.10: He^+ velocity from RPC-ICA and RPC-IES the 19th of February 2016.

The alpha particle moments from ICA in the currently delivered L5 data show a speed about 10% higher than the proton speed. Whereas protons can be expected to be somewhat more decelerated than alpha, as the force per mass from electric and magnetic fields is twice that for alpha particles, there remains concern that this is an instrumental effect. It is currently being investigated.

The He^+ signal is rather weak, but ICA can frequently detect a signal with a velocity similar to that for alpha particles. In the example shown in Fig. 2.10, the He^+ appears to be on the detection limit for IES, while the ICA velocity shows a consistent and expected pattern.

2.4.3 Which cometary ion speed should be used?

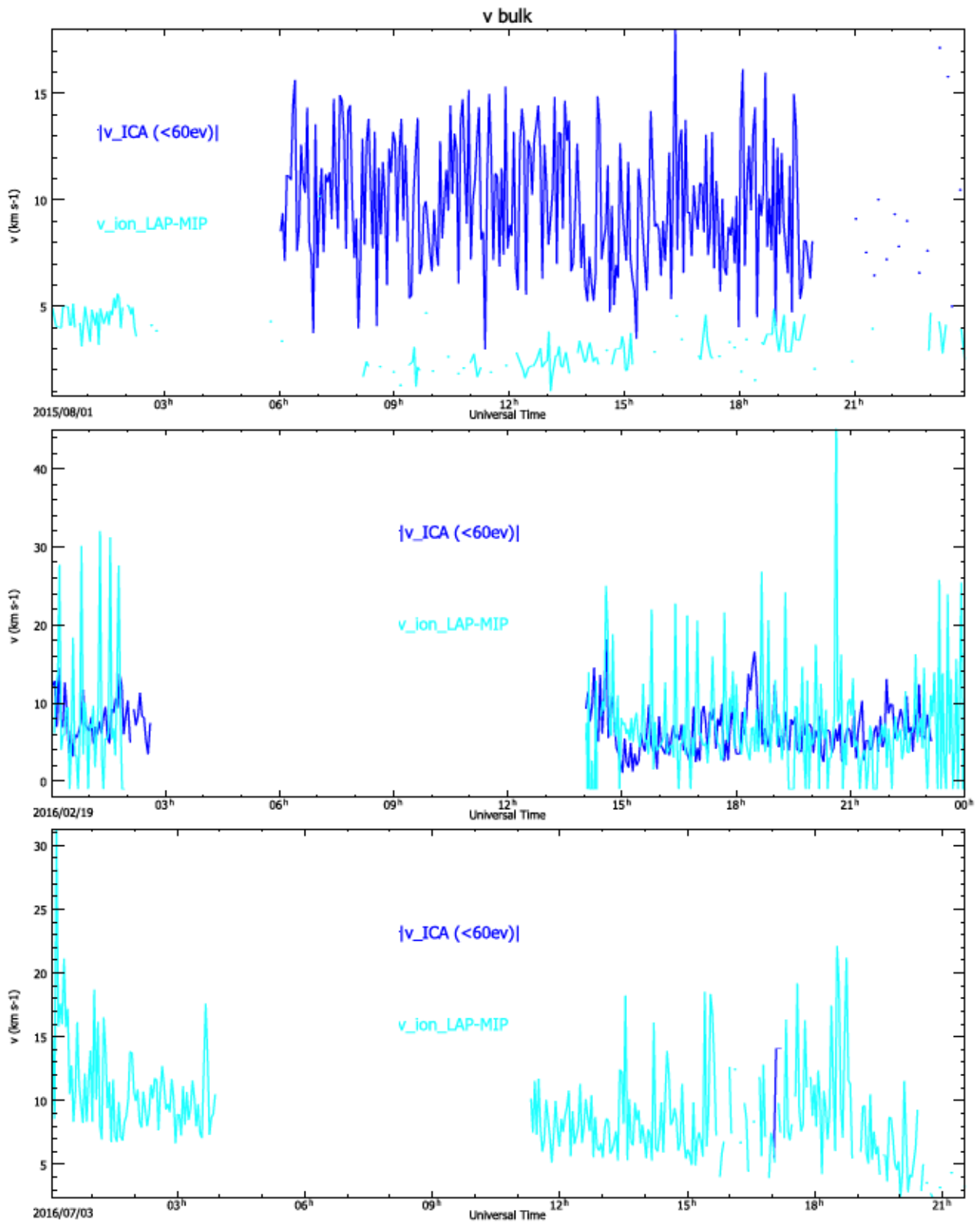


Figure 2.11: Cometary ion speed from RPC-ICA and RPC-LAP/MIP the 1st of August 2015 (upper panel), the 19th of February 2016 (middle panel), and the 3rd of July 2016 (lower panel). The bulk speed from RPC-ICA ($|v_{ICA} (<60\text{ev})|$) has been derived from ions at energies between a few eVs (not 0) and 60 eV.

The cometary ion density reported by ICA is frequently much lower than what is reported by the the RPC-LAP/MIP ion velocities extracted from simultaneous MIP and LAP data. (see Fig. 2.6). It is most likely that the lowest energy part of the (cometary) ion population is missing in the ICA data. Therefore it is quite possible that the ICA speed is an overestimation of the actual cometary ion velocity. We show one case (1st August 2015, Fig. 2.11-top) where the ICA speed is much higher than that of LAP. In the second case (19th February 2016, Fig.2.11-bottom), the speeds determined from both instruments are similar(taking into account that the measurements are provided at different time rates).

2.5 Plasma (ion and electron) temperature (RPC-IES and RPC-LAP/MIP)

- **RPC-LAP:** The ASW.TAB files include up to two electron characteristic energies. One of these energy is derived from LAP sweeps and the other, from both LAP sweeps and MIP data. The warm electron temperature (T_{ew}) results from the observed probe current in the part of a LAP bias voltage sweep where electrons are repelled by the probe as is usual for Langmuir probes. It should be noted that in case there is also a population electrons with T_e below about 0.5 eV, (T_{ew}) will still refer only to the warm component.
 - **Major strength:** availability over large part of the mission.
 - **Major limitation:** only refers to part of the electron distribution; errors in fit procedure sometimes significant.

The cold electron temperature (T_{ec}) is provided when the conductance of the probe sweep (dI/dV) exceeds $70 \text{ nA}\cdot\text{V}^{-1}$ and there is a simultaneous MIP density value available. In that case, the conductance is dominated by the contribution from cold electrons and T_{ec} can be derived from dividing the conductance by the MIP density as shown by (Engelhardt et al., 2018a).

- **Major strength:** good measure of cold electron presence and robust upper limit on their temperature.
- **Major limitation:** there may be a cold electron population even if not reported here (due to highly negative spacecraft potential hiding it from LAP, or no MIP data available).
- **RPC-IES:**
 - **Major strength:** availability over large part of the mission.
 - **Major limitation:** for electrons, population is a mixture of solar wind, cometary, secondaries, affected by S/C potential. For ions, includes only solar wind. For both, sometimes affected by limited FOV.

2.5.1 List of dataset

Table 2.12: List of available dataset regarding the plasma temperature

Name	Unit	Sensor	Level	Brief description
Ion temperature				
IES Solar wind temperature	K	IES/ION	L5	Solar wind H ⁺ , He ⁺ and He ²⁺ temperatures PSA folder: RO-{TT}-RPCIES-5-{pppp}-V{v}.0 Data files: RPCIES{YYYYDOY}_L5ION_MOM_V{v}.TAB
IES Negative ion temperature	K	IES/ELC	L5	H ⁻ (from charge exchange in the coma) temperature PSA folder: RO-{TT}-RPCIES-5-{pppp}-V{v}.0 Data files: RPCIES{YYYYDOY}_L5ELC_MOM_V{v}.TAB
Electron temperature				
T_{ew} (T_E)	eV	LAP	L5	Characteristic energy of warm electrons (0.5 – 15 eV) from LAP bias voltage sweeps PSA folder: RO-C-RPCLAP-5-{pppp}-DERIV2-V{v}.0 Data files: LAP_{YYYYMMDD}_{hhmmss}_{xxx}_ASW.TAB
T_{ec} (T_E_XCAL)	eV	LAP, MIP	L5	Characteristic energy of cold electrons (~ 0.1 eV) from LAP sweeps and MIP densities PSA folder: RO-C-RPCLAP-5-{pppp}-DERIV2-V{v}.0 Data files: LAP_{YYYYMMDD}_{hhmmss}_{xxx}_ASW.TAB
IES Electron temperature	K	IES/ELC	L5	Temperature of electrons – mixed population PSA folder: RO-{TT}-RPCIES-5-{pppp}-V{v}.0 Dataset files: RPCIES{YYYYDOY}_L5ELC_MOM_V{v}.TAB

2.5.2 Which electron temperature should be used?

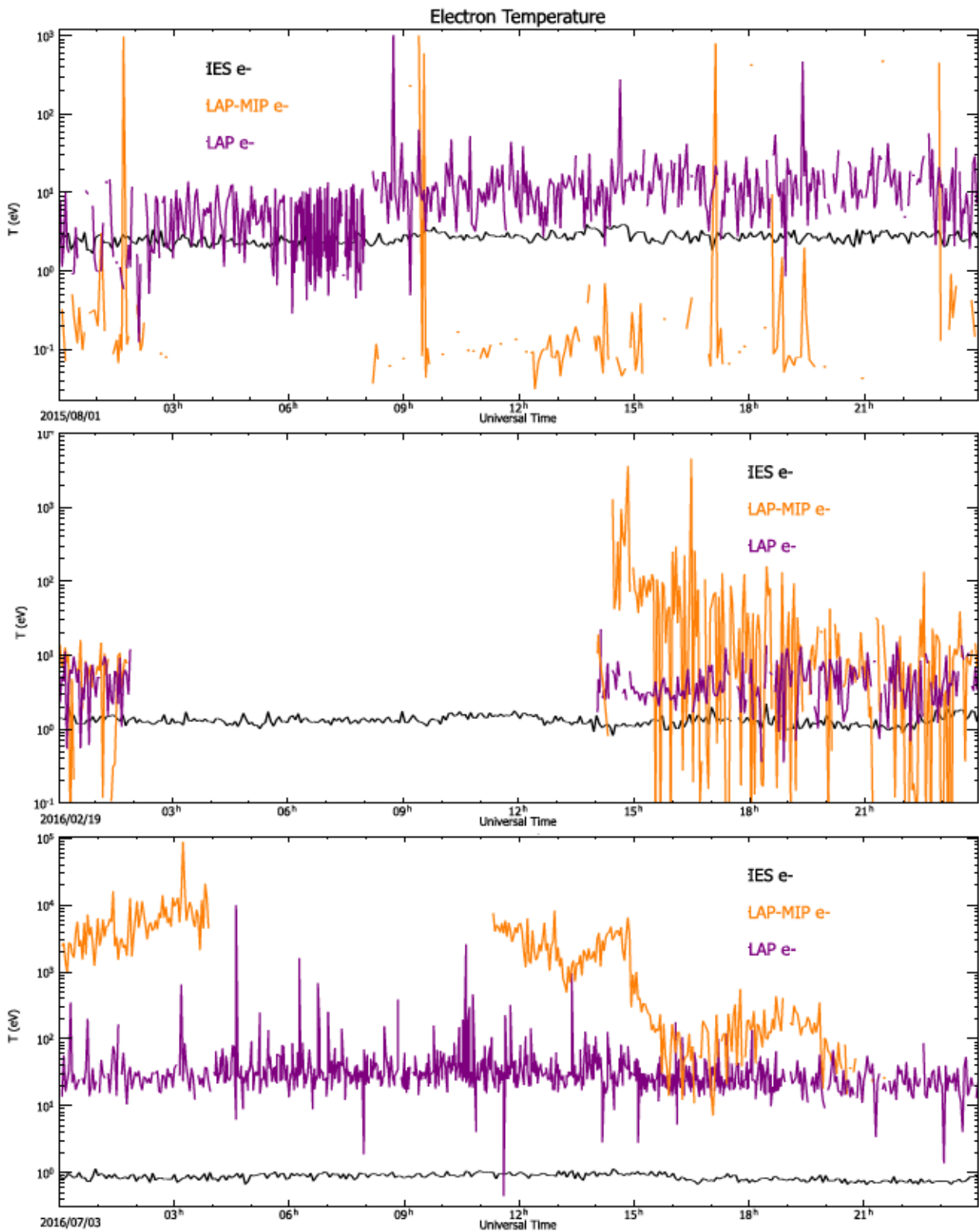


Figure 2.12: Electron temperature from RPC-IES, RPC-LAP and cross-calibration LAP-MIP the 1st of August 2015 (upper panel), the 19th of February 2016 (middle panel), and the 3rd of July 2016 (lower panel).

The most reliable dataset for the electron temperature is the cross-calibrated LAP/MIP product.

2.6 Electric field (RPC-LAP and RPC-MIP)

- **RPC-LAP:**

Electric field The LAP electric field estimate in the EFL.TAB files is derived from the voltage between the two LAP probes divided by their distance, and defined to be positive when directed from LAP2 to LAP1. The value is only reported when both probes are operated in floating mode and both are sunlit. As the DC level of the electric field is prone to contamination by spacecraft-plasma interaction features, a 32 second moving average value has been removed. There is no good cross-calibration available for this quantity, but the technique is widely used on ionospheric spacecraft. Low-frequency ($\sim 0.1 - 20$ Hz) electric fields are available for (quite rare) periods when both LAP probes are in floating mode and both are illuminated by the Sun. Available as the EFL parameter in the EFL.TAB files.

- **Major strength:** availability of E-field information
- **Major limitation:** possible influence of spacecraft-related electrostatic fields

High frequency waves Short snapshots at usually $18750 \text{ samples}\cdot\text{s}^{-1}$ are available from most macros (in the last months of the mission often downsampled onboard to a few kHz). However, data transmission bandwidth limited their length on the order of 100 points for normal mode (NM, see above) macros, so BM macros (record length ~ 1000 samples) are more useful. The sensitivity is higher for E-field (voltage) measurement than for the probe current. Spectra are available in the PSD.TAB files.

- **RPC-MIP:** The MIP electric field along the direction of the MIP boom, in the frequency range [7-448] kHz or [7-3584] kHz depending on operational mode, can be straightforwardly derived from the electric potential spectra obtained from the so-called MIP passive mode, that is obtained from fast Fourier transforming the difference of electric potential measured between the two MIP receivers, separated by 1 metre.

An electric field can be derived also from the data sampled at high (kHz) frequency. This can be done trivially by taking differences of the V1H.TAB and V2H.TAB files available in L3 data.

2.6.1 List of dataset

Table 2.14: List of available dataset regarding the electric field measurements

Electric field				
Name	Unit	Sensor	Level	Brief description
Electric field (EFL)	$\text{mV}\cdot\text{m}^{-1}$	LAP	L5	Electric field component along LAP probe separation vector, in EFL.TAB files.
Probe voltage	V	LAP	L3	Probe voltage with respect to the spacecraft for both LAP probes at high time resolution (files V1L.TAB and V2L.TAB for frequencies of ~ 1 Hz, V1H.TAB and V2H.TAB for kHz range).
MIP passive spectra	dB	MIP	L3	Electric field spectra Time resolution depends on operational parameters (see Section 2 and RPC-MIP User Guide) PSA folder: RO-C-RPCMIP-3-{pppp}-V{v} Data files: one file type per sub-mode RPCMIPS3E{mo}{YYMMDDhhmm}_{xxxxx}.TAB where {mo} describes the mode/sub-mode and {xxxxx}, the duration in minutes (see RPC-MIP User Guide for details)
MIP active spectra	dB	MIP	L3	Electric mutual impedance spectra Time resolution depends on operational parameters (see Section 2 and RPC-MIP User Guide) PSA folder: RO-C-RPCMIP-3-{pppp}-V{v} Data files: one file type per sub-mode RPCMIPS3W{mo}{YYMMDDhhmm}_{xxxxx}.TAB

2.7 Spacecraft potential V_{SC} (RPC-LAP)

The principal LAP spacecraft potential (V_{SC}) proxy is available in the USC.TAB files, whose identifier USC is chosen to indicate its nature of a proxy for V_{SC} . The value reported in these files is the potential of the spacecraft with respect to the probe when no current is flowing between them, often referred to as the “floating potential”. This is derived either from the voltage at which the probe current is zero in LAP probe bias sweeps, or, when at least one LAP probe is in E-field mode, from the time series of the probe floating potential. In this case, the time resolution is 32 s (averaged from data with up to 57.8 Hz sampling) while for sweeps it is slightly lower, most often 160 s.

As the booms on which the LAP probes are mounted have finite length, the probes cannot pick up the full spacecraft potential, and in addition there is a voltage drop (of order 1 V) over the plasma sheath surrounding the probe. The relation of the observed USC to the real V_{SC} has been investigated by Odelstad et al. (2017, 2018): typically, $U_{SC} \sim 0.8 V_{SC}$.

- **Major strength:** robust measurement available over most of the mission.

- **Major limitation:** some uncertainty on absolute calibration to V_{SC}

There is also another spacecraft potential proxy available, in the ASW files. This is known as V_{ph} and is the observed “photoelectron knee”, the upper limit of probe voltages where all photoelectrons are repelled from the probe. If reliably identified in the sweep, this should be a better estimate of V_{SC} than USC is, as there at this point on the probe current-voltage characteristic should be no voltage drop over the sheath around the probe. On the other hand, it is often problematic to reliably identify in LAP sweep data particularly at high plasma densities, and is therefore considered less robust than USC. Nevertheless, it may still be of interest to users interested in the spacecraft potential and is therefore provided in the ASW files.

2.7.1 List of dataset

Table 2.16: List of available dataset regarding the spacecraft potential V_{SC}

Spacecraft potential V_{SC}				
Name	Unit	Sensor	Level	Brief description
U_SC	V	LAP	L5	Spacecraft potential proxy from floating probe, in USC.TAB files.
V_{ph}	V	LAP	L5	Spacecraft potential proxy from probe photoemission threshold voltage (“knee”), in ASW.TAB files.

In principle, it is always available as the USC parameter in the USC.TAB files, either from the LAP sweeps or from single-probe measurements in the E-field mode (voltage measurement). H

2.8 Magnetic field (RPC-MAG)

2.8.1 List of dataset

Table 2.18: List of available dataset regarding the magnetic field measurements.

Magnetic field components					
Name	Unit	Sensor	Level	Coordinates	Brief description
Magnetic field	Raw ADC counts	RPC-MAG-OB RPC-MAG-IB	L2	Instrument	Magnetic field data with original sampling (OB: 1 or 20 Hz, IB: 0.03125 or 1 Hz) PSA folder: RO-{target}-RPCMAG-2-{pppp}-RAW-V{v} Data files: RPCMAG{YMMDD}_RAW_{SS}_M{mode}. where {SS} correspond to the sensor (IB: inboard or OB: onboard)
Magnetic field	nT	RPC-MAG-OB RPC-MAG-IB	L3	Instrument (LEVEL_A)	Magnetic field data with original sampling (OB: 1 or 20 Hz, IB: 0.03125 or 1 Hz) PSA folder: RO-{target}-RPCMAG-3-{pppp}-CALIBRATED-V{v} Data files: RPCMAG{YMMDD}_CLA_{SS}_M{mode}.*
Magnetic field	nT	RPC-MAG-OB RPC-MAG-IB	L3	spacecraft (LEVEL_B)	Magnetic field data with original sampling (OB: 1 or 20 Hz, IB: 0.03125 or 1 Hz) PSA folder: RO-{target}-RPCMAG-3-{pppp}-CALIBRATED-V{v} Data files: RPCMAG{YMMDD}_CLB_{SS}_M{mode}.*
Magnetic field	nT	RPC-MAG-OB RPC-MAG-IB	L3	spacecraft (LEVEL_B)	Magnetic field data with original sampling (OB: 1 or 20 Hz, IB: 0.03125 or 1 Hz) PSA folder: RO-{target}-RPCMAG-3-{pppp}-CALIBRATED-V{v} Data files: RPCMAG{YMMDD}_CLC_{SS}_M{mode}.*
Magnetic field	nT	RPC-MAG-OB RPC-MAG-IB	L3	CELESTIAL (LEVEL_C)	Magnetic field data with original sampling (OB: 1 or 20 Hz, IB: 0.03125 or 1 Hz) Data contain spacecraft positions as well PSA folder: RO-{target}-RPCMAG-3-{pppp}-CALIBRATED-V{v} Data files: RPCMAG{YMMDD}_CLC_{SS}_M{mode}.*
Magnetic field	nT	RPC-MAG-OB RPC-MAG-IB	L4	spacecraft (LEVEL_F)	Magnetic field data resampled to 1s and 64 s averages. PSA folder: RO-{target}-RPCMAG-4-{pppp}-RESAMPLED-V{v} Data files: RPCMAG{YMMDD}_CLF_{SS}_A{average}.*
Magnetic field	nT	RPC-MAG-OB RPC-MAG-IB	L4	CELESTIAL (LEVEL_G)	Magnetic field data resampled to 1s and 64 s averages. Data contain spacecraft positions as well PSA folder: RO-{target}-RPCMAG-4-{pppp}-RESAMPLED-V{v} Data files: RPCMAG{YMMDD}_CLG_{SS}_A{average}.*
Magnetic field	nT	RPC-MAG-OB	L4	CELESTIAL (LEVEL_H)	Magnetic field data resampled at original sampling rate of 20 Hz. Reaction Wheel disturbance eliminated. Data contain spacecraft positions as well. PSA folder: RO-{target}-RPCMAG-4-{pppp}-RESAMPLED-V{v} Data files: RPCMAG{YMMDD}_CLG_OB_M3.*

2.9 Illumination maps (RPC-PIU)

The purpose of the illumination maps is the visualisation of the conditions of illumination at 67P for a given configuration between the comet, the spacecraft and the Sun. The shape of the comet, so called shape model, has been reconstructed with the images acquired by the different instruments (NAVCAM and OSIRIS) on board Rosetta. For this work, we have used the shape model from ESA/NAVCAM available here:

```
ftp://psa.esac.esa.int/pub/mirror/INTERNATIONAL-ROSETTA-MISSION/SHAPE/  
RO-C-MULTI-5-67P-SHAPE-V2.0/DATA/TRIPLATE/SPC_ESA/MTP019/  
CSHP_DV_130_01_LORES_OBJ.OBJ
```

The shape model is made of 52098 nodes and 104192 facets

The shape model is divided in two parts:

- the lines starting by the character "v": they are the positions (x,y,z) of the nodes considered for mapping the surface of the comet,
- the lines starting by the character "f": these lines contain the nodes which you have to link together to make a facet. One facet, in the shape of a triangle, requires three nodes.

A given position of the Sun in the rotating frame of the comet is identified by the longitude XXX and the colatitude YYY of the subsolar point in the rotating frame of the comet, given in degrees, where XXX and YYY are 3 digits including leading zeroes (e.g., 3° corresponds to 003). For each subsolar point, we calculate the cosine of the angle between the normal of the facet and the Sun direction, taking into account self-shadowing effects. The values are set to 0 if: either they are lower than 10^{-5} or the facet is completely shadowed (i.e., the three nodes are in the shadow). The values of the cosine of the angle are sorted in the same order as the facets in the shape model.

We have generated maps for each degree in longitude (between 0° and 359°) and colatitude (between 38° and 142° because of the obliquity of the comet, 52°, meaning that the subsolar point cannot be lower than $90^\circ - 52^\circ$ or higher than $90^\circ + 52^\circ$). We preferred to use the colatitude instead of the latitude (colatitude=90°-latitude) for the convenience to be a positive value, and for the filename. As the same conditions of illumination are encountered several times due to the rotation of the comet, it is more relevant to provide illumination maps with respect to the configuration comet-Sun instead of the time. In total, we have produced 37800 maps. For comparison, throughout the mission, generating 1 map for every minute corresponds to more than 1 million maps.

2.9.1 List of dataset

The different products are available through different formats on the PSA.

Table 2.20: List of available files regarding the illumination maps (XXX is the longitude in degree and YYY is the colatitude in degree, coded over 3 digits)

Filename	Description
ASCII_XXX_YYY.LBL	Header for ASCII_XXX_YYY.TAB Following PDS3 requirement
ASCII_XXX_YYY.TAB	Cosine of the solar zenith angle of the corresponding facet, sorted as the facets in the shape model
MAP_XXX_YYY.LBL	Header for MAP_XXX_YYY.FIT Following PDS3 requirement
MAP_XXX_YYY.FIT	Projection "plate carrée" of the illuminated surface of the comet for a given configuration comet-Sun. Although this projection is supposed equidistant, as the comet is not a sphere, that property is not applicable. The resolution of the image is 6000×3000 . The bottom left of the image correspond to -180° in longitude and -90° in latitude, the top right to 180° in longitude and 90° in latitude.
PREVIEW_XXX_YYY.LBL	Header for PREVIEW_XXX_YYY.JPG Following PDS3 requirement
PREVIEW_XXX_YYY.JPG	Their main purpose is displaying the image as it is in the .FIT files with the addition of axes and title. No DATA folder but in BROWSE folder.
TIME2SUN.LBL	Header for TIME2SUN.TAB Following PDS3 requirement
TIME2SUN.TAB	Correspondence between the maps and time during the mission with one minute timestep. For each minute of the mission, from the 1 st of August 2014, 00:00:00, to the 30 th of September 2016, 23:59:00, the file provides the closest illumination map at that time, within one degree in longitude and latitude, i.e. rounded towards the closest integer.

For each set of subsolar colatitude and longitude, we have created one ASCII file in order to offer the possibility to the users to generate their own 3D representation of the comet with the right illumination. There is one file per subsolar coordinate, so when there is degeneracy in the longitude and latitude, the file given is associated with the most illuminated facet. Because of the degeneracy of the longitude and latitude (several parts of the comet share the same longitude and latitude, especially for the small lobe, see Fig. 3.22 in the section dedicated to the caveats), we privilege for the representation to put in the foreground the facets with the highest illumination.

The 2D-illumination maps have been successfully compared with the maps, which Bernhard Geiger (ESA, personal communication) generated for validation of this activity. These latter maps are however not readily available from the ESA website. It was the reason why we have decided to systematically generate them and make them available to the scientific community.

2.9.2 Additional information

Table 2.22: List of additional quantities provided within the label.

ROSETTA KEYWORDS	Unit	Description
ILLUMINATED_SURFACE_AREA	km ²	Illuminated surface area of the comet; the facet area is included if at least one of its nodes is illuminated.
ILLUMINATED_SURFACE_PERCENTAGE	%	Ratio between the non-weighted illuminated surface area and the total surface area of the comet.
ILLUMINATED_SURFACE_AREA_WEIGHTED	km ²	Illuminated surface area of the comet weighted by the cosine of the solar zenith angle (0 if in the shadow).

For convenience to the user, we have generated an ASCII file, TIME2SUN.TAB, in order to link a given period during the cometary mission phase, to the relevant illumination products.

Previews (JPG format named: PREVIEW_XXX_YYY.JPG) are visible on the PSA. For each associated dataset, MAP or ASCII, the projection of the illuminated surface is displayed in an inset with title and axes, as illustrated in Fig. 2.13.

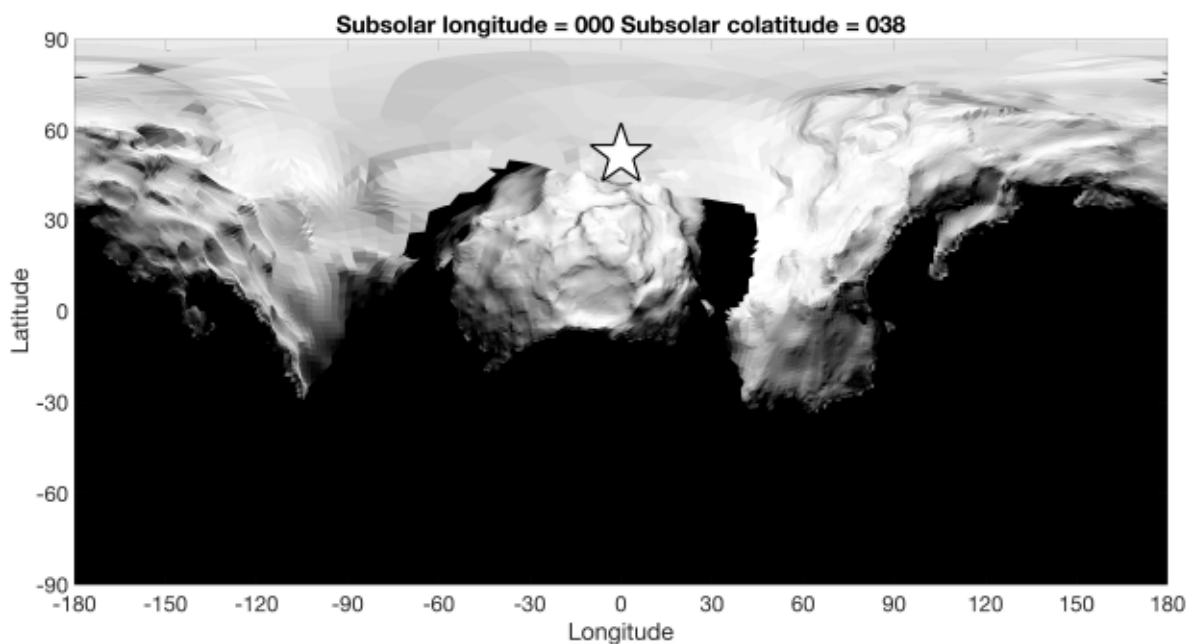


Figure 2.13: Example of preview displayed on the PSA

FIT is a standard format for image in astronomy. FIT files available for download represent the illuminated surface, following a plate carrée projection, for a given configuration, illustrated in Fig. 2.14.



Figure 2.14: Example of FIT



Figure 2.15: Colourscale for the illumination and the corresponding value of the cosine of the angle between the normal of the facet and the sun direction. For the FIT file, the intensity of one pixel is coded over 8 bytes, i.e., the values are between 0 and 255 in decimal basis. In order to retrieve the corresponding cosine, the value in the FIT file has to be divided by 255.

The correspond colourscale of the FIT and JPG files is displayed in Fig. 2.15.

Chapter 3

Science use of the data, examples and associated caveats

3.1 The Ion Composition Analyzer (RPC-ICA)

3.1.1 Science use of the data

Measurements of solar wind ions

RPC-ICA can be used to study solar wind ions and how they are affected by the comet environment. This is in particular described in a series of papers (Behar et al., 2016a,b, 2017) describing the solar wind deflection. Even though significantly deflected, the solar wind mostly forms a well-defined beam, and calculating velocity moments is usually straightforward even though one must take the limited field of view into account. ICA can resolve H^+ , He^+ and He^{2+} . The density can typically also be well determined.

Estimates of the neutral atmosphere

Charge exchange of He^+ to He^{2+} allows for studies of the neutral atmosphere (Hansen et al., 2016; Nilsson et al., 2015a; Simon Wedlund et al., 2016) as the He^+ to He^{2+} ratio is a measure of the integrated atmospheric density the He^{2+} ions has passed through.

Measurements of cometary ions

RPC-ICA can also be used to study cometary ions and how they are affected by the solar wind and other phenomena. The first pick up detection of ions was described in Nilsson et al. (2015a) with further descriptions of the cometary ion flow directions shown in Nilsson et al. (2015b, 2017). The latter studies established that most observed ions have a significant anti-sunward component. The relation between cometary and solar wind ion flow was described in a case study (Behar et al., 2016a), whereas Berčič et al. (2018) described how cometary ions at low energy and observed relatively close to the nucleus were expanding radially in the YCSEQ-ZCSEQ plane, while more energetic pick-up ion motion in the same plane was controlled by the solar-wind electric-field direction. Both ion populations had a significant anti-sunward motion. In another study, Nicolaou et al. (2017) studied energy-angular dispersion of cometary ions, and found that these only sometimes were consistent with a gyration of the ions. In other cases they suggested that inhomogeneity of the electric and magnetic fields along the particle orbit could give rise to the observed dispersion.

Studying fast changes in the unstable cometary environment

High time resolution data from RPC-ICA can also shed light on variations in the spacecraft potential (Odelstad et al., 2017; Stenberg Wieser et al., 2017) and other fast variations in the comet environment. Frequently a co-variation between magnetic field strength, plasma density as determined from the LAP or MIP instruments and ion fluxes as observed by RPC-ICA can be observed (Stenberg Wieser et al., 2017).

Density at low energy

Measurements of low energy ions are affected by the spacecraft potential, by the lower limit of the energy range of RPC-ICA and by the restricted angular coverage of the instrument at low energy. Therefore studies of low energy ions represent a special challenge. Flow directions are almost certainly strongly affected by the spacecraft potential when the ion energy and the spacecraft potential are in the same range.

3.1.2 Example of the dataset

As discussed in more detail in the RPC-ICA User Guide the instrument initially suffered from automatic shut-downs and associated restricted operating hours, as well as data corruption giving frequent shorter time period data gaps. The situation improved with time, so to get started it may be better to look at data from perihelion and onward. In particular data is better after 1 November 2014 when the energy tables were updated. The overview given in Nilsson et al. (2017) can be used to find the type of data one wish to study. An example used in the RPC-ICA User manual is 2016-03-09 which consists of standard 3D data with full energy range. The data show H^+ , He^+ and He^{2+} of solar wind origin as well as cometary ions accelerated up to approximately the energy of the solar wind ions.

Data for the common RPC sample day of 30 July 2016 is shown in Figure 3.1.

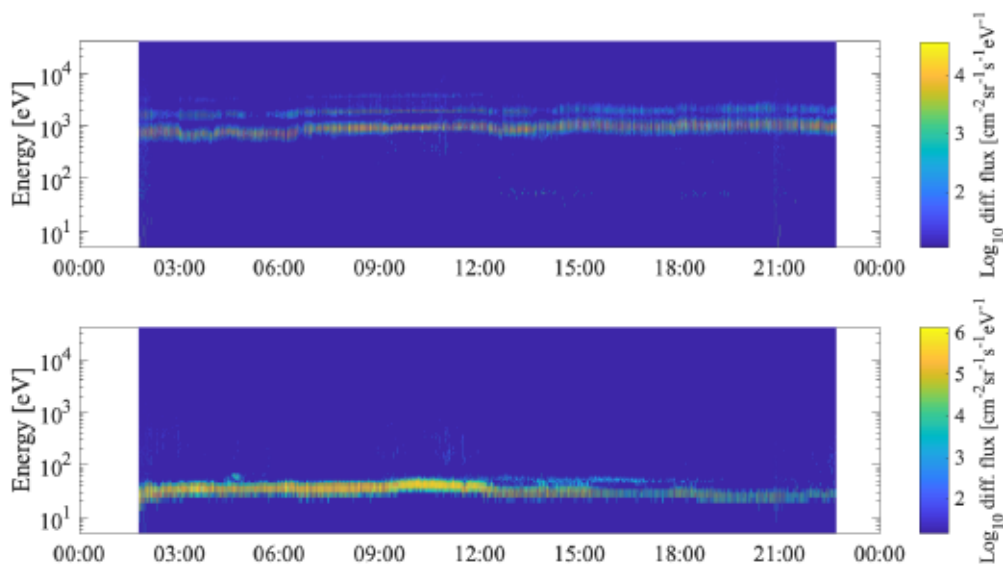


Figure 3.1: Ion energy spectrograms (Level 3) from the RPC-ICA instrument, with time on the X-axis, energy on the Y-axis and the colour scale gives the logarithm of the differential ion flux. The upper panel shows solar wind ions (H^+ , He^+ , He^{2+}) and the lower panel shows cometary ions (water group ions and heavier).

During the sample day the onboard loss-less compression of RPC-ICA data was inefficient. This was due to a higher than usual degree of background noise. The plotted data has been treated with a simple noise-removal procedure where data points with less than two counts has been set to zero. Because of inefficient data compression the mode of the instrument quickly increased to a mode number in the range from 20 to 22, with a corresponding mass resolution of only 2 - 4 mass bins. This means that it is not really possible to distinguish different solar wind ions from each other using mass data. Separation of heavy ions of cometary origin and solar wind ions still works well. From inspection of the solar wind ions one can see that by using the energy information, H^+ , He^+ and He^{2+} can still be separated, by a manual selection of energy ranges over the day, as can frequently be done for the RPC-IES instrument.

A quite intense low-energy population dominates throughout the sample day for the cometary ions. The low energy border of this population corresponds to the spacecraft potential: this can be judged with some confidence from the RPC-LAP estimates of the spacecraft potential (see panel, Fig. 3.9). There is not sufficient mass information available to distinguish between the main (water group) heavy ion population and heavier ions in the mass range of CO_2 , though such a separation is possible on different days/modes

RPC-ICA has a limited field of view, in particular at low energy, and a lower limit of its energy range, both factors that make it likely that RPC-ICA will underestimate the density of the cometary ions. In Figure 3.2, we present moment calculations for cometary ions, assuming the mass of water, and for solar wind ions, assuming the mass to be that of protons. The moments are integrations over the available energies and directions. The upper panel shows the number density of solar wind and cometary ions and the lower panel, the velocity of the cometary ions.

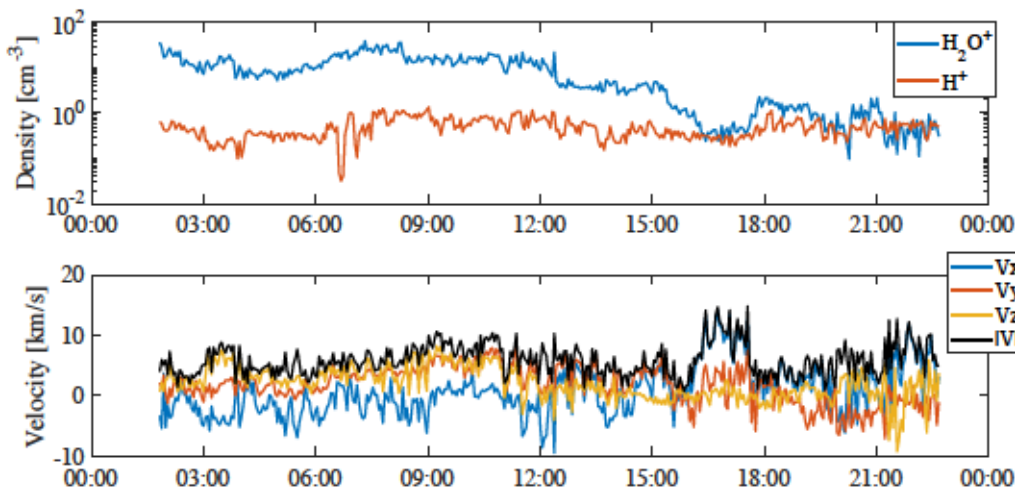


Figure 3.2: Upper panel: Number density (from Level 3) of the cometary ions (blue line) and of the solar wind ions (red line), obtained through integration of the observed fluxes [cm^{-3}]. Lower panel: Bulk velocity (from Level 3) of the cometary ions [$km \cdot s^{-1}$]. Note that these may be strongly affected by the spacecraft potential as well as restricted field of view.

The solar wind density is around 0.1 cm^{-3} which is about what can be expected for the solar wind at a heliocentric distance of more than 3 AU. The cometary ion density estimate is around 10 cm^{-3} in the denser parts, and at about 16 UT even drops to solar wind levels. This is much below the estimates from MIP and LAP which are in the range of about 100 to 1000 cm^{-3} (see Sections 3.3.2 and 3.4.2). The velocity moments of RPC-ICA may be unreliable if the spacecraft has a negative charge similar to the ion energy observed. Still, one may note that the net velocity

is an anti-sunward flow of about $10 \text{ km}\cdot\text{s}^{-1}$, which is quite typical (Berčič et al., 2018; Nilsson et al., 2015b, 2017). This may indicate that for this case, RPC-ICA is mainly observing an accelerated cometary plasma, and the more locally produced denser plasma is below the energy threshold of RPC-ICA (thus indicating a not so negative spacecraft potential) or outside the field-of-view of RPC-ICA. Nominally, RPC-ICA does look toward the comet direction for this and most cases, but the elevation sampling is coarse at low energies, so a narrow beam of ions can maybe still be outside the field-of-view of the instrument.

3.1.3 List of caveats

RPC-ICA data may contain a few types of known problems. The most notable as yet unexplained types of data include a real-looking signal below the spacecraft potential, possibly sometimes at invalid energy analyser settings which should not yield any external signal. These signals were mentioned in Nilsson et al. (2017) and are described in more detail in the RPC-ICA User Guide.

3.2 The Ion and Electron Sensor (RPC-IES)

3.2.1 Science use of the data

Examples of the results of analysis can be found in the following published papers.

Studies of solar wind electron distributions

Broiles et al. (2015)
Madanian et al. (2016)
Clark et al. (2015)

Discovery of negative ions in the coma

Burch et al. (2015)

Survey of coma plasma measurements

Goldstein et al. (2015)
Goldstein et al. (2017)

Identification of plasma boundaries

Mandt et al. (2016)

3.2.2 Example of dataset

Examples of energy-time spectrograms for electrons and ions measured by RPC-IES on 30 July 2016 are shown in Fig. 3.3. Rosetta was ~ 3.5 au from the Sun and ~ 9 km from CG during this day. The electron population was primarily at energies < 200 eV. Higher count-rates are seen early in the day. The ion spectrogram shows the solar wind, with the protons at ~ 1 keV and alpha particles at twice that energy. A number of abrupt changes in energy appear. The band of very low energy (~ 10 eV) ions are locally ionized (e.g., water, CO_2). Their high energies result from the negative spacecraft potential which attracts them.

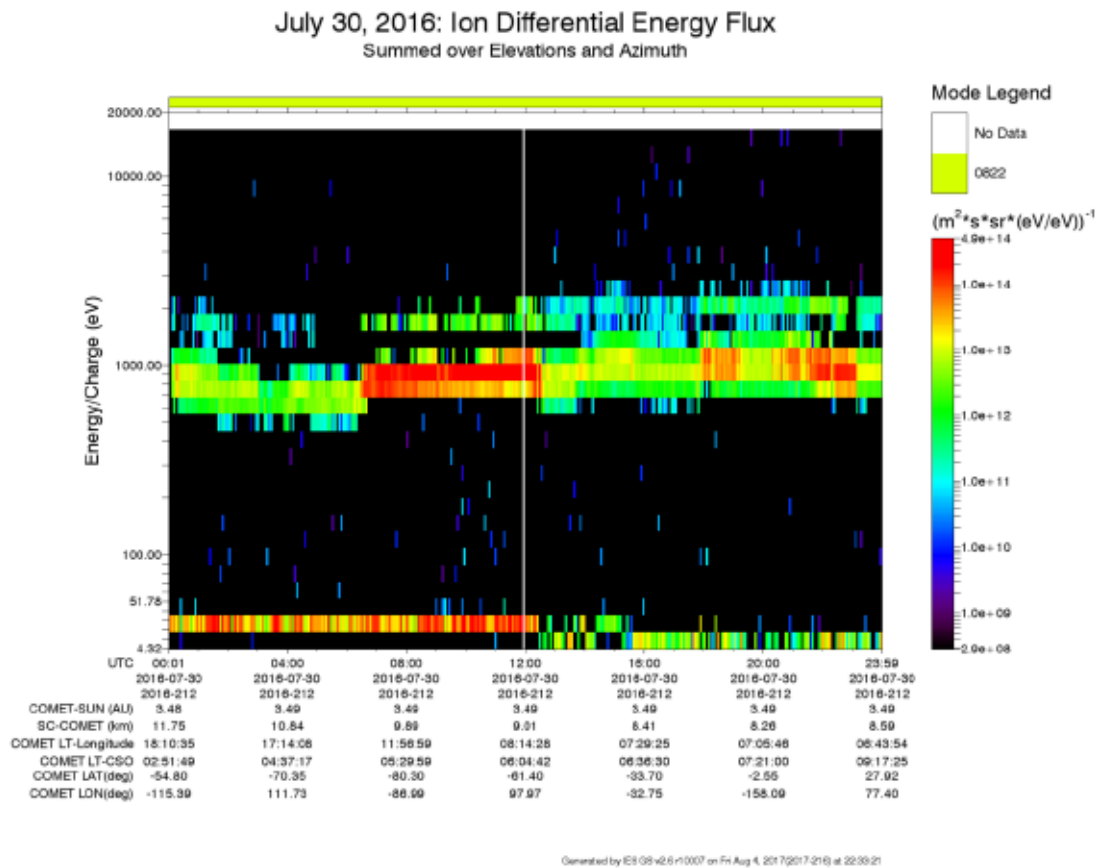
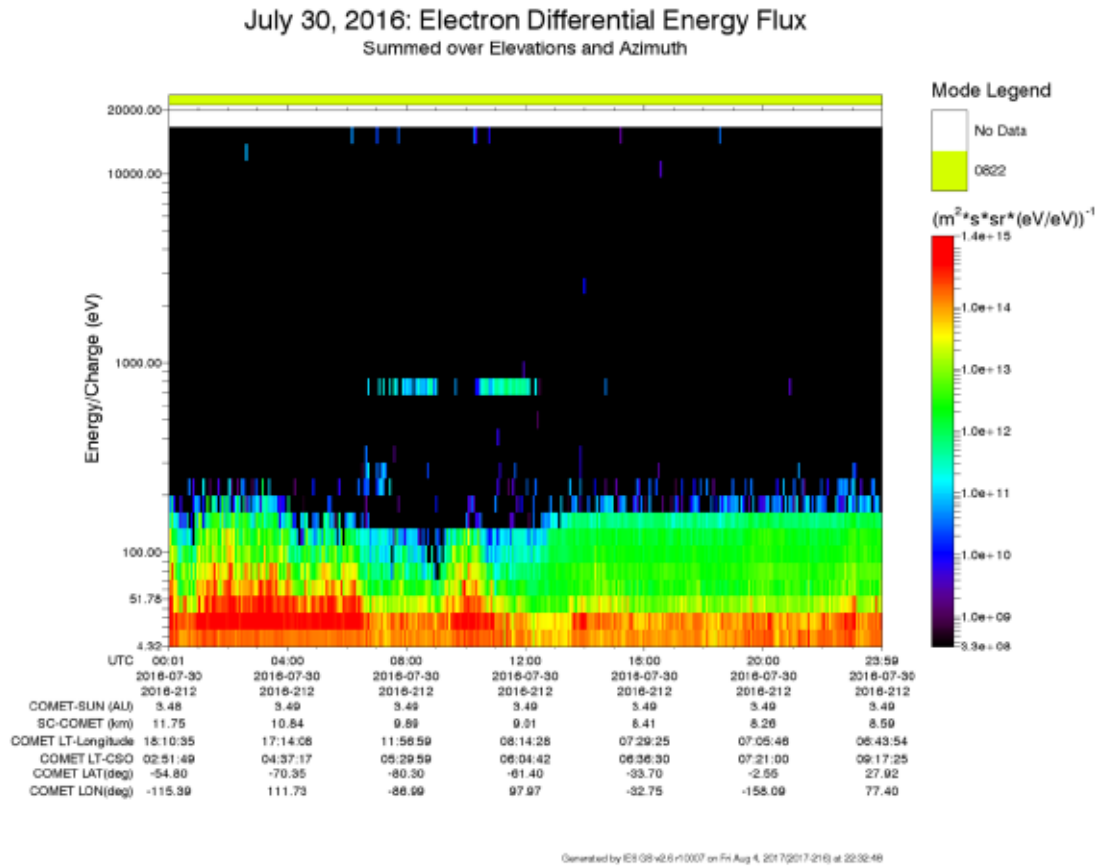


Figure 3.3: Energy-time spectrogram of electrons (upper) and ions (lower) on July 30, 2016. These are counts-s⁻¹, L3 data.

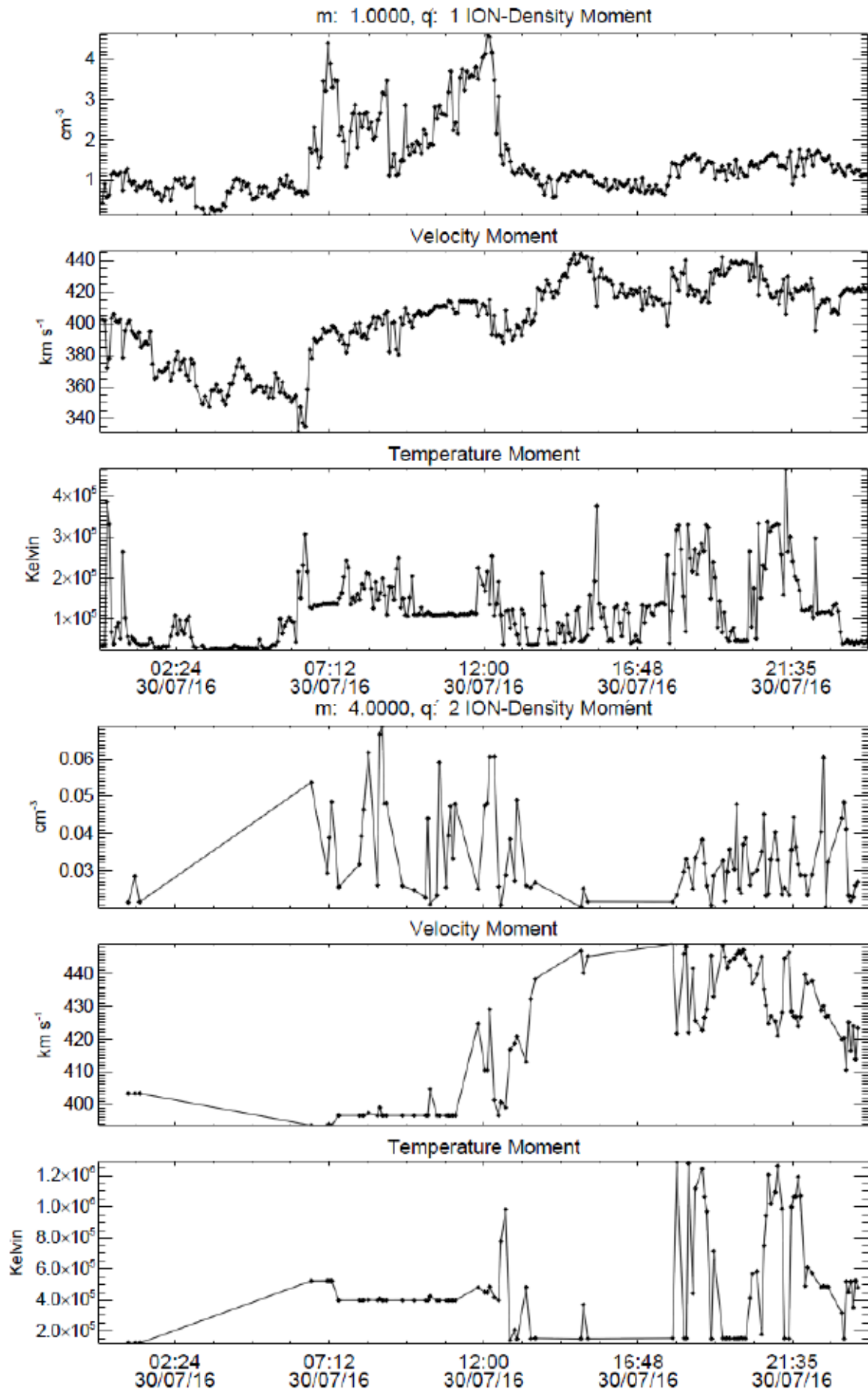


Figure 3.4: Zeroth-, first- and second-order moments for protons (top) and alphas (bottom panel).

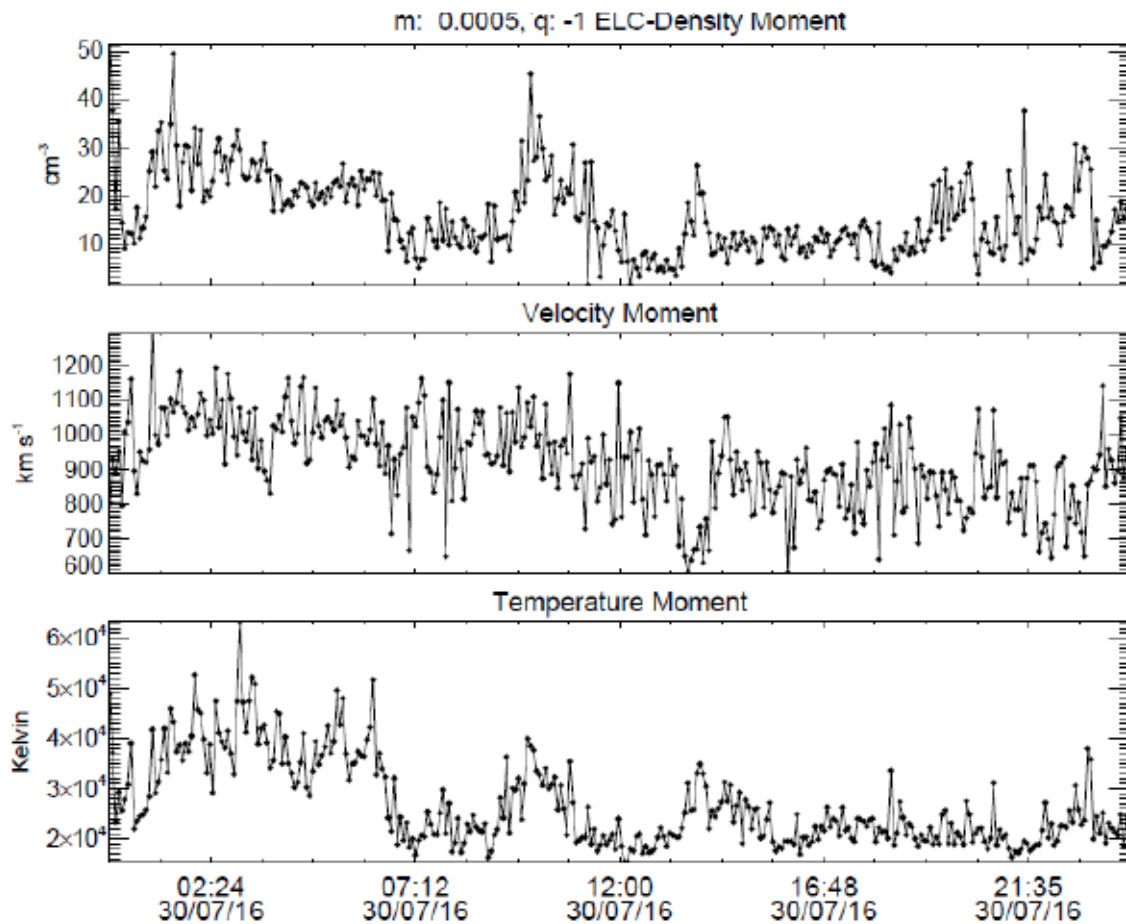


Figure 3.5: Zeroth-, first- and second-order moments for electrons.

3.2.3 List of caveats

There are several issues that the user of IES data needs to be aware of and understand before processing and interpreting the data. These are described in Section 2.5, “Data Caveats” within the EAICD.

Additionally, data are marked with quality flags that describe either specific characteristics of data, the non-nominal state of the instrument at that time or spacecraft pointing with regards to IES. The quality flags are described in each label file associated with data files and relate to (1) MCP Voltage, (2) Sun Pointing, (3) Interference from the RPC-ICA instrument, (4) Transition Cycle, and (5) Enhanced counts due to possible penetrating radiation.

Blockage of Some Elevation Angle Bins

Several spacecraft structures and parts of other instruments block the RPC-IES FoV in portions of the most negative elevation angles (see Fig. 3.6). In particular, note that the positions of the solar arrays and the High Gain Antenna (HGA) in the RPC-IES FoV vary throughout the mission.

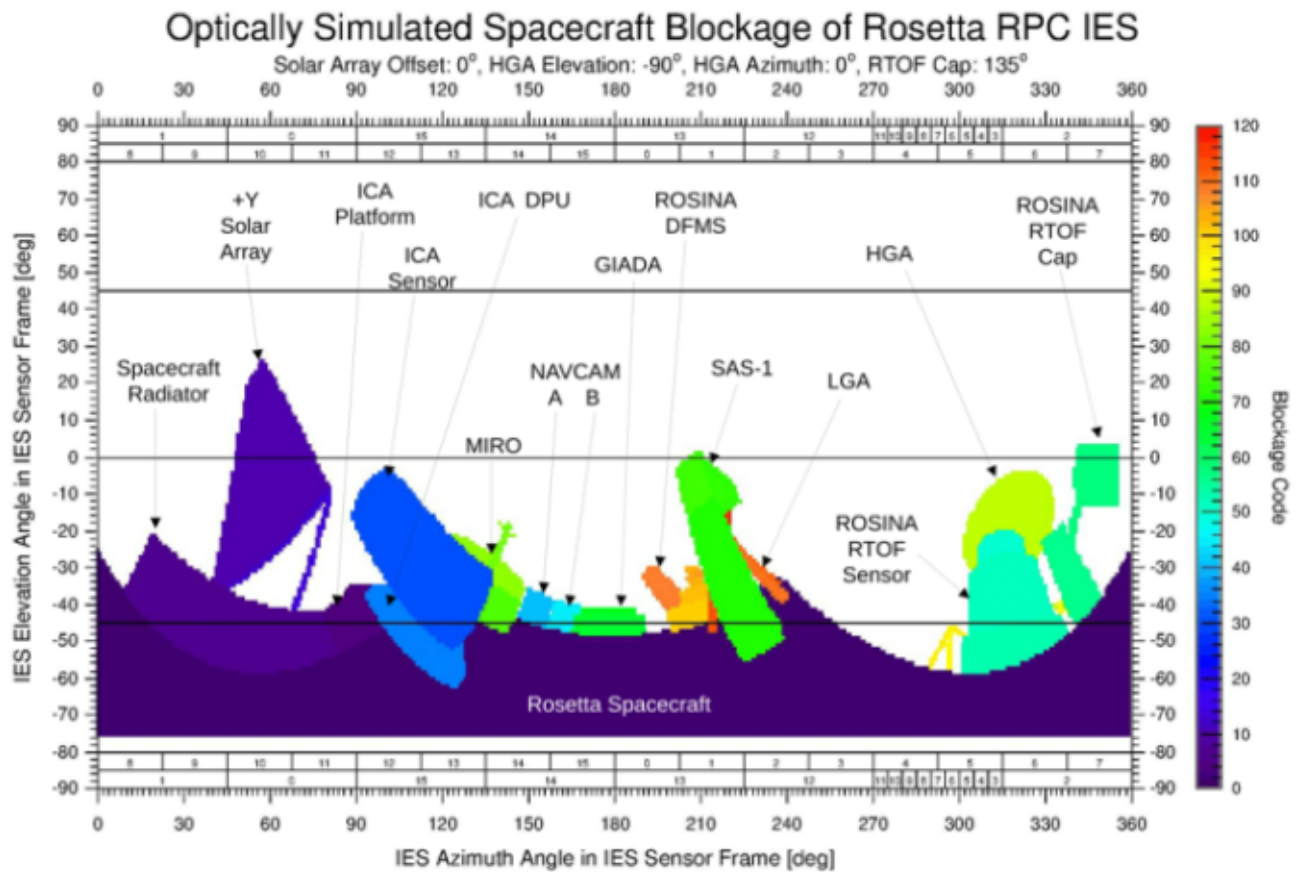


Figure 3.6: Positions of the different elements of Rosetta in the field of view of RPC-IES, with respect to its reference frame. From Clark et al. (2015)

Individual Anode (Azimuth) Characteristics

Sometimes anode data are combined on board in certain operating modes because of telemetry limitations. In those cases each of the anodes is given identical values (sum/number of anodes).

Ions

Anodes 13 and 14 are often noisy so caution is recommended when using data from them.

The so-called “fine anodes” (3 - 11) are sometimes combined on board in certain operating modes because of telemetry limitations. In those cases each of these 9 anodes are given identical values (the sum/9).

The data from individual fine anodes, when provided, suffer from crosstalk between these anodes and thus may not be reliable.

It was discovered after launch, apparently as a result of a light leak, that when the Sun is incident between anodes 2 and 3, a high count rate is seen in anode 12. It is also seen in anode 13 when counts in 12 and 13 are combined.

Electrons

Occasionally the electron data exhibit a signal at narrow energy ranges between 200-2000

eV, appearing as short dashes in spectrograms, as a result of interference from a neighbouring instrument (ICA). The occurrences are indicated in the flag column.

Anode 11 (azimuths from 67.5° to 90°) became noisy shortly after launch and since 16 September 2007 data from that anode have not been downloaded. In those operating modes for which data from 2 or more anodes are combined will result in the absence of data from one or more anodes adjacent to number 11.

In April 2015, the electron sensor's response began to change, especially anodes 8-15 started to measure reduced differential energy flux at low energies (Broiles et al., 2016). It may come from an issue in the altered amplifier and associated with these anodes from April 2015 onwards should be used with caution.

Users of RPC-IES level 5 data should proceed with caution and understanding that different electron populations are not separated in the moments data files. The electrons measured by RPC-IES near comet 67P coma consist of several populations from different sources. The quiet solar wind typically contributes 3 separate populations (the core, halo, and strahl). Transients in the solar wind contribute other distributions. Photoionization of material from the comet nucleus produces other populations and electron collision ionization produces more electrons. These populations interact and blend with each other, producing a complicated mess. In addition, the spacecraft is generally charged negatively, typically the order of 10-20 V, resulting in an apparent distortion of the distributions when measured by a Rosetta-based instrument. Another important aspect that may occasionally affect the quality of the data is due to the IES field of view (FOV) being $\sim 2.8\pi$, not covering all of space. The result is that as the spacecraft turns, IES may see different electron populations during the course of the turn. This is not significant for solar wind protons since they are normally either in or out of the FOV.

Several investigators have studied the electron distribution in detail using IES electron data (Broiles et al., 2016; Clark et al., 2015; Madanian et al., 2016) shown the complexity of these distributions. Separating the populations into individual distributions over the whole mission is a task beyond the funding and time available to the IES team and therefore the level 5 files contain unseparated electron populations.

Users of RPC-IES electron moments data should have an understanding of this issue and proceed with caution.

Correction for the spacecraft potential

Once the L3 electron differential energy flux $I(E, \theta, \phi)$ (θ and ϕ refer to elevation and azimuth angle in the instrument frame) has been derived, one needs to correct for the spacecraft potential, V_{SC} (Odelstad et al., 2017), which is measured by the RPC-Langmuir Probe (LAP) (Eriksson et al., 2007). Applying the Liouville's theorem, the correction of I is given by (e.g., Galand et al., 2016):

$$I(E, \theta, \phi) = \frac{E^2}{E_{IES}^2} I^{IES}(E_{IES}, \theta, \phi) \quad (3.1)$$

where $E = E_{IES} - V_{SC}$ and E_{IES} is the electron energy measured by RPC-IES. Note that in Galand et al. (2016), the relation is given in terms of the particle flux (= energy flux / E), hence the introduction of the square of the energy in Eq. 3.1.

As for most of the escort phase, the spacecraft potential was negative (Odelstad et al., 2017), this means that part of the electron population which should have been seen in the absence of a spacecraft potential is going to be missed. Indeed, for a spacecraft potential of -10 V, electrons with an energy ($E = 27$ eV) are going to be detected at $E_{IES} = 27 + (-10) = 17$ eV, while electrons with ($E = 12$ eV) are going to be missed (indeed, in that case, $E_{IES} = 12 + (-10) = 2$ eV, below the energy range of the first bin).

The electron-impact ionisation frequency, ν_n^e , of the neutral species n is derived from the electron particle flux J , as follows (e.g., Galand et al., 2016):

$$\nu_n^e = \int_{E_{th}}^{E_{max}} \sigma_n^{e,ioni}(E) J(E) dE \quad (3.2)$$

where E_{th} and $\sigma_n^{e,ioni}(E)$ are the ionisation energy threshold and the total electron-impact ionisation cross section of the neutral species n , respectively, and E_{max} is the maximum energy considered (typically a few hundreds of eV). The electron particle flux [in $m^{-2}\cdot s^{-1} eV^{-1}$] is derived by applying Eq. 3.1 to the electron differential energy flux I for correcting for V_{SC} , then dividing by E , and finally integrating over elevation and azimuthal angles. Isotropy is assumed over the missing field of view.

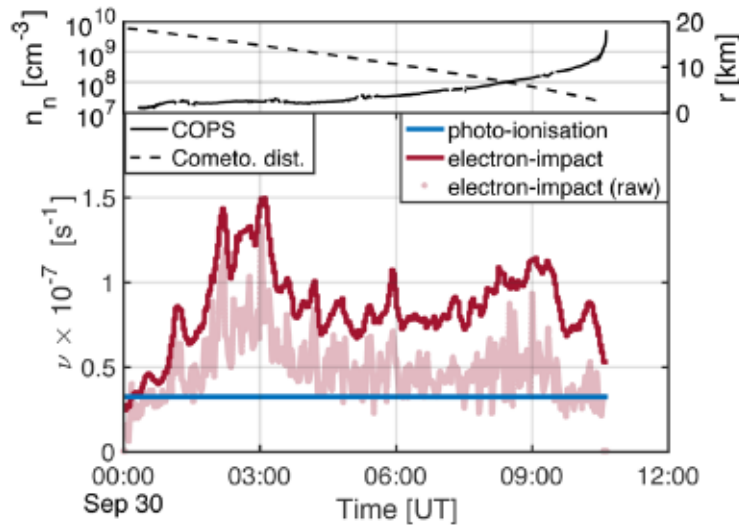


Figure 3.7: Top: Time series of the ROSINA-COPS neutral number density (full line) and cometocentric distance (dashed line) on 30 September 2016 (End of mission). Bottom: Time series of the photo-ionisation frequency at comet 67P (3.8 au) (blue curve), electron-impact ionization frequencies corrected with the spacecraft potential (red curve) and uncorrected (pink dots). Pure water has been assumed for the neutral composition. [After Heritier et al. (2017)]

Fig. 3.7 highlights the effect of the correction for the spacecraft potential on the electron-impact ionisation frequency. In pink, the ionisation frequency derived from RPC-IES electron energy differential flux without correction by V_{SC} and in red, with correction. The frequency not corrected by V_{SC} is highly structured and seems very noisy, while once corrected for V_{SC} the variation over time is smoother, the high-frequency structure disappears (Heritier et al., 2017).

In order to validate the analysis of the RPC-IES electron differential flux as well as to identify the source and loss processes of the cometary plasma, we have applied a multi-instrument analysis to the RPC and Rosetta Orbiter Spectrometer for Ion and Neutral Analysis (ROSINA) dataset (Galand et al., 2016; Heritier et al., 2017, 2018). At large heliocentric distances (> 2 au) to which

the analysis has been applied, the continuity equation is reduced to the balance between the ionisation rates and plasma transport (Galand et al., 2016).

The multi-instrument analysis which links the modelled electron density derived from the neutral density and composition from ROSINA and electron-impact ionisation frequency from RPC-IES (corrected for the spacecraft potential by RPC-LAP), to the electron density observed by RPC-Mutual Impedance Probe (MIP) (Trotignon et al., 2007) and RPC-LAP (Eriksson et al., 2007). An overview of the analysis is given in Fig. 2 of Galand et al. (2016).

Galand et al. (2016) showed that during the pre-perihelion phase, over the summer, northern hemisphere photo-ionisation was a prime source of ionisation, while over the southern hemisphere electron-impact ionisation was often dominant and some structures seen in the measured electron density were driven by similar structures in the ionisation electron population measured by RPC-IES. During post-perihelion, Heritier et al. (2018) found that electron-impact ionisation was the main source of ionisation at most times analysed. They also showed that during post-perihelion the analysis not only held during quiet conditions up to 70 km, but also during solar events. Heritier et al. (2017) applied this multi-instrument study at the end of mission all the way down to the surface. The electron densities from RPC observations and from the model (upgraded in terms of the neutral number densities, as required for comparing with observations close to the surface) agree well (see Fig. 3.8); close to the surface the adiabatic expansion of the neutral gas needs to be taken into account in order to explain the observed electron density. Here again, some structures seen in the electron density, such as near 10:00 UT, are driven by the ionising electrons measured by RPC-IES and driving the electron-impact ionisation frequency (see Fig. 3.7).

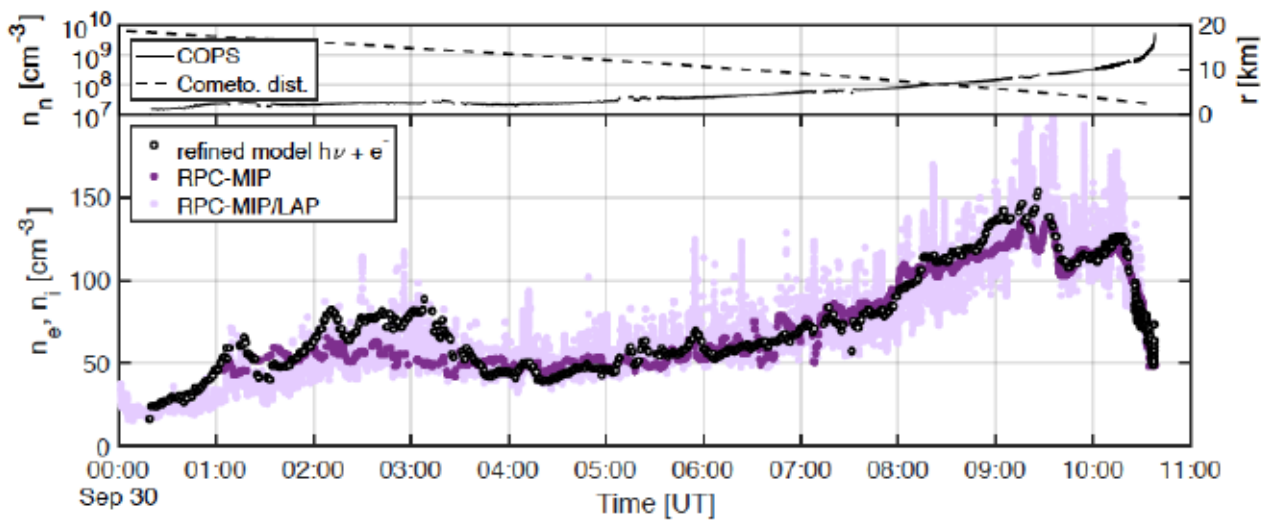


Figure 3.8: Top: Time series of the ROSINA-COPS measured neutral number density (full line) and cometocentric distance of the spacecraft (dashed line). Bottom: Time series of the preliminary RPCMIP electron number density (dark purple dots), preliminary RPCMIP/RPCLAP cross calibrated densities (light purple dots) (final versions of both density datasets are available on the PSA). Refined modelled ionospheric densities using a neutral gas expansion model calibrated on ROSINA-COPS measured densities at Rosetta (black circles) [After Heritier et al. (2017)]

3.3 The Langmuir probe instrument (RPC-LAP)

3.3.1 Science use of the data

Low time resolution measurements of plasma density and electron temperature

These fundamental quantities can be derived from the RPC-LAP bias voltage sweeps, typically performed every 160 s in most operational modes but sometimes more often. Much discussion of this method can be found in Eriksson et al. (2007). It has also been used, e.g., by Edberg et al. (2015) for plasma density profiles close to the nucleus, by Vigren et al. (2016) for modelling the early activity phase and by Yang et al. (2016) for the first activity of the comet.

It should be noted that plasma density values can also be obtained from RPC-MIP, RPC-ICA and RPC-IES. The relation between the various RPC plasma density values is discussed in Section 2.3.

High time resolution measurements of plasma density variations

The RPC-LAP measurements of probe currents in between sweeps, or of probe voltage when the probes are in bias current (E-field) mode, can be used to follow the plasma density variations at high-time resolution (up to 57.8 samples·s⁻¹). Calibrations to RPC-LAP sweeps, RPC-MIP density values or assumptions on particle energy (electron temperature or ion drift speed and composition) are needed for converting these to plasma densities. This has been used by e.g. Heritier et al. (2017) (using probe voltages) and Engelhardt et al. (2018b) (using voltages and currents) at the comet, and by Edberg et al. (2009) (using voltages) at the Rosetta Mars flyby.

Measurement of ion energy/flow speed

The Langmuir probe bias voltage sweeps can be used to derive the ratio of ion density to ion momentum. With density either from the electron side of the sweep or from RPC-MIP and with an assumption on ion mass, an effective ion speed can be derived, combining bulk and thermal motion. This has been done by Vigren et al. (2017) and Odelstad et al. (2018).

Measurements of low frequency E-fields

With two probes in E-field mode, measuring voltage at fixed bias current (which at the comet mostly was zero, i.e. floating probes), the electric field between them can be derived. The use of this for LF data (approximately 1 Hz - 20 Hz) is described by Karlsson et al. (2017) and André et al. (2017).

Measurements of high frequency E-fields

At sufficiently high frequency, the current to a probe will be dominated by the displacement current due to the capacitive coupling of the probe to the plasma. This means that even if the probe has a bias voltage applied so that the probe current is the quantity sampled, it is the wave electric field which is measured. This has been used to study ion acoustic waves to kHz frequencies by Gunnell et al (2016, 2017).

Measurements of spacecraft potential V_{SC}

This can be derived at a time resolution of minutes from the probe bias sweeps, or to fractions of a second by use of a probe in E-field mode. The fundamental reference here is Odelstad et al. (2017), who also compare and cross-calibrate these data to RPC-ICA measurements. The spacecraft potential can provide information on plasma density (Odelstad et al., 2015, 2017) but also be used for interpreting and calibrating particle data (Galand et al., 2016; Heritier et al., 2017, 2018).

Probe photo-electron emission

The photoelectron saturation current depends on the EUV flux, and thus is of interest also for understanding ionization in the coma. Its measurement is discussed in detail, including validation by several different methods, in Johansson et al. (2017).

3.3.2 Example of the dataset

An overview of the RPC-LAP derived quantities and raw data for the common RPC sample day (July 30, 2016) are shown in Fig. 3.9. LAP ran one single macro (known as 416) during all this day. In this mode, the prime sampled quantities are the voltage of LAP1 with respect to the spacecraft and the current flowing from LAP2 to the plasma. From the sweeps performed every 160 seconds on LAP2 (shown in Fig. 3.9, Panel i) we can derive the plasma density n_e (Fig. 3.9, Panel a), electron temperature T_e (Fig. 3.9, Panel b) and spacecraft potential V_{SC} (Fig. 3.9, Panel c). The continuous voltage data on LAP1 (Fig. 3.9, Panel f) also provides a measure of the spacecraft potential V_{SC} (with reverse sign), and the brief snapshots of 2 kHz data taken every 160 s provide wave spectra (Fig. 3.9, Panel j). In addition to the LAP data, Fig. 3.9 also display auxiliary geometry information important for LAP data interpretation (see Panels d, e and h).

The data illustrate several of the issues any user of RPC and LAP data has to consider. The plasma density is probably the quantity a user of LAP data is most interested in. We may immediately note that the LAP sweep-derived densities provided in Panel a are significantly (factor 2-8) higher than the values given by RPC-MIP for the same day (see Section 3.4.2). MIP is in its short Debye length mode (SDL), which cannot measure densities below a few hundred cm^{-3} but has no identified issue with high densities, so the MIP data are in this case considered the more trustworthy. One possible reason for why the LAP sweep density (which here is derived assuming a single electron population at $T_e = 5$ eV) is overestimated in the presence of cold electrons, which drastically can change the sweeps and complicate their interpretation (Engelhardt et al., 2018a; Eriksson et al., 2017). This also implies that T_e estimation in Fig. 3.9, Panel b, is uncertain, as is also indicated by its large spread. However, we may note that the probe voltage (negative of V_{SC}) in Fig. 3.9, Panel f, is clean and well follows the density variation observed by MIP. This means that this day should be suitable for cross-calibration of MIP and LAP, where the LAP1 voltage measurements are used to interpolate the MIP density data to a continuous time series using the procedure applied by Heritier et al. (2017). This procedure can provide a time series combining the higher accuracy of MIP with the better dynamic range and time resolution of LAP. Further discussion of RPC plasma densities and electron temperatures can be found in Sections 2.3 and 2.5.

The power spectra shown in Fig. 3.9, Panel j, give information on the plasma waves. The line around 200 Hz is an interference line, but no issues have been identified with the other low frequency activity seen.

The data also illustrates a not yet understood issue with LAP2 in dense regions after May 2016, producing unexpectedly high ion currents. Fig. 3.9, Panel g, shows the LAP2 current at a fixed bias potential of -27 V (in between the sweeps). While the current follows the general plasma density trend from MIP and also the LAP1 probe potential (Fig. 3.9, Panel a), it has more of short term variations and is surprisingly high. Closer investigation of the raw data on short timescales shows high step-like variations. While the LAP ion current at other times well follows an expected linear relation to the plasma density and therefore is useful as a plasma density measure (Engelhardt et al., 2018a), it often turned out suspiciously high and erratic in dense plasmas, but only after May 2016. Any user needs to treat these data very carefully. It is possible that this is a problem related to the unusually high deviation of the sweep-derived spacecraft potential (Fig. 3.9, Panel c, red/blue dots) from the value we get from the floating LAP1 (grey). However, as a few data points well overlap, this can well be an algorithmic issue which at best can disappear in future data releases. In the meantime, the LAP1 data (panel f) are considered to provide the best estimate of the spacecraft potential, and also agree better with the lower cut-off energy in RPC-ICA data (see Section 3.1.2).

As noted above, Fig. 3.9 also shows auxiliary geometry data of particular interest to LAP. Panel e gives the Cometocentric Solar Equatorial (CSEQ) coordinates of Rosetta and Panel d the Rosetta latitude and longitude in the standard rotating reference frame (CG-CK) of the nucleus. The solar zenith angle (or phase angle, i.e. the angle Sun-Rosetta-nucleus) and subsolar longitude are also shown. The subsolar latitude and the heliocentric distance (both changing slowly) are given as a numbers at lower right.

Fig. 3.9, panel h, indicates the most LAP-relevant of the angles specifying the spacecraft attitude. In nominal pointing, the solar panels are kept perpendicular to the Sun. The Solar Elevation Angle (SEA, black) must then be zero, as it is during all this day. The Solar Aspect Angle (SAA, red) shows how the spacecraft is rotated around the symmetry axis of the solar panel. When $SEA = 0^\circ$, SAA can be used to determine if a LAP probe is sunlit or not. If the red curve enters the upper dark grey region of Panel (c), LAP1 is in shadow behind the solar panels. If it enters the lower dark region in the same panel, LAP2 is in shadow behind the spacecraft body. If it enters the light grey region, LAP may or may not be in shadow behind the high gain antenna, depending on how the latter was directed. The Comet Aspect Angle (CAA) and Comet Elevation Angle (CEA) are defined in the same way, but with respect to the direction of the nucleus instead of the direction to the Sun. To avoid spurious data, stable pointing is preferred. Avoiding periods with varying pointing is usually a good idea, as the varying photo-emission and photo-electron collection currents can be falsely interpreted as plasma variations.

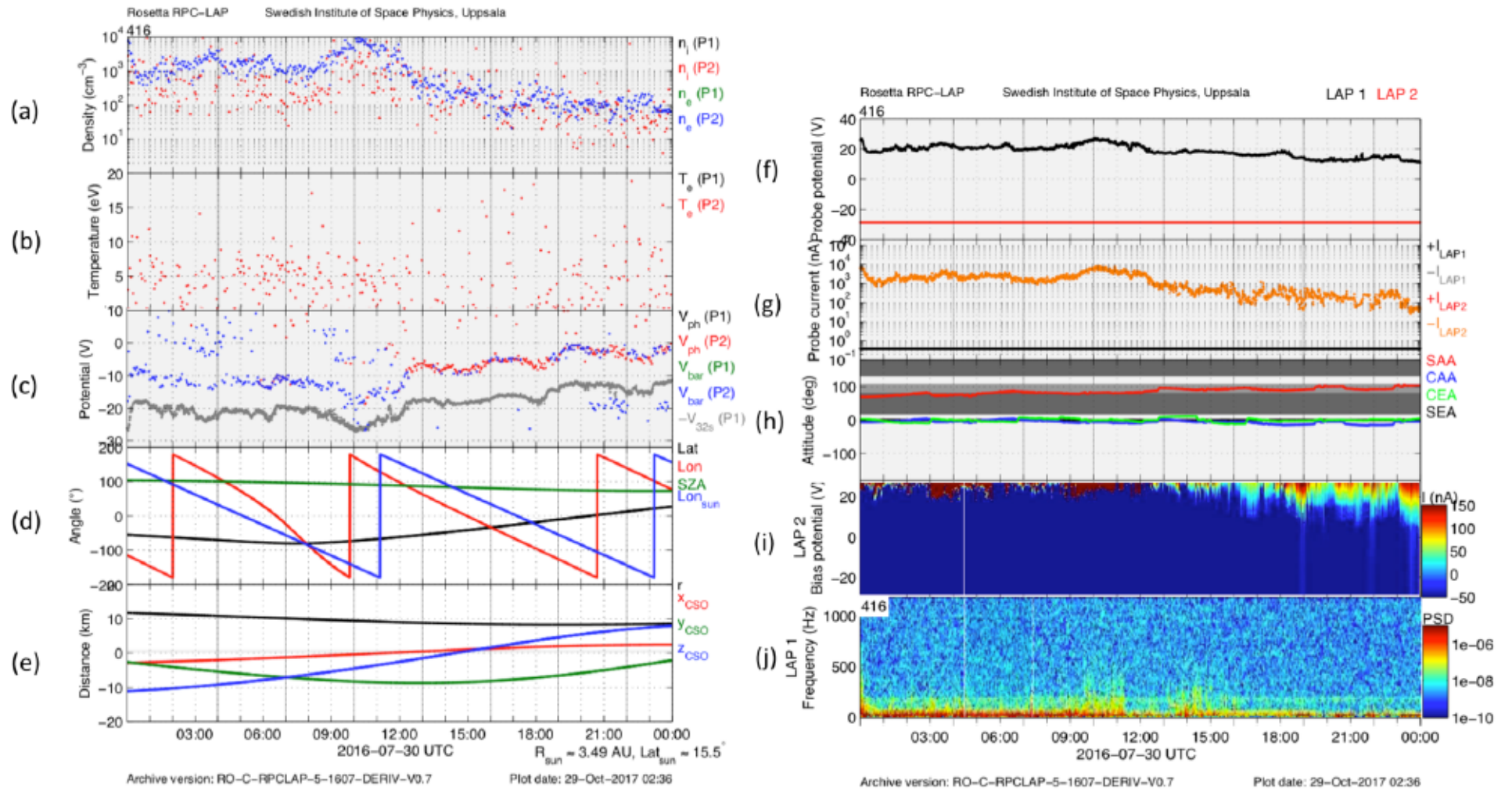


Figure 3.9: LAP derived quantities and Rosetta position during the common RPC sample day (July 30, 2016). Left panel: L5 data. Right panel: L3 data.

3.3.3 List of caveats

Most users should not have to bother about all technical details of the LAP mode concept. However, some orientation is useful to understand what data are available, to make it possible to locate time intervals with mode settings particularly useful for the problem at hand. This section therefore contains first a brief introduction to the LAP mode concept with a typical example, and then some remarks on how to find data suitable to your needs.

LAP macros

As described above, LAP has several different kinds of “modes”, of which the main are:

- Bias modes for each probe (bias voltage sweeps, fixed bias voltage, or fixed bias current);
- High or low sampling frequency range (HF down-sampled from 18.75 kHz and LF down-sampled from 57.8 Hz)
- Telemetry (TM) mode (normal mode NM or burst mode BM)

There were additional analogue settings for, e.g., gain and internal calibration, and the software could be configured for various kinds of digital filtering, averaging and down-sampling. For operational convenience, all these settings were handled by “macros”. These were repetitive command sequences that could be executed by time tagged command. A typical macro provided a mix of bias sweeps with data sampled quasi-continuously between sweeps at low frequency (LF, often 57.8 Hz in BM or 0.9 Hz in NM) and in very short snapshots at high sampling frequency (HF, usually 18.75 kHz). The most common repetition rate was 160 s, making this the typical time between sweeps and HF snapshots. New macros were uploaded to the instrument as new plasma environments were encountered or particular needs arose. All macros are described in the macro table distributed with the LAP documentation in the ESA PSA archive.

An example of the data available from one particular LAP macro is presented in Section 3.3.2. Further details are available in the RPC-LAP User Guide.

Calibration

The primary RPC-LAP data are the currents or voltages of the two probes. All known calibration issues have been compensated for in the level 3 (calibrated) and level 5 (derived) data sets but some remnant errors will inevitably remain. The most important point is that the slowly varying temperature dependent offsets in the analog electronics. Due to these, the absolute accuracy of measured current cannot be guaranteed to better than 1 nA. This means currents of a few nA or less should be treated with caution. The voltage offsets are small compared to the values sampled and can be ignored.

Interference

Wave spectra can show stable narrow lines, obvious signs of interference from other spacecraft systems. These can easily dominate the HF data (the short snapshots sampled at kHz frequency) but are easily recognizable in the data. Interference is rarely an issue for the low frequency data (continuous sampling up to tens of Hz).

The strongest source of HF interference is the RPC-MIP instrument when in its LDL mode (Long Debye length, see Section 1.4), when LAP2 is used for MIP transmission. If making a

spectrum of a HF snapshot in an LDL interval, the signal is usually dominated by the MIP signal, swamping all real signals. However, this is not necessarily the case over all the time interval (few to few tens of ms) covered by the snapshot, so the data may have potential use after careful analysis and removal of periods dominated by interference. Nevertheless, users of LAP HF data are strongly recommended to stick to data acquired in non-LDL modes.

RPC-MIP interference can be found also in the LAP sweeps taken in LDL modes. The analysis algorithms providing plasma parameters from the sweeps attempt to identify and remove bad data points, minimizing this influence. Some caution may still be warranted.

Probe contamination

During most of the mission, LAP2 showed clear signs of surface contamination, visible as hysteresis effects in the sweeps and as a long time constant for settling the probe voltage when switched to electric field mode, both indicative of an RC layer. This can impact the sweeps (shifting the apparent spacecraft potential and reducing the current at positive bias voltage) and the continuously sampled current when at positive probe bias voltage (where the resistance of the plasma sheath around the probe is low, causing a substantial part of the bias voltage to end up over the contamination layer). As a consequence, the measured LAP2 current usually is lower than the LAP1 current when both are operated at positive bias potential. The contamination layer can also shift the LAP2 voltage when a bias current is sent to the probe. However, it has only small impact on the LAP2 current when at negative bias voltage (as the resistance of the plasma sheath around the probe then dominates) and on the LAP2 voltage when the probe is in floating mode (as there flows no current to the probe in that case, so the added resistance gives no appreciable voltage error). For this reason, LAP2 was mainly used in these two modes, where its data usually are good. No contamination issues have been identified on LAP1.

Spacecraft-plasma interaction

The main issue for interpretation of RPC-LAP data is that the probes are not ideal spheres floating freely in space but are mounted on a huge spacecraft, albeit on booms. Perfect shielding of the charges on the spacecraft can rarely be assumed, and the spacecraft emitted photoelectrons as well as wake effects in the flowing cometary plasma adds further complication. Various aspects of this class of issues are discussed by, e.g., Odelstad et al. (2017), Johansson et al. (2016), Eriksson et al. (2017) and Odelstad et al. (2018).

A particularly treacherous effect, illustrated in Figure 3.10, is what variations of the spacecraft potential can do to the current to a LAP probe at positive bias voltage. When the probe is positive with respect to the plasma it collects electrons, and the current is proportional to the electron density, which we can use for getting high time resolution information on the plasma density (Engelhardt et al., 2018b). However, if the spacecraft potential V_{SC} reaches negative values comparable in magnitude to the positive bias voltage, the probe potential with respect to the plasma will be close to zero, meaning that small relative variations in the spacecraft potential can have large impact on the probe current. As the spacecraft potential generally goes more negative in denser plasmas Odelstad et al. (2017), this means the probe current can actually decrease when the plasma density increases. This problem occurs only for a probe at positive bias voltage, and only when the spacecraft potential is more negative than about -10 V. If the spacecraft potential is very negative, it is therefore safer to use a probe at negative bias voltage when investigating plasma density variations. Such data are usually but not always available.

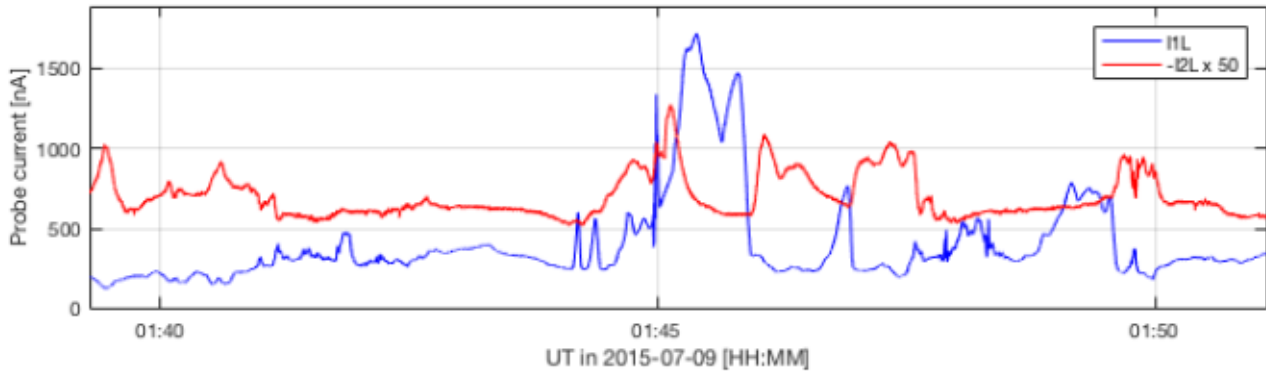


Figure 3.10: Example of spacecraft potential effects on a positively biased probe (LAP1, blue in the plot, at +30 V with respect to the spacecraft). The absolute values of the currents to both probes are shown, so that both should co-vary with the plasma density, though this actually is the case only for the negatively biased LAP2 (at -30 V). Covariation can be seen in some intervals, but at other times there is counter-variation or very little correlation. This may happen at high densities, where the actual potential of LAP1 with respect to the plasma is close to zero, making the current to it very sensitive to small changes in the spacecraft potential.

High LAP2 currents from May 2016

As noted in the discussion of the RPC example data in Section 3.3.2 above, LAP2 currents during the last months of the mission could sometimes be very high (μA range, much more than usual for the ion current from the plasma) and rapidly varying. Some aspects of these currents look artificial (the rapid jumps) while some look real (the correlation to density), and these data are not yet understood. Until better understood, these data should not be used.

3.4 The Mutual Impedance Probe (RPC-MIP)

3.4.1 Science use of the data

Basic data analysis are:

- mutual impedance spectra (L3 data):
 - use mutual impedance spectrograms (electric field spectrograms in active mode) to identify time variations of the plasma frequency, and therefore variations of the plasma density.
 - analysis of mutual impedance spectra to extract bulk plasma parameters, other than the total plasma density available in the PSA.
- plasma density (L5 data):
 - time series analysis of derived MIP plasma density based on irregularly sampled time series spectral analysis, e.g. non-uniform discrete Fourier transform (NDFT), Lomb-Scargle periodogram, etc.
 - spatial analysis of plasma density: vertical profiles, mapping.
 - data/simulation comparisons.
 - a combination of the RPC-MIP and RPC-LAP input is available at PSA as a different L5 dataset of plasma density measurements. This dataset is obtained by rescaling the

RPC-LAP ion current and floating potential measurements to the RPC-MIP density measurements, as described in the RPCMIP/RPCLAP cross-calibration report.

Some relevant publications showing examples of RPC-MIP data analysis, for both mutual impedance spectrograms (L3) and plasma density (L5):

Modelling of the RPC-MIP mutual impedance (active) spectra and extraction of plasma parameters

An example of model of a mutual impedance the RPC-MIP instrumental response in a two-electron temperature plasma is described and applied to RPC-MIP (Gilet, N. et al., 2017).

Derivation of plasma density time series from RPC-MIP active spectrograms for cometary science

Two examples of plasma density extraction from RPC-MIP active spectrograms in the context of cometary plasma increase associated with a cometary outburst (Grün et al., 2016; Hajra et al., 2017).

An example of derivation of plasma density time series from RPC-MIP active spectrograms in order to test and support an ionospheric model based on photo-ionisation only (Vigren et al., 2016).

An example of derivation of plasma density time series from RPC-MIP active spectrograms in order to test and support an ionospheric model based on photoionisation and ionisation by electron impact (Galand et al., 2016; Heritier et al., 2018).

Identification and characterisation of plasma boundaries

An example of analysis of unmagnetised (aka diamagnetic) regions is described in Henri et al. (2017).

Example of combined analysis of RPC-MIP and RPC-LAP measurements to extract densities, velocities, temperatures

An example of cometary ionospheric plasma density study, including a cross-calibration of RPC-LAP and RPC-MIP density measurements, the extraction of a cometary plasma density vertical profile, and comparisons with expected plasma densities from an ionospheric model is presented in Heritier et al. (2017)

An example of ion bulk velocity estimation combining RPC-MIP and RPC-LAP measurements is given in Vigren et al. (2017).

An example of electron temperature estimation combining RPC-MIP and RPC-LAP measurements is proposed in Odelstad et al. (2018).

3.4.2 Example of the dataset

The plasma density (L5) are obtained from the MIP active spectra (L3) under certain plasma conditions, that enable to identify the plasma frequency line on the MIP spectrograms. Users are

encouraged to check that the plasma frequency line is clearly visible on the MIP active electric spectrograms (L3). Time intervals when the plasma frequency line is not visible in the MIP active electric spectrograms are such that the MIP density (L5) is not retrieved. The users are therefore encouraged to start learning how to use the MIP data using the period May-September 2016, during which an almost complete coverage of plasma density is provided. During this interval, users are encouraged to start with time periods during which MIP is operated in burst mode and in LDL and/or in SDL phased mode.

Fig. 3.11 shows MIP data acquired in active SDL mode for July 30, 2016. Some instrument operational parameters are shown in the top panel as color bars, giving information on the transmission configuration. The first panel shows the colour-coded frequency-time spectrogram of active mutual impedance spectra between 0 dB and 30 dB. Note that an operating mode change occurred around 13:30, resulting in variation in the instrument frequency range. While the plasma frequency line is clearly observed on the spectrogram, it is contaminated by some interferences (appearing as high amplitude horizontal line(s)) and by a fluctuating signal-to-noise ratio along the day. To bypass these issues when analysing the plasma line, it can be useful to process RPC-MIP spectra by removing the strongest interference(s) and normalizing spectra individually to better highlight the resonance or the cut-off around the plasma frequency. This is illustrated in the third panel, where the plasma line is highlighted as the blue-to-red sharp transition. The fourth panel gives the phase of the mutual impedance spectra, normalized individually as in the previous panel. While the interpretation of RPC-MIP phase data is somehow intricate and requires some level of modelling, the information contained there is usually valuable to validate results obtained on the power spectra. As active measurements only are used to derive the plasma density, the passive MIP measurements are not shown here. They usually contain less information to extract the plasma density and cannot be interpreted without a dedicated processing step. The bottom panel gives the result from an automatic plasma line derivation from the power active spectra, converted to density and shown as grey diamonds, with a moving median density over-plotted as a red line.

Note that the plasma line is no longer visible in the MIP active spectrogram (Fig. 3.11, top panel) during 23:00-24:00. This is most probably due to the fact that the Debye length gets larger than the MIP transmitters-receivers distance because of the decreasing plasma density. Therefore the plasma density cannot be extracted from MIP measurements during this time interval (Fig. 3.11, bottom panel).

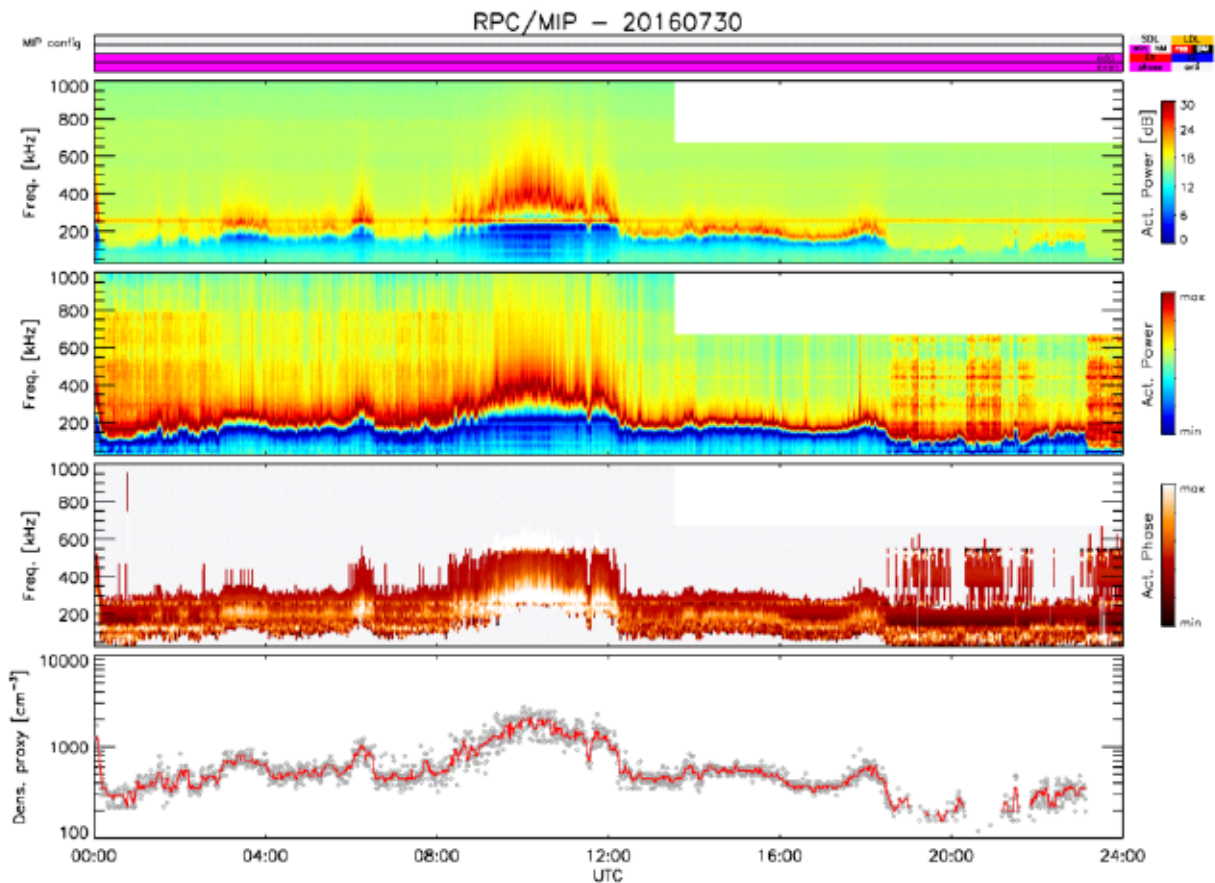


Figure 3.11: Example of RPC-MIP data overview during a full day in 30 July 2016, from top to bottom: (i) MIP operational parameters, (ii) calibrated active MIP power spectrogram (Level 3), (iii) rescaled calibrated active MIP power spectrogram (Level 3), (iv) rescaled calibrated active MIP phase spectrogram (Level 3), (v) retrieved MIP densities (grey dots) and moving averaged density (red line) (Level 5).

3.4.3 List of caveats

The plasma density (L5) are obtained from the MIP active spectra (L3) under certain plasma conditions, that enable to identify the plasma frequency line on the MIP spectrograms. The known caveats on the MIP L3 and L5 data are described in the RPC-MIP User Guide (see RPC-MIP User Guide, Section 9). The known caveats regarding the cross-calibrated density dataset are described in RPCMIP/RPCLAP cross-calibration report.

Note also that a quality value is associated with each density value given in the PSA archive (cf. RPC-MIP User Guide and RPCMIP/RPCLAP cross-calibration report). The user is strongly encouraged to consider using it.

3.5 The Magnetometer (RPC-MAG)

3.5.1 Science use of the data

The magnetometer delivers timeseries of the magnetic field vector data. All the scientific usable data (data in celestial coordinates like ECLIPJ2000 or CSEQ) contain the actual position of the

spacecraft and the measured 3-component magnetic field vector. Basic magnetic field analyses are:

- plotting of the timeseries,
- filtering using suitable filters (low pass, band pass, high pass),
- spectral analyses e.g., computation of power spectral density, dynamic spectra, cross spectral density using IB, OB and possible ROMAP Lander data,
- minimum variance analyses (in order to study wave properties),
- plotting hodographs (to investigate polarization phenomena),
- compare IB and OB signatures (to assess spacecraft disturbance and extract external field effects),
- comparing data with simulations,
- reconstructing spacecraft attitudes using magnetic field data measured on-board two different spacecraft under the assumption of equal signatures.

The following list shows examples of published papers using, analysing and interpreting RPC-MAG magnetic field data.

Comparison with measurements by the lander magnetometer

Auster et al. (2015)
 Heinisch et al. (2016)
 Heinisch et al. (2017)

Diamagnetic cavity investigations

Goetz et al. (2016b)
 Goetz et al. (2016a)

Magnetic field waves

Richter et al. (2015)
 Richter et al. (2016)
 Volwerk et al. (2016)
 Koenders et al. (2016a)

Structure of the field and plasma environment

Koenders et al. (2016b)
 Volwerk et al. (2017)
 Volwerk et al. (2018)

Overview of observations

Goetz et al. (2017)
 Glassmeier (2017)

3.5.2 Example of the dataset

For scientific use the data with the highest available time resolution should be used. Furthermore the magnetic field should initially be analyzed in a celestial coordinate system; therefore data are provided in ECLIPJ2000 system for the pre-comet phase and in the CSEQ-System (cometocentric solar equatorial coordinates) for the comet phase. This means that CALIBRATED Burst mode data (M3) of LEVEL_C (CLC) should be the first choice. Data are disturbed by reaction wheels, therefore a huge effort has been taken to eliminate this impact from the data. Thus for intervals where this correction was successful, resampled LEVEL_H (L4) data are provided and should be used preferentially. All these datafiles contain the spacecraft position as well. Thus full geometry information is available.

In order to improve the estimation of any offset e.g. coming from the spacecraft residual field, observations close to magnetic cavities are best, as the external field should per definition be identical to zero in the cavity (see Goetz et al. (2016b)).

On the other hand, phases characterized by huge external magnetic fields are valuable as well, as during these intervals the offset and spacecraft residual fields are playing a negligible role.

As an example of data, observations from July 30, 2016 are shown in Fig. 3.12. The MAG-instrument was in normal mode all the day. The observations taken are displayed in CSEQ-coordinates. Besides the three magnetic field components also the magnitude is plotted as well. At the bottom of the plot the coordinates of ROSETTA with respect to the comet are displayed in the CSEQ frame accordingly.

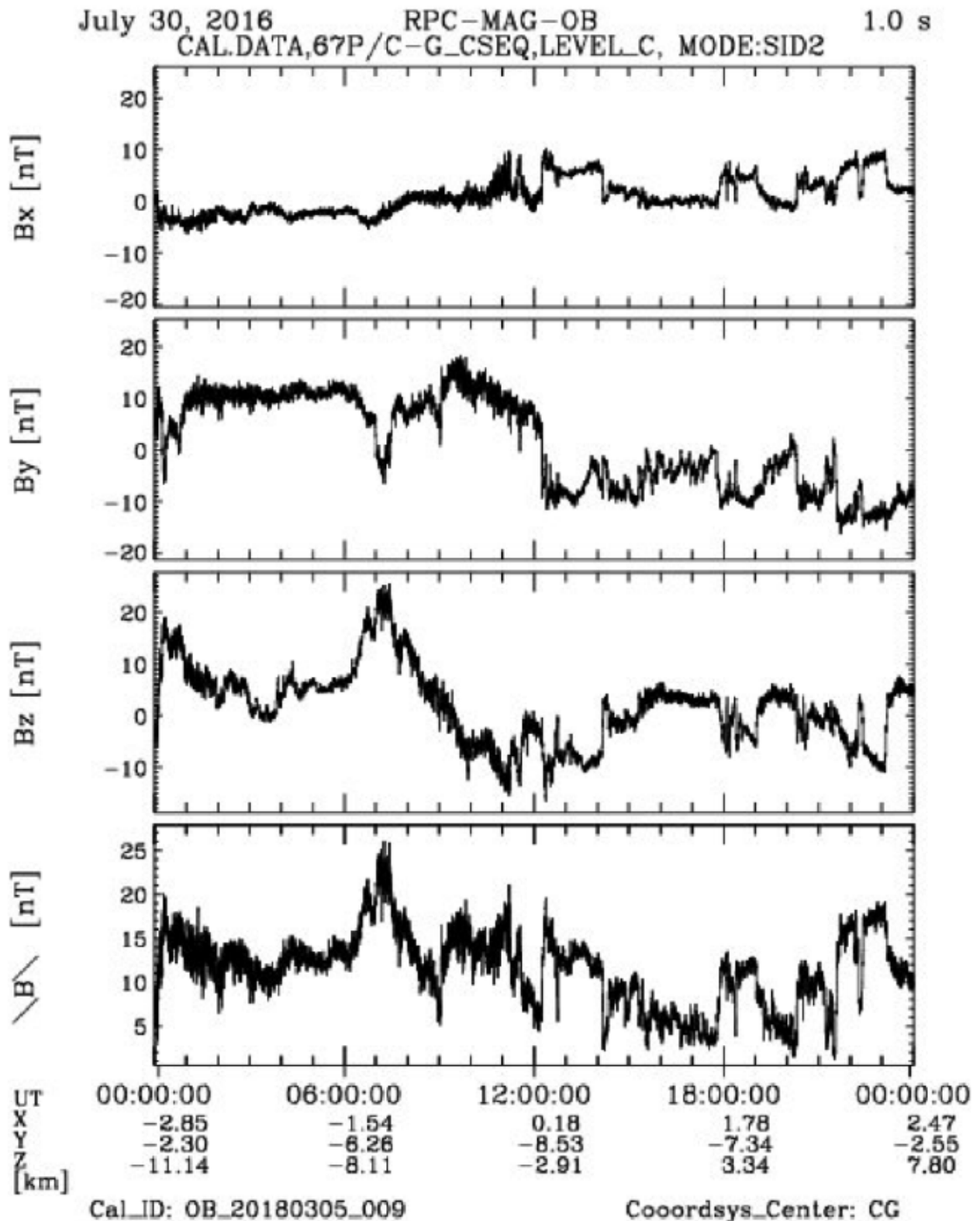


Figure 3.12: Overview of the three magnetic field components and magnetic field magnitude on July 30th, 2016. The data is shown in the CSEQ reference frame with highest available resolution (Level C, L3) data resampled to 1 Hz. Auxiliary data is given at the bottom.

3.5.3 List of caveats

The magnetic field sensors are very sensitive to various disturbance sources located on the spacecraft. Main disturbers are :

- Thrusters (movable magnetic valves), critical during phases of Wheel off-Loading (WOL) and Orbit Correction Manoeuvres (OCM)
- Currents (e.g. Lander power ESS, Heaters)
- Reaction wheels (rotating magnets, signatures appear aliased in the magnetic field data)

Furthermore, spacecraft attitude changes can cause non equilibrium temperature changes on both magnetic field sensors shifting the sensor offsets. In general this is considered in an advanced sensor temperature model but remaining offset residual can occur.

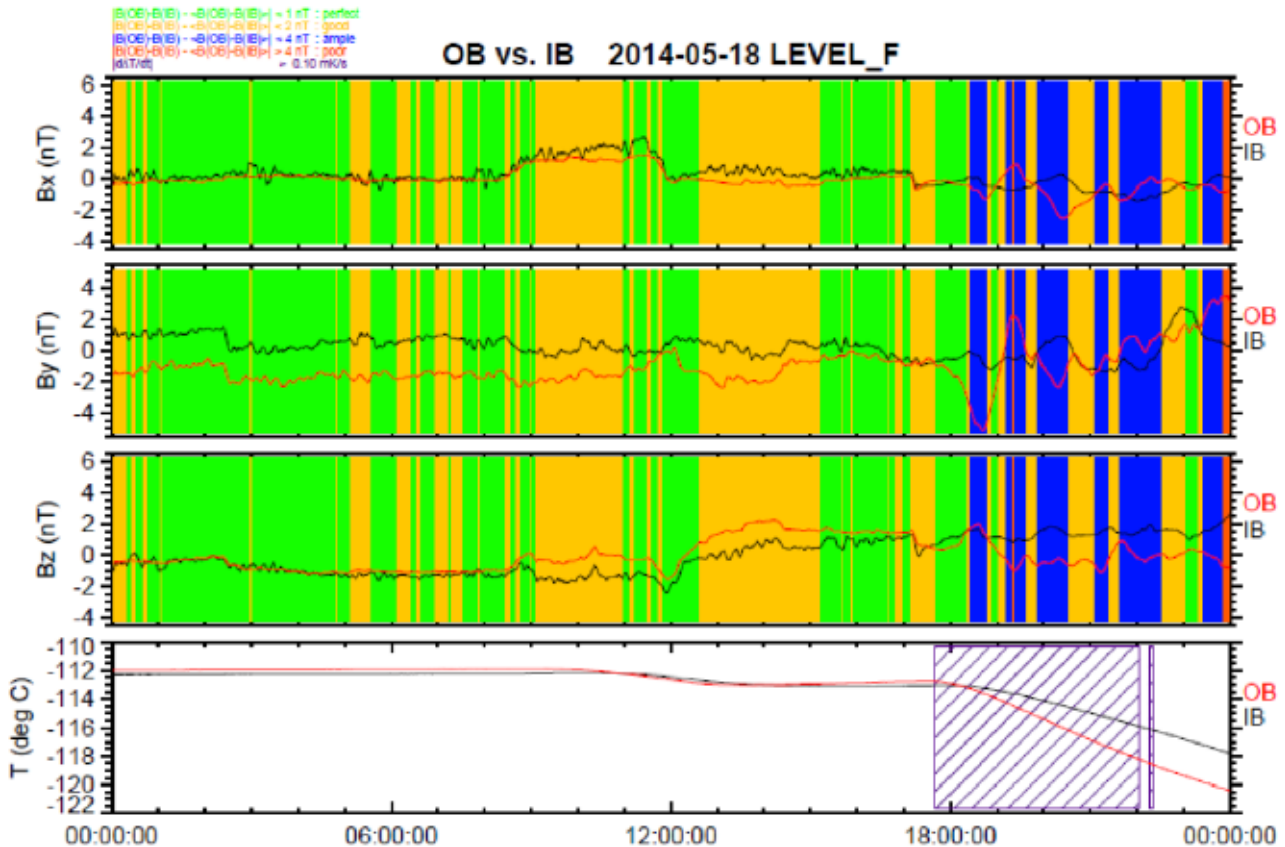


Figure 3.13: Example of averaged OB (red) and IB (black) data for a whole day (Level F, L4). All 3 components of both sensors and also the sensor temperatures are shown here. The coloured areas (see legend on the top) indicate the data quality with respect to the differences of the components and the temperature difference change rates.

Figure 3.13 shows examples of disturbed data by different sources on OB and IB data for a whole day. In times where the sensor temperature is stable, the magnetic field data of both sensor show similar behaviour as expected (IB is always more influenced by spacecraft disturbance and noise due to a closer location to the spacecraft body). Attitude changes can cause different temperature changes and therefore different magnetic field readings due to limited hardware temperature correction possibilities and a limited temperature calibration model. The colour coding reflects the quality of the data. For instance, green means that the difference between the OB and IB data and the mean difference of OB and IB over the whole day are less than 1 nT which means an excellent quality. For orange flagged data, however, the difference is more than 4 nT due to spacecraft effects or temperature drifts. Note that the new calibration model (V9.0) of 2018 generates much better data than the older models used temporarily during the mission.

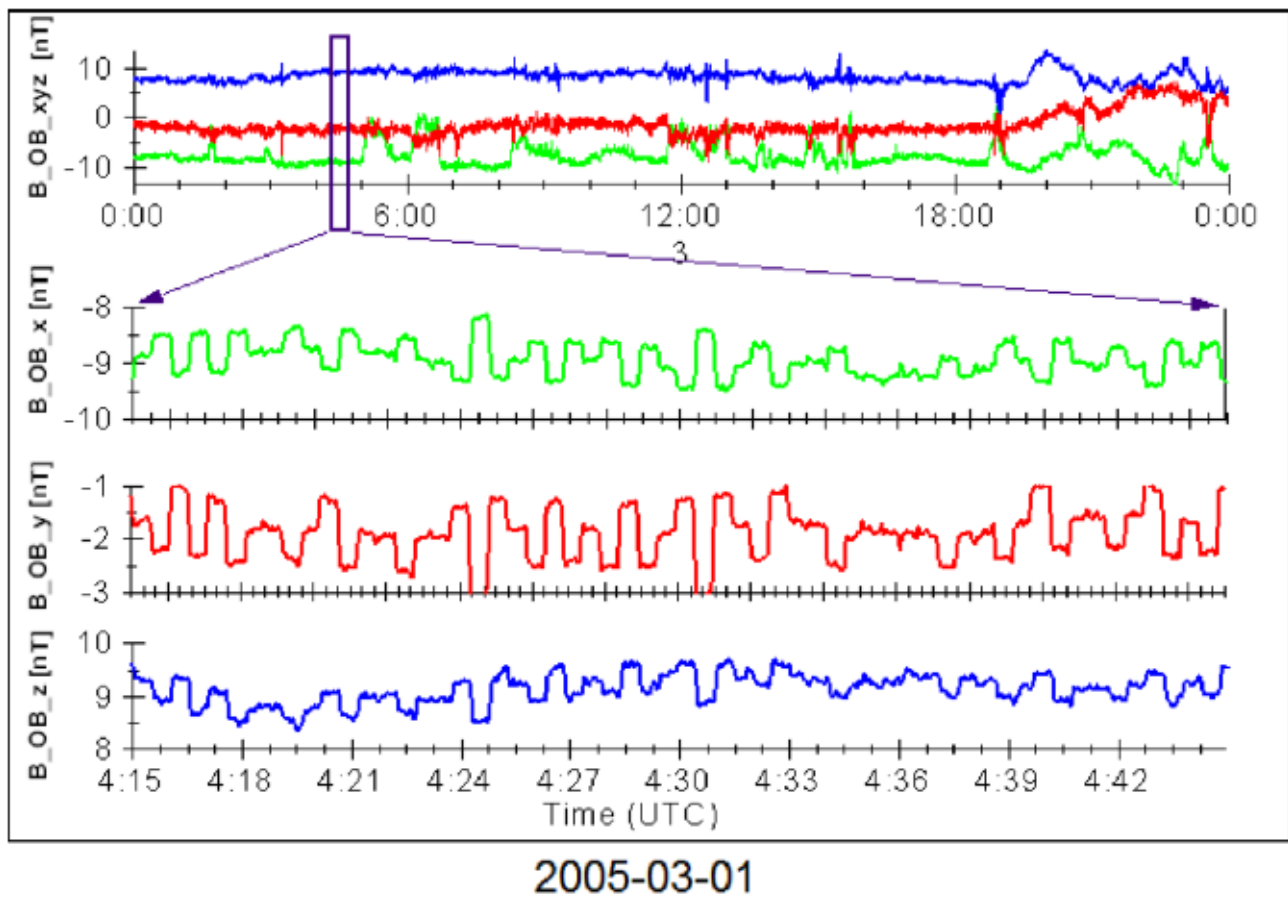


Figure 3.14: Influence of PHILAE heater currents. During the first Earth Fly by heaters on the Lander were activated with 1 min period. The heater current are causing magnetic field disturbances in the order of 1 nT. These disturbances have been accordingly flagged in the dataset. Unfortunately, they cannot be removed.

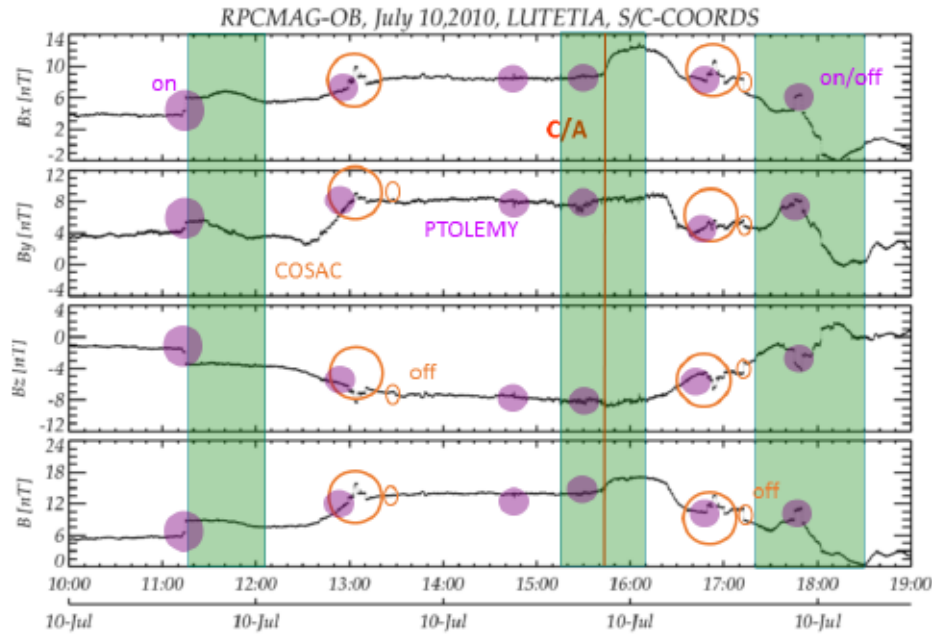


Figure 3.15: Influence of supply currents drawn by the PTOLEMY and COSAC experiments. The figure shows specific disturbance patterns in the order of 2 nT caused by the operation of the mentioned instruments. These disturbances have been accordingly flagged in the dataset. Unfortunately, they cannot be removed.

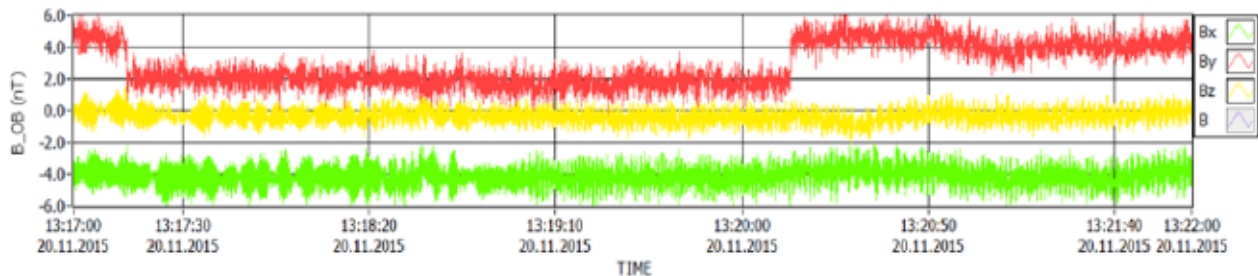


Figure 3.16: Disturbance by thruster activation during WoLs on LEVEL_C (L3) magnetic data. A clear shift of the spacecraft residual field in the order of ~ 3 nT can be seen while the latch valves of the thrusters are activated. The WoL activation is deterministic and known, thus these periods can be flagged as bad data.

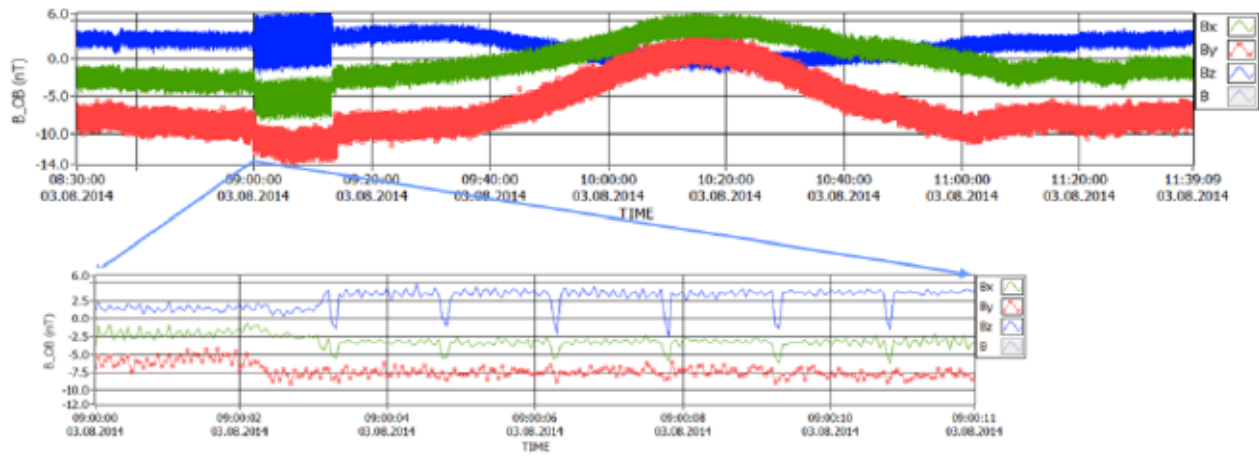


Figure 3.17: Disturbance by thruster activation during OCMs. Besides DC-jumps of ~ 2 nT additional AC spikes of ~ 6 nT spikes, at ~ 625 mHz, and ~ 200 ms width appear. An automatic cleaning of these structures is hardly possible, but the data in these intervals will be flagged as bad data in the final datasets.

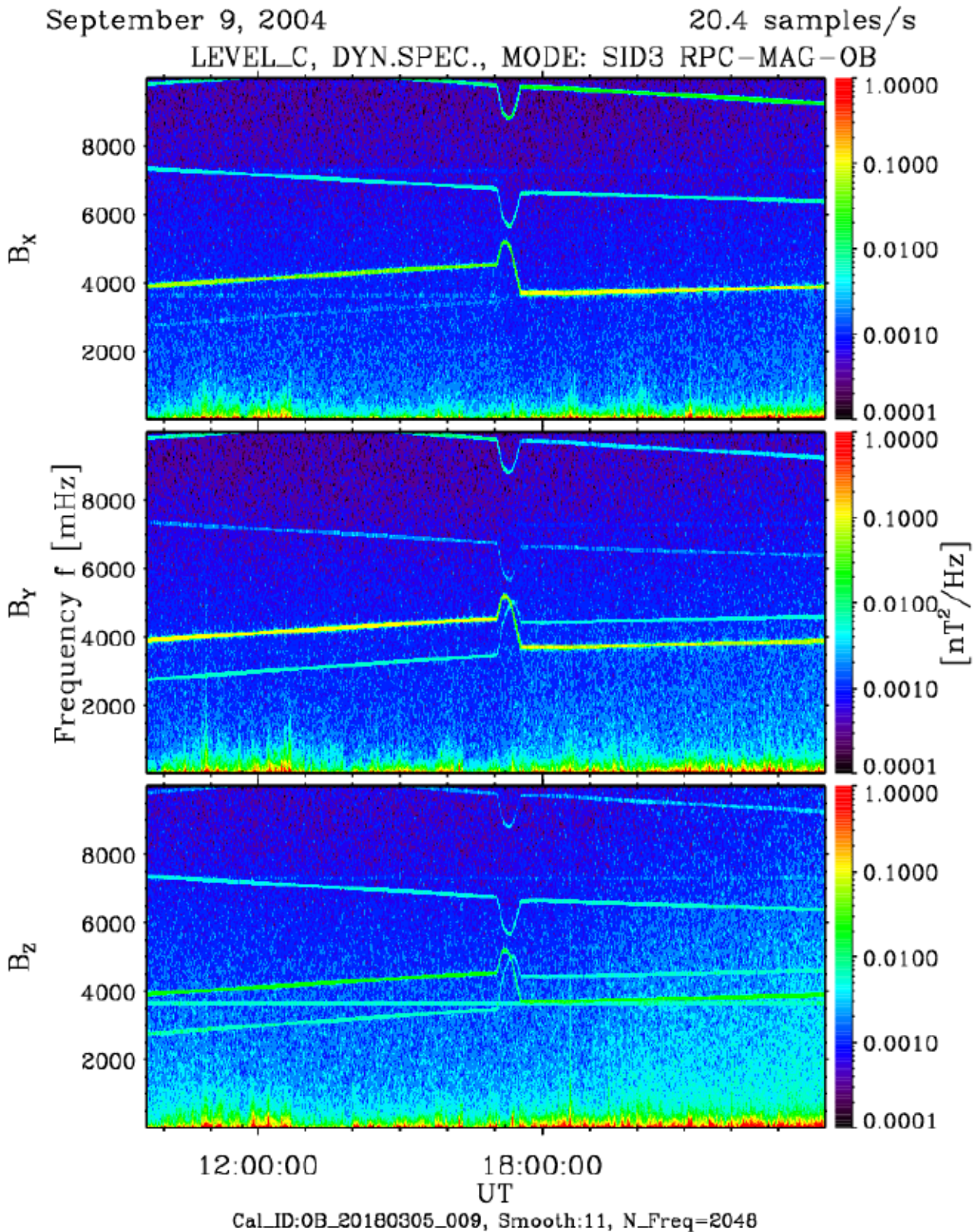


Figure 3.18: Dynamic power density spectrum of the magnetic field is shown for 16 hours of data. The tilted traces in the spectra represent the impact of the 4 spacecraft reaction wheels rotating at variable frequencies. They are causing dynamic disturbances in the 1-10 Hz range at amplitudes of ~ 2 nT. As these frequencies are known at any time, an automatic elimination is possible. Data without reaction wheel impact are delivered for the OB sensor in burst mode as resampled LEVEL_H (L4) data.

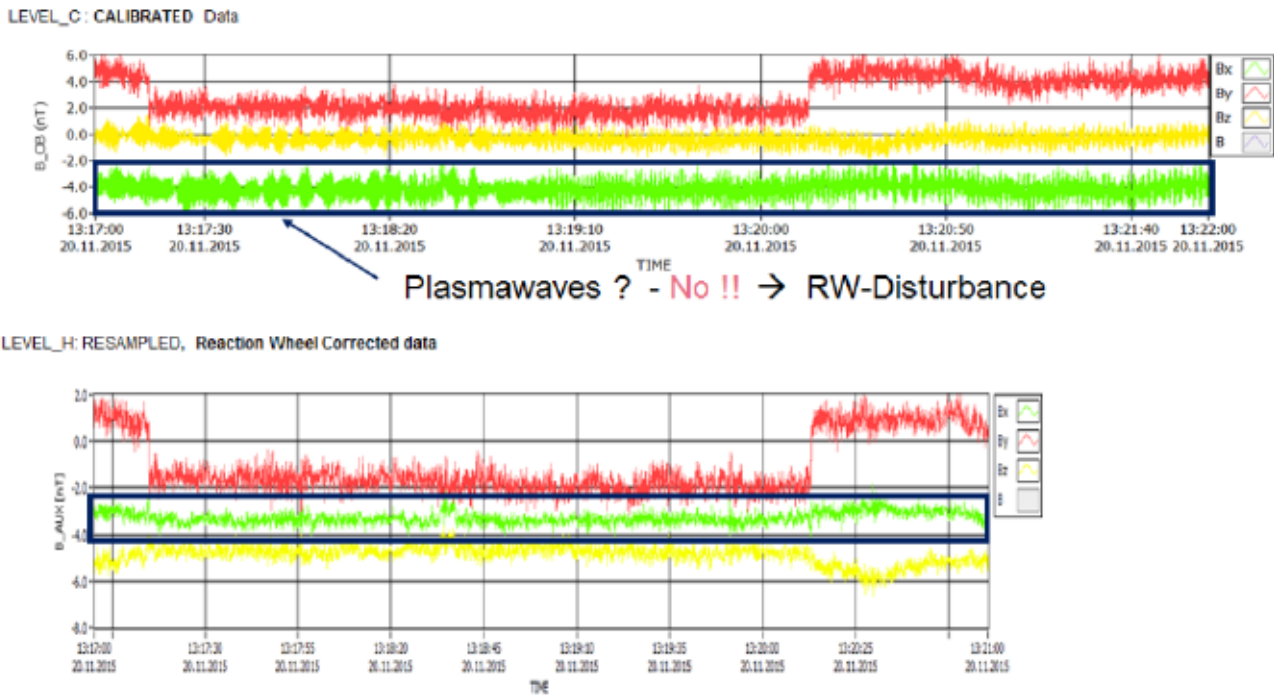


Figure 3.19: Impact of the reaction wheels in the time series. On the upper panel a nice plasma wave structure might be hypothesized (same as Fig 3.16, L3 data). However, a view to the reaction wheel impact eliminated LEVEL_H (L4) data in the lower panel clearly depicts, that there are no plasma waves present but only higher frequent disturbances (data shifted due to enhanced visibility).

All the examples above show that there is a lot of spacecraft influence diminishing the quality of the magnetic field data. As is it in many cases not possible to eliminate these effects automatically the data will only be flagged by certain designators. Each magnetic field vector in the calibrated data files is flagged with a string of digits. The meaning of these digits is explained in the related label files *.LBL, and the EAICD. In general, the lower the value of such a digit (0..9) is, the better the quality is. Furthermore, an “x” means that there is no quality assessment of that specific property. Thus, a user of the data - YOU! - has to be aware of the specific quality of the present data before doing any serious science analyses using these data!

Special care must be exercised calculating the field magnitude or derived angles. For the magnitude:

$$|B| = \sqrt{\sum_i (B_i + \text{offset}_i)^2}$$

the root of the sum of squared offset and spacecraft residual afflicted magnetic field components has to be calculated. With uncertain spacecraft residual field- and offset-components, the magnitude becomes uncertain in a non-linear way, possibly depicting a strange trend. This is not only a simple additive shift but a variable displacement, possibly leading to misinterpretation.

Similarly, for angles of the magnetic field

$$\alpha = \arctan \left(\frac{B_i + \text{offset}_i}{B_j + \text{offset}_j} \right)$$

the same care has to be exercised. The division of entities of the same order which are afflicted by errors can produce very uncertain results, especially if the error are in the order of the

actual field components. Thus be careful when calculating and interpreting angles!

An additional point which should be mentioned here is the filtering of the data. Burst mode OB data are sampled with 20 Hz and pass all the processing chain unchanged from the instrument via telemetry to the calibration pipeline. The normal mode data, however, show an effective vector rate of 1Hz, which is accomplished by digital filtering inside PIU, using a two stage FIR decimator with -3 dB cutoff at 0.3 Hz and final damping of about -130 dB starting at ~ 1.8 Hz. This very steep filter characteristic was also used for the generation of 1s averaged data for the RESAMPLED datasets, in order to keep the spectral characteristics of the normal mode data also for the averaged burst mode data. Otherwise the noise properties would have changed within one datafile at the transitions from one mode to another. Therefore, RESAMPLED data are good for quicklook purposes, but should not be used for wave investigations as the amplitudes in the 0.1 - 0.5 Hz range are damped much more as if have been filtered by a standard - even higher order - 1Hz Butterworth low-pass. Thus, for spectral analyses, the original burst mode data should be used if available.

3.6 The Plasma Interface Unit (RPC-PIU): Illumination maps

3.6.1 Science use of the data

The illumination maps and ASCII illumination files provide a context for the outgassing activity and its variability and to support the analysis and scientific interpretations of neutral and plasma observations. They have been used as supporting material in the following papers: Galand et al. (2016), Heritier et al. (2017) and Hoang et al. (2017). The illuminated area and the percentage of the illuminated surface – both provided in the labels of the ASCII files – are also relevant to provide constrains on the outgassing rate, especially when the ROSINA/COPS total number density is not available.

3.6.2 Example of the dataset

For each set of subsolar colatitude and longitude, we have created one ASCII file in order to offer the possibility to the users to generate their own 3D representation of the comet with the right illumination (see Fig. 3.20 and 3.21).

Here is an example of values of the cosine of the angle between the normal of the facet and the Sun direction, taking into account self-shadowing effects. It is found in the ASCII_000_038.TAB file corresponding to the subsolar longitude of 0° and subsolar colatitude of 38° :

```
...
0.0
0.0
0.19671
0.08952
0.08632
0.37012
...
```

0.0 means that either the facet is in the shadow (each node of the facet is hidden by a part of the comet) or the cosine is lower than 10^{-5} . The latter occurs almost in the terminator plane



Figure 3.20: 3D representation of the comet with the corresponding illumination and orientation with respect to Rosetta on 17 October 2014 at 11:46 (top), 15:30 (middle) and 18 October 2014 at 23:00 (bottom). The white lines correspond to 6 meridians: $\pm 0^\circ$, $\pm 60^\circ$, $\pm 120^\circ$. The blue lines represent the circles of latitude: -30° , the equator and 30° . From Galand et al. (2016).

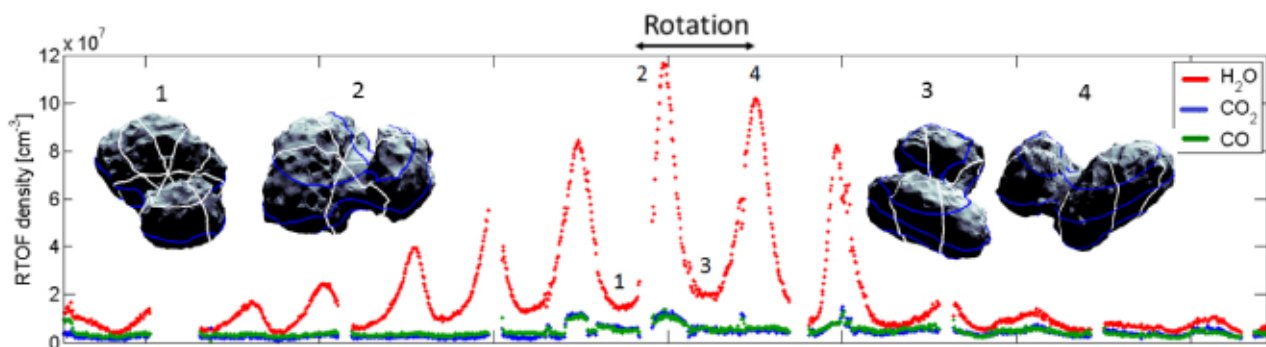


Figure 3.21: 3D representation of the comet with the corresponding illumination and orientation with respect to Rosetta from 8 October to 11 October 2014. The white lines correspond to 6 meridians: $\pm 0^\circ$, $\pm 60^\circ$, $\pm 120^\circ$. The blue lines represent the circles of latitude: -30° , the equator and 30° . In addition, H_2O , CO_2 and CO number densities are displayed for the same period. The number density increased every time Rosetta was seeing the illuminated neck. From Hoang et al. (2017).

(grazing incidence).

Software, such as MATLAB (see Section 4.4), allows to assign a particular colour to a 3D object. Here the colours associated with each facet is the value provided by the ASCII file.

In addition, illumination maps can also be projected in 2D (longitude vs latitude available on the PSA, called MAP_XXX_YYY.FIT), or ASCII files can be stacked together for one or several rotation periods for an average illumination (see Hoang et al. (2017)).

Additional informations are provided in the .LBL.

ROSETTA KEYWORDS	UNIT	DESCRIPTION
ILLUMINATED_SURFACE_AREA	km ²	Illuminated surface area of the comet; the facet area is included if at least one of its nodes is illuminated.
ILLUMINATED_SURFACE_PERCENTAGE	%	Ratio between the non-weighted illuminated surface area and the total surface area of the comet.
ILLUMINATED_SURFACE_AREA_WEIGHTED	km ²	Illuminated surface area of the comet weighted by the cosine of the solar zenith angle (0 if in the shadow).

3.6.3 List of caveats

The caveats concern the eventual errors made for the illumination. From the 3D shape model, the code for determining the illumination (cosine of the solar phase angle) of each facet tests whether or not each node is shadowed by another facet. However, each facet has 3 nodes, all, some or none of them may be shadowed. A decision should be taken when only 1 or 2 are shadowed, i.e., when the facet is partially shadowed. It especially happens at the terminator plane. It has been decided to set the cosine to 0, either when all the three vertices of the facet are shadowed, or when the cosine is less than 10^{-5} . This assumption leads to uncertainties on the total illuminated area and thus depends on the resolution of the shape model.

Concerning the 2D maps, the facets are projected following a “plate carrée” projection: the facets are no longer triangular, their edges are no longer a perfect line. Surfaces and distances are modified.

Finally, the 2D maps should not be used to averaging the illumination over a period unlike ASCII files. Because of the degeneracy (i.e., some parts of the comet are sharing the same longitude and latitude) and as we have chosen to put in the foreground the most illuminated surfaces, the 2D maps cannot be stacked together and then accurately provide an average illumination.

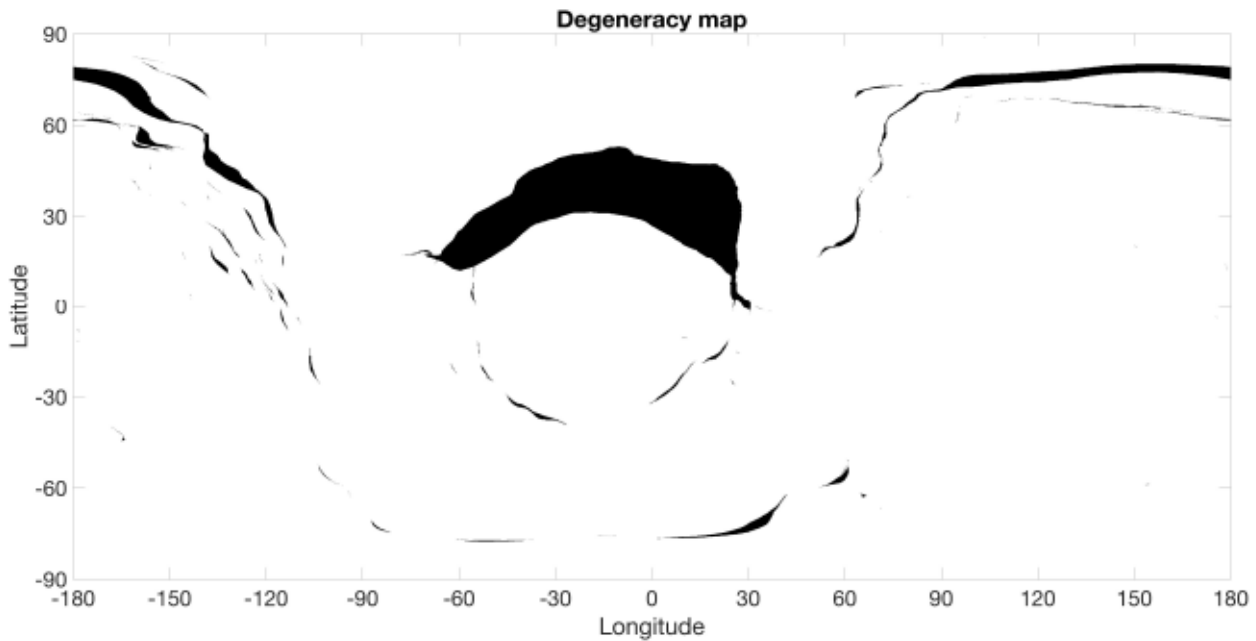


Figure 3.22: Degeneracy map in longitude and latitude of the surface of 67P. Black regions correspond to places where several facets share the same latitude and longitude at these locations.

3.7 Rosetta Orbiter Spectrometer for Ion and Neutral Analysis (ROSINA)-Comet Pressure Sensor (COPS)

Even if it is not part of the RPC consortium, the data from ROSINA/COPS is extremely valuable for the analysis of the RPC dataset. COPS has the capability of providing the neutral number density of the coma at the location of Rosetta, and a proxy for the outgassing rate. Like other sensors, ROSINA has its dedicated User Guide which describes the instrument, including COPS. In particular, we would like to highlight potential caveats or variations from COPS which can be misinterpreted. COPS can be affected by the ambient plasma conditions at Rosetta or by dust. Many examples are shown in the Ph.D. Thesis of Tzou (2017). Fig. 3.23 is an example of COPS measurements with and without plasma within the chamber. P.S.: COPS has a replica of the one onboard Rosetta with which these measurements have been done.

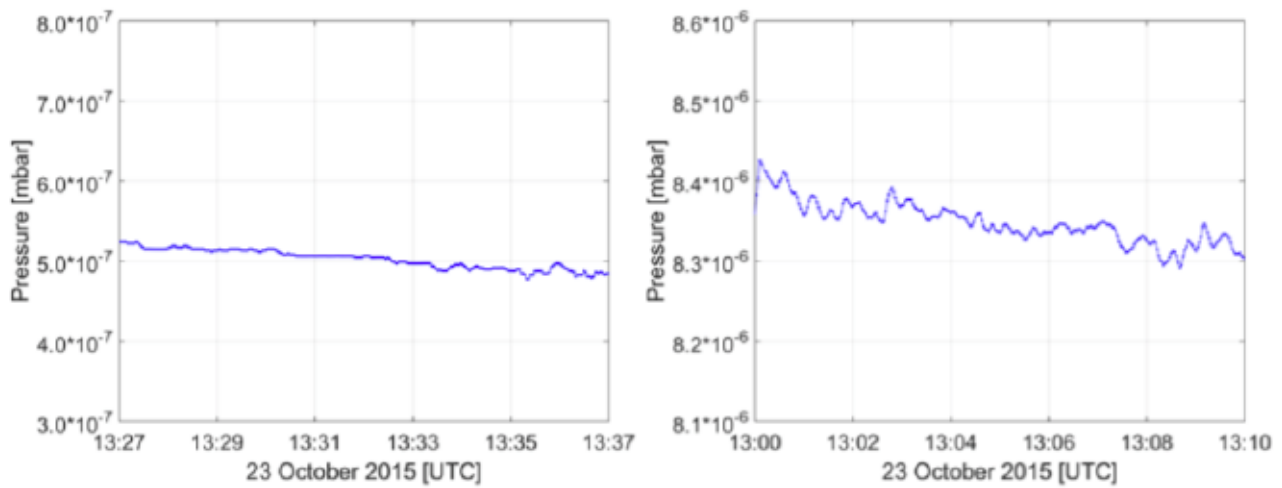


Figure 3.23: From Tzou (2017). Example of measurements by COPS with (left) and without (right) plasma in the chamber. Plasma inside the chamber makes COPS measurements less reliable: the pressure measured is higher, spikier and variable on short timescales.

Chapter 4

Recommended software for visualisation/analysis of the RPC science data

4.1 Data Formats

The data for the Rosetta mission are archived in NASA PDS3 format. This is not always ideal for plasma data, particularly higher dimensional particle data. Also, the metadata is in a separate .LBL file and without standardisation of the nomenclature for some scientifically useful metadata.

To mitigate this, it is now possible to download some of the RPC datasets (see detailed list below) on the PSA in NASA Common Data Format (CDF), ISTP¹ compliant. This format is understood by many tools currently used by the space physics community (such as QSAS, Autoplot, SPEDAS and easily loadable in IDL, Matlab and Python).

The CDF files are binary, and must be read using the CDF libraries integrated into analysis tools. However, please note that it is recommended to use the NASA routines to read CDF/ISTP files in Matlab and IDL to make sure that EPOCH16 variables are loaded properly (available at <https://spdf.sci.gsfc.nasa.gov/pub/software/cdf/dist/>). CDF format handles multi-dimensional data naturally, and the metadata is available within the CDF file itself. This allows the reading software to make intelligent decisions on how to handle the data, such as units, coordinate frame, whether the quantity is a scalar or vector and dimensionality. It also allows the dimensions to be described (energy bin ranges, angular ranges, etc).

This conversion requires specific knowledge of the product being converted, and special handling for some products. As a consequence it will only be made available for L3 products and above (see detailed list below).

The CDF files have been created by the ESA SPARTA software and stored on the PSA as daily files. SPARTA converts the ingested data (in this case PDS3) into an internal format and writes it out in the selected output format (in this case CDF). Available metadata is included in the CDF file in the ISTP compliant CDF standard.

It is highly recommended that, when available, the RPC data be downloaded in CDF format for use with any pre-existing tools or software libraries. The PDS3 format is useful for visual inspec-

¹International Solar-Terrestrial Physics

tion (ASCII .TAB files) or processing in the user's own software for scalar and 1-dimensional (e.g. vector) data products. See the sections 4.2 on AMDA and 4.3 QSAS for what can be achieved by software that is ISTP metadata aware.

As of 10 December 2018, daily CDF files derived from the following RPC datasets are available on the PSA in CDF ISTP compliant format for the whole Rosetta mission:

RPC-IES: Level 3 related to differential energy flux for electrons and ions, Level 5 (when available) related to moments

RPC-MAG: Level 4 V3.0 or V6.0 (when available) of type B,C,F,G,H

Daily CDF files converted by SPARTA from RPC-LAP, RPC-MIP and RPC-ICA best calibrated PDS3 datasets will be made available on the PSA soon after their final delivery.

Downloading from the PSA UI

STEP 1: Open PSA in a browser at <https://archives.esac.esa.int/psa>

The screenshot shows the PSA web interface with the following details:

- Header: EUROPEAN SPACE AGENCY, SCIENCE & TECHNOLOGY, COSMOS, ESA logo.
- Page Title: planetary science archive, PSA 2.5.0
- Navigation: Expand All, Collapse All, Show Browse Images Only.
- Search: Filter by string in the current page.
- Table Columns: Product ID, Observation Start Time, Observation Stop Time, Target, Mission, Instrument, Processing Level.
- Table Content: A list of RPC datasets with various product identifiers and observation times.
- Filters: Mission (Rosetta), Instrument (RPC), Processing Level (Level 3, Level 4, Level 5).
- Footer: Page 1, 3, 5000 items, Displaying 1 - 5000 of 13045.

STEP 2: Type RPC and click on search

STEP 3: In the table view, side left panel, click on "PROCESSING LEVEL" and select only levels 3 and up

STEP 4: Select your products according to the available CDF products listed above

STEP 5: Click the download button located on the top right corner of the table view



STEP 6: Please select: Send to Download Manager. The number of products will then appear in blue on the Download view logo (fourth logo from the top left of the table view).



STEP 7: Click on the Download view logo

STEP 8: In the download view select the CDF data format in the download options and click on Download products. The type of compression is then asked and data download starts.

The screenshot displays the 'planetary science archive' interface. At the top, there are navigation links for 'EUROPEAN SPACE AGENCY', 'SCIENCE & TECHNOLOGY', and 'COSMOS', along with a 'SIGN IN' link. The main header includes the 'esa' logo and a 'DOWNLOAD VIEW' label. Below the header, there is a navigation bar with several icons, including a download icon with a blue notification bubble.

The main content area is divided into two sections:

- PRODUCTS SELECTED FOR DOWNLOAD [3]**: This section shows a table with the following data:

Postcard	Product Identifier	Mission	Version	
N/A	RPCIES01627N_L3FLC_FLUX_V1	Rosetta	1.0	
N/A	RPCIES201627N_L3TDW_FLUX_V1	Rosetta	1.0	
N/A	RPCMAG160930T0000_FLX_00_M3	Rosetta	0.0	

 Below the table, there is a 'Remove all' button.
- DOWNLOAD OPTIONS**: This sidebar contains a 'Select the data format' dropdown menu set to 'Original Format'. Below it, the 'Original Format' is highlighted in blue. There are three radio button options: 'Product documentation', 'Mission documentation', and 'Only images'. At the bottom of this section is a 'Download products' button.

At the bottom of the page, there is a copyright notice: 'COPYRIGHT 2004 - 2019 © EUROPEAN SPACE AGENCY. ALL RIGHTS RESERVED.'

4.2 AMDA

AMDA is a powerful online data visualisation and access tool. Note that AMDA has been used during Rosetta operations as the RPC data temporary quicklook system. It permits multi-mission, multi-sensor visualization within the same browser window, and data selection based on these plots. It permits the user to see products from different instruments plotted on the same time axes. It can be used with pre-defined as well as user defined (and saved) plots designs. Data held on AMDA is publicly available for download or on special PI agreement. The date of the

latest dataset update is shown in the LastUpdate item of the DatasetHelp (click on small info icon near corresponding dataset node in the AMDA Parameters Tree to open DatasetHelp). If available, the version of dataset is shown (see Fig. 4.1).

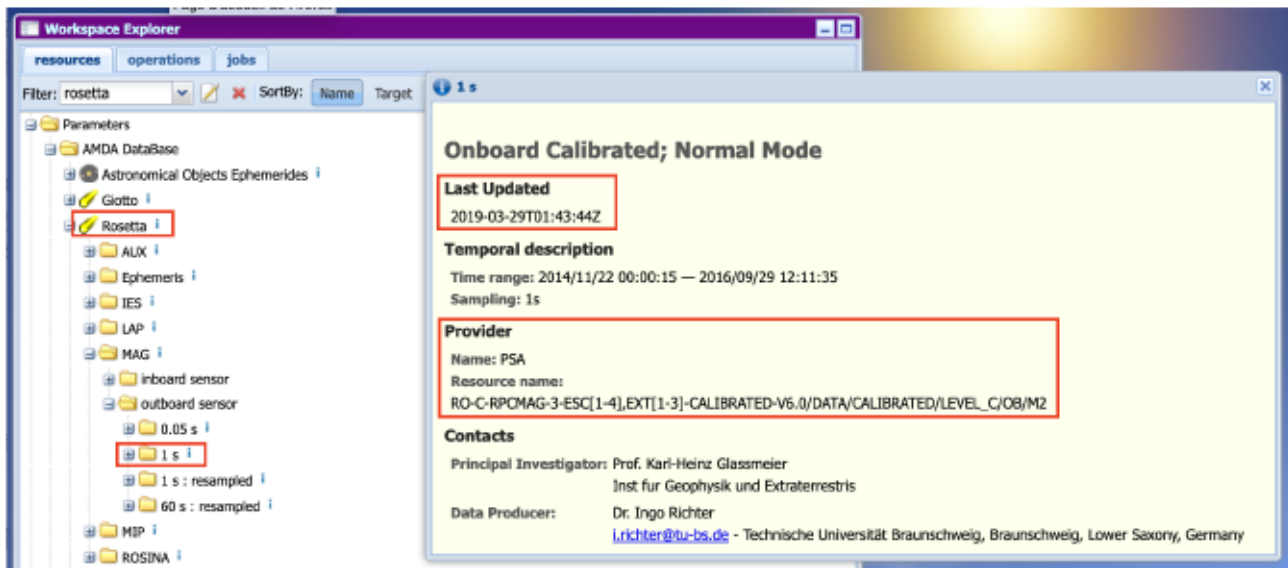


Figure 4.1: Screenshot of the interface once the user logs to AMDA. This is an example for Rosetta and RPC/MAG dataset. The file tree with the missions and their respective dataset is displayed on the left. An additional window pops up once the user clicks on the info icon of one dataset (next to 1 s here). The last update, the version and the provider are highlighted in the red boxes.

The AMDA system is accessed at <http://amda.cdpp.eu/>. New users are invited to select the “First visit - demo tour” button. Dataset from RPC-ICA, RPC-IES, RPC-LAP, RPC-MIP and RPC-MAG along with ROSINA/COPS (neutral density and pressure, which is often of relevance to RPC science), extracted from the PSA, are available on AMDA.

In order to plot a dataset, in the “Workspace Explorer” window, go to:

Resources → Parameters → AMDA Database → Rosetta

There, you can choose amongst the various ephemeris, RPC and ROSINA parameters which are available. Next, click on the “Plot data” icon available on the bottom part of the AMDA desktop to open the “Plot Manager” window and drag the relevant parameters to plot from the “Workspace Explorer” window to the “Plot Manager” window.

One example of how to practically use AMDA and quickly plot RPC data is given in Figure 4.2, using only a subpart of the Rosetta data available on AMDA, for the time interval 8:00-14:00 UTC on 2016/02/19. Clicking “Plot” lets pop-up a plot panel shown in Figure 4.3. In this example, the data show the impact of a cometary outburst observed on the 19th of February 2016 (seen in neutral density increase from 10:00 in the top panel), on the cometary inner ionosphere (with cometary plasma density increase, energetic electron decrease and magnetic field local pile up and rotation) documented in Hajra et al. (2017).

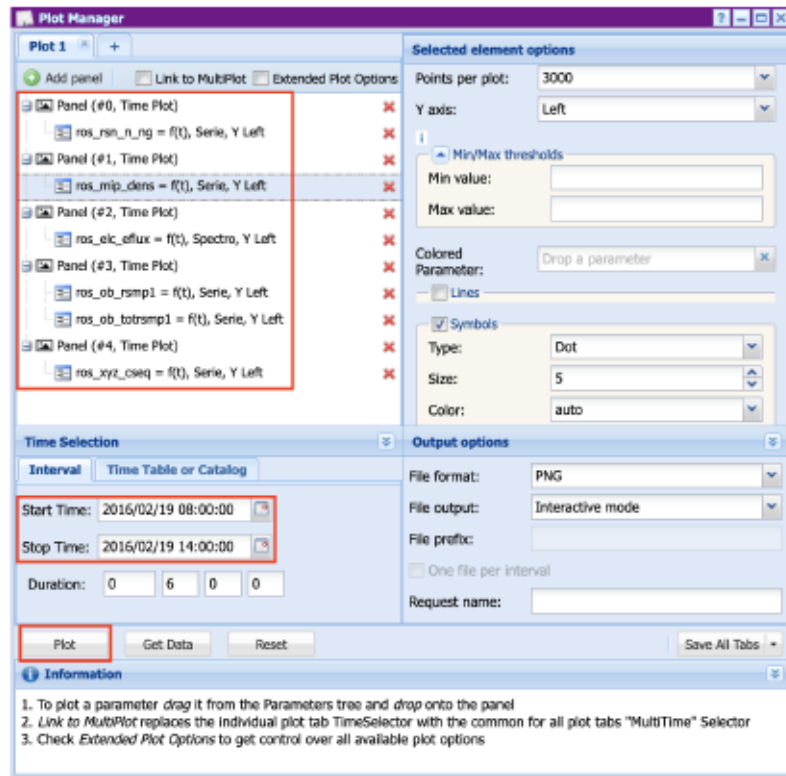


Figure 4.2: Example of AMDA plotting interface, to generate Figure 4.3.

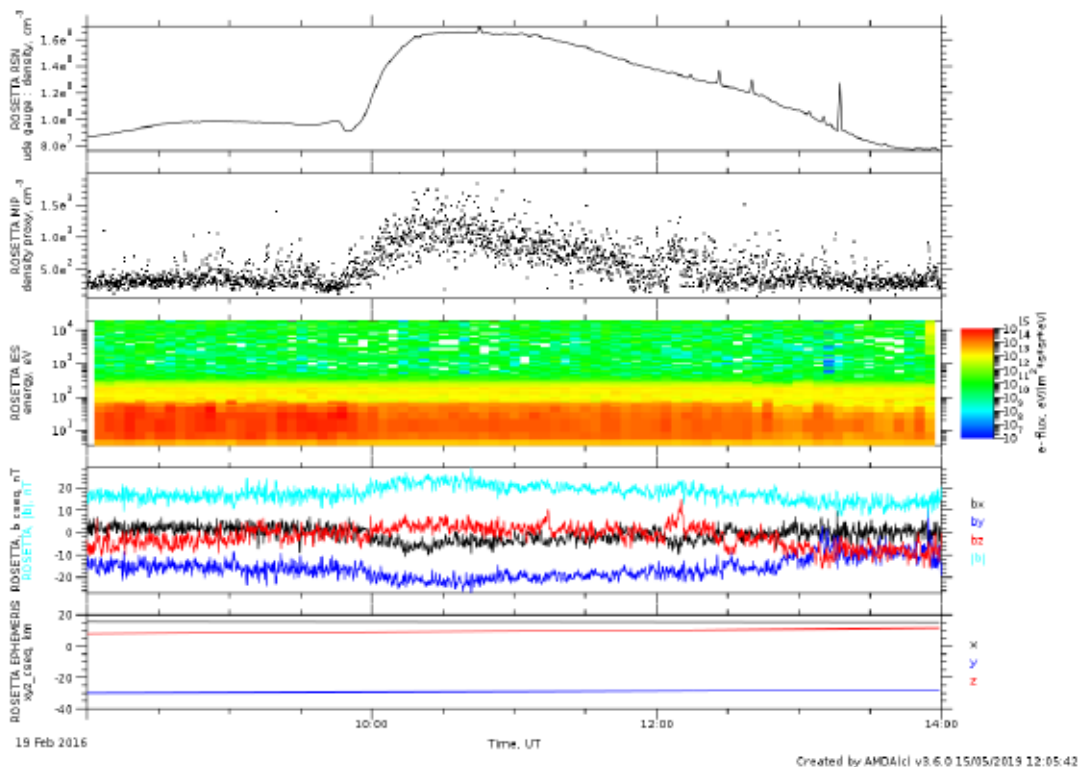


Figure 4.3: Dataset version produce by setup in Figure 4.2: Quicklook based on a cometary outburst (Hajra et al., 2017). From top to bottom: Neutral density (from ROSINA/COPS), plasma density (from RPC-MIP), energetic electron count rates as a function of energy (from RPC-IES), the three components of the magnetic field vector together with its amplitude (from RPC-MAG), location of Rosetta in the CSEQ frame.

Note that data downloaded from AMDA does not currently come with minimal set of metadata attached, and it is recommended for data interval selection, but the PSA should be used as primary source of RPC data. AMDA expects to ultimately provide visualisation of all RPC data held at the PSA.

4.3 QSAS

QSAS is a software tool run on the user's own computer. It may be downloaded (available for Mac, Windows and Linux) from <https://sourceforge.net/projects/qsas> and the QSAS homepage is at http://www.sp.ph.ic.ac.uk/csc-web/QSAS/qsas_welcome.html.

QSAS can read, manipulate and plot multi-instrument and multi-spacecraft time series data.

Data is held in a 'Working List' of data objects, and operations are assembled via simple drag and drop between windows. Figure 4.4 show the QSAS main window (Working List) and plot interface.

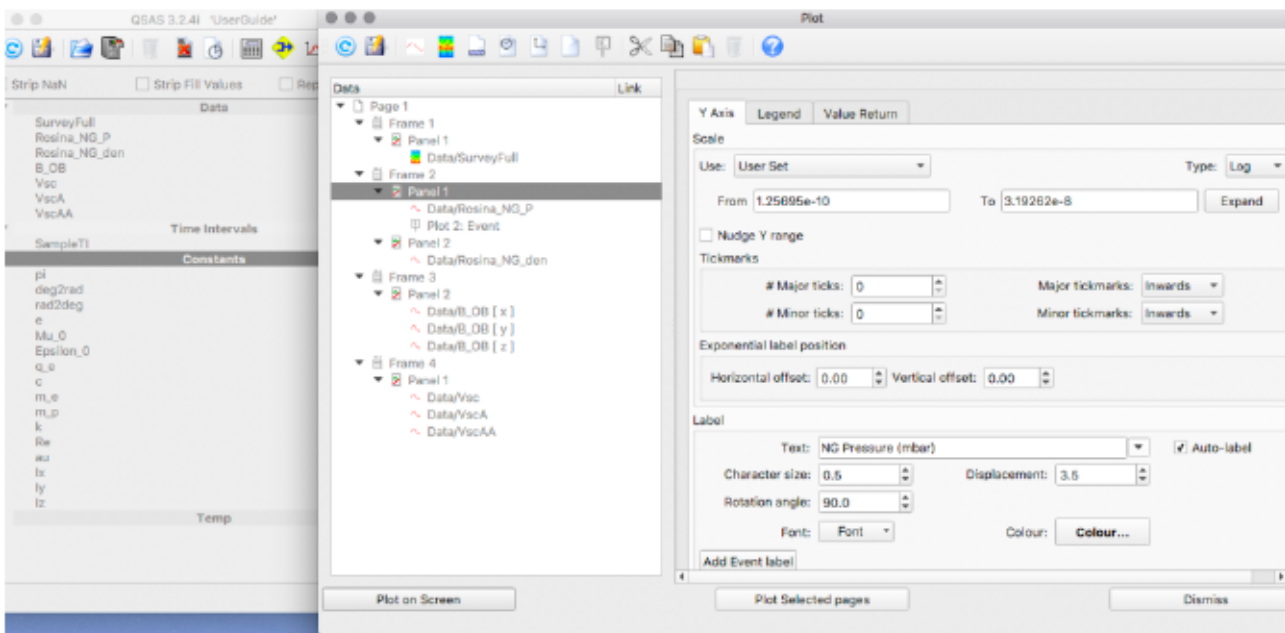


Figure 4.4: Dataset version: Quicklook based on preliminary analysis (pre-PSA release).

The resulting plot (Fig. 4.5) shows traces and spectra combined.

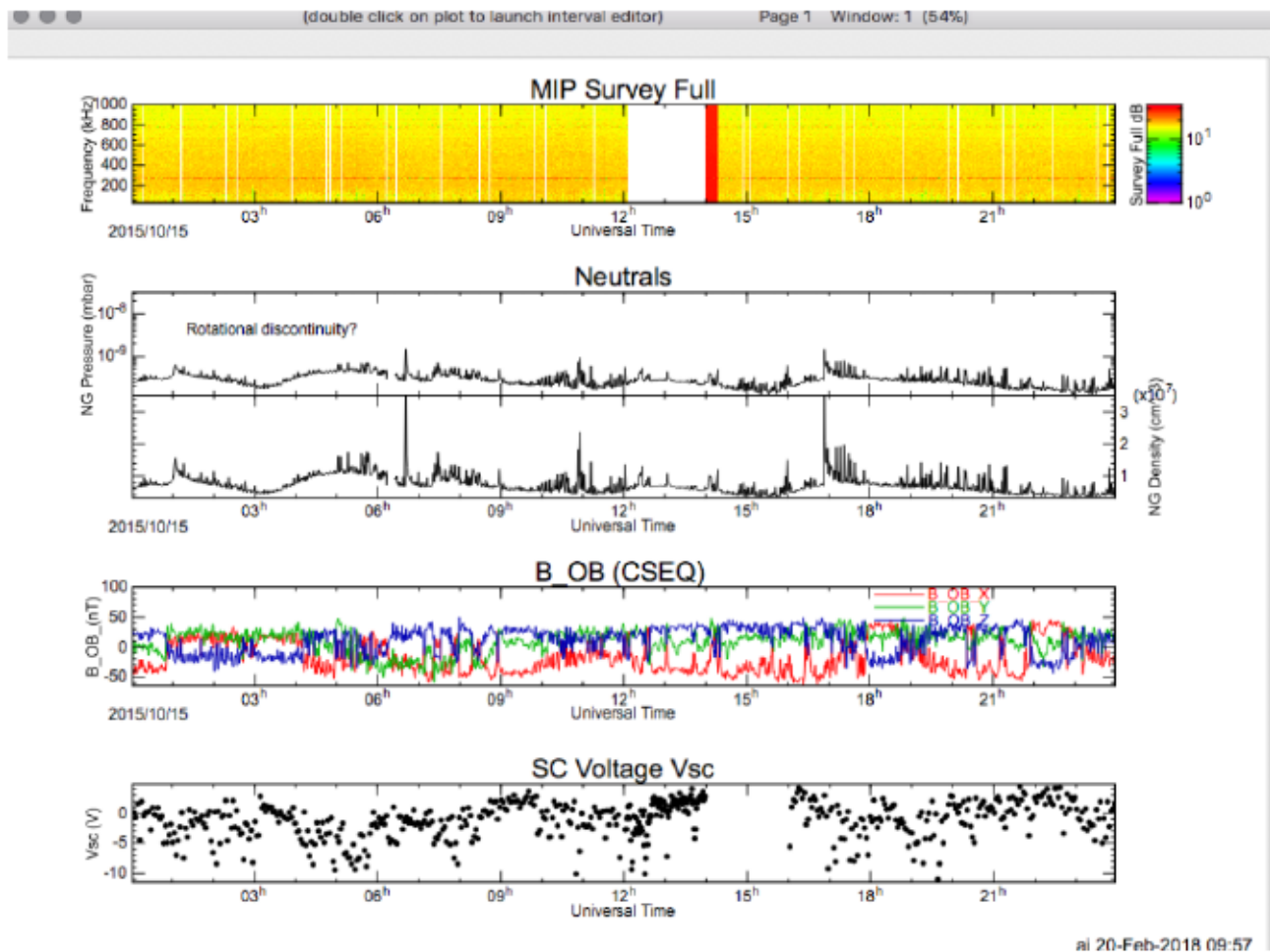
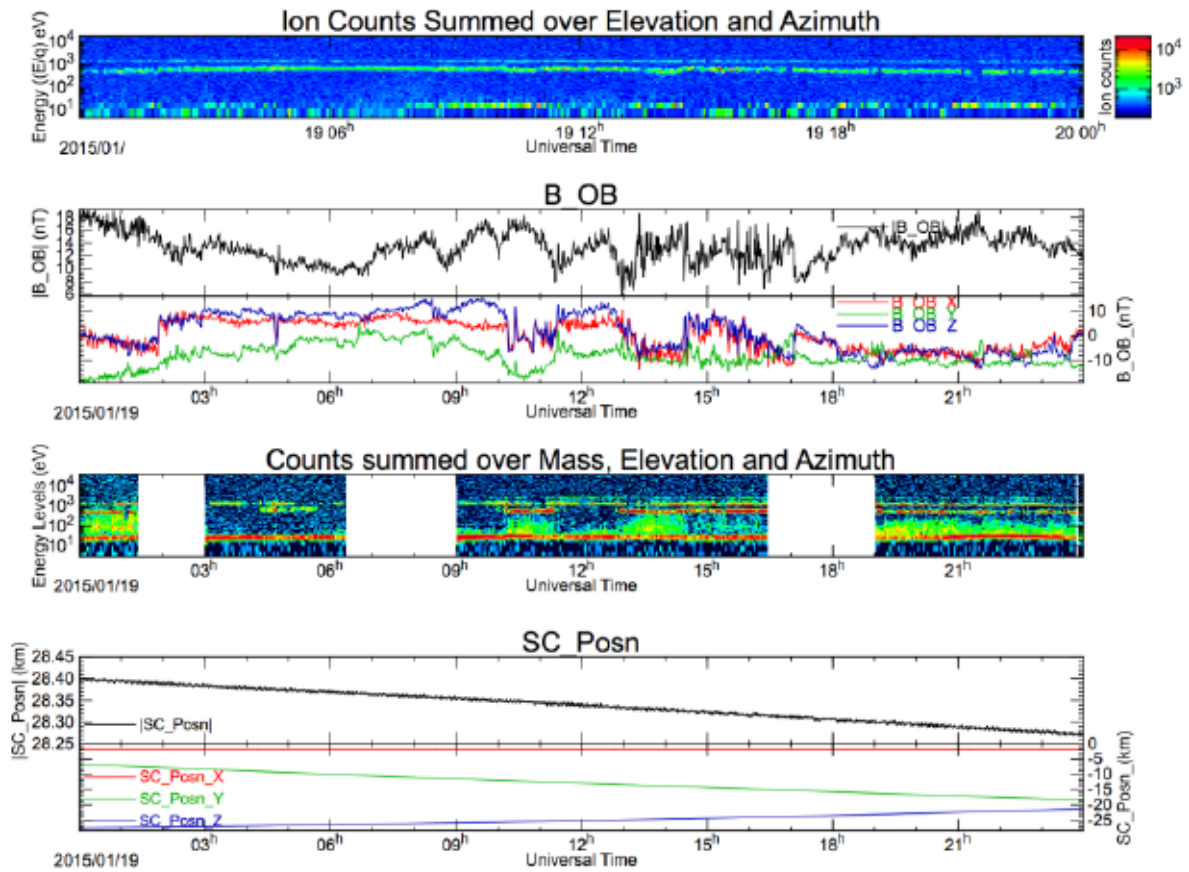


Figure 4.5: From top to bottom: RPC-MIP frequency, Rosetta Orbiter Spectrometer for Ion and Neutral Analysis (ROSINA)-Comet Pressure Sensor (COPS) neutral pressure and total number density and RPC-MAG magnetic field components in the CSEQ reference frame.

For comparison, the same data as the AMDA plot (Figure 4.3) is shown using QSAS, from January 19, 2015 on Figure 4.6.



aj 28-Feb-2018 12:08

Figure 4.6: Plots of IES, MAG and ICA data with spacecraft position (from MAG files). Same as Figure 4.3 using QSAS.

Higher dimensional data may be viewed in 2D and 3D as polar or relief plots or as slices through a 3-dimensional distribution. The data input slots in all plot windows allow for sum, average, slice or sub-sample over any of the dimensions to reduce higher dimensional data to be suitable for the selected plot type (see Figure 4.7–4.10).

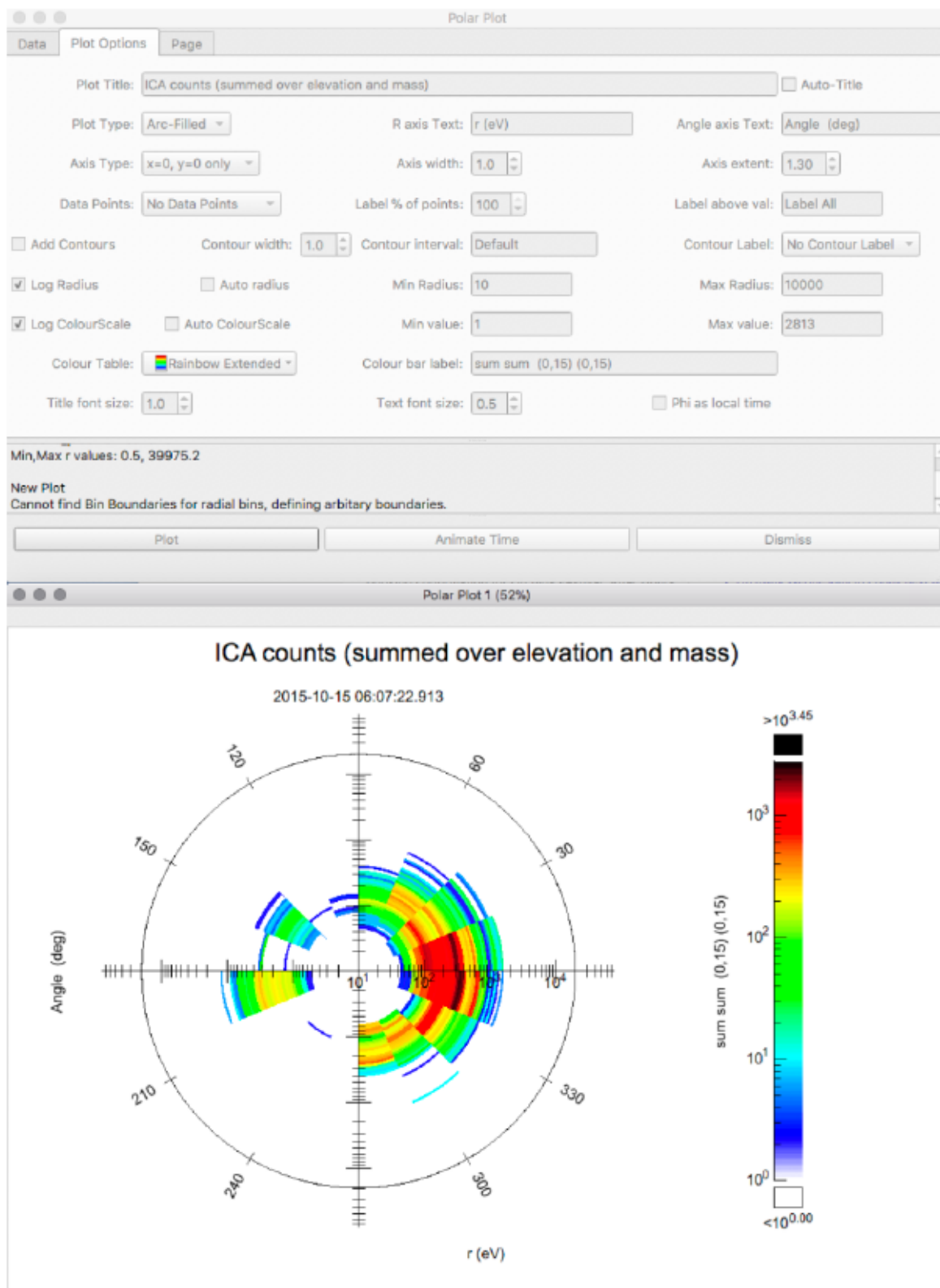


Figure 4.7: Polar plot of ICA data

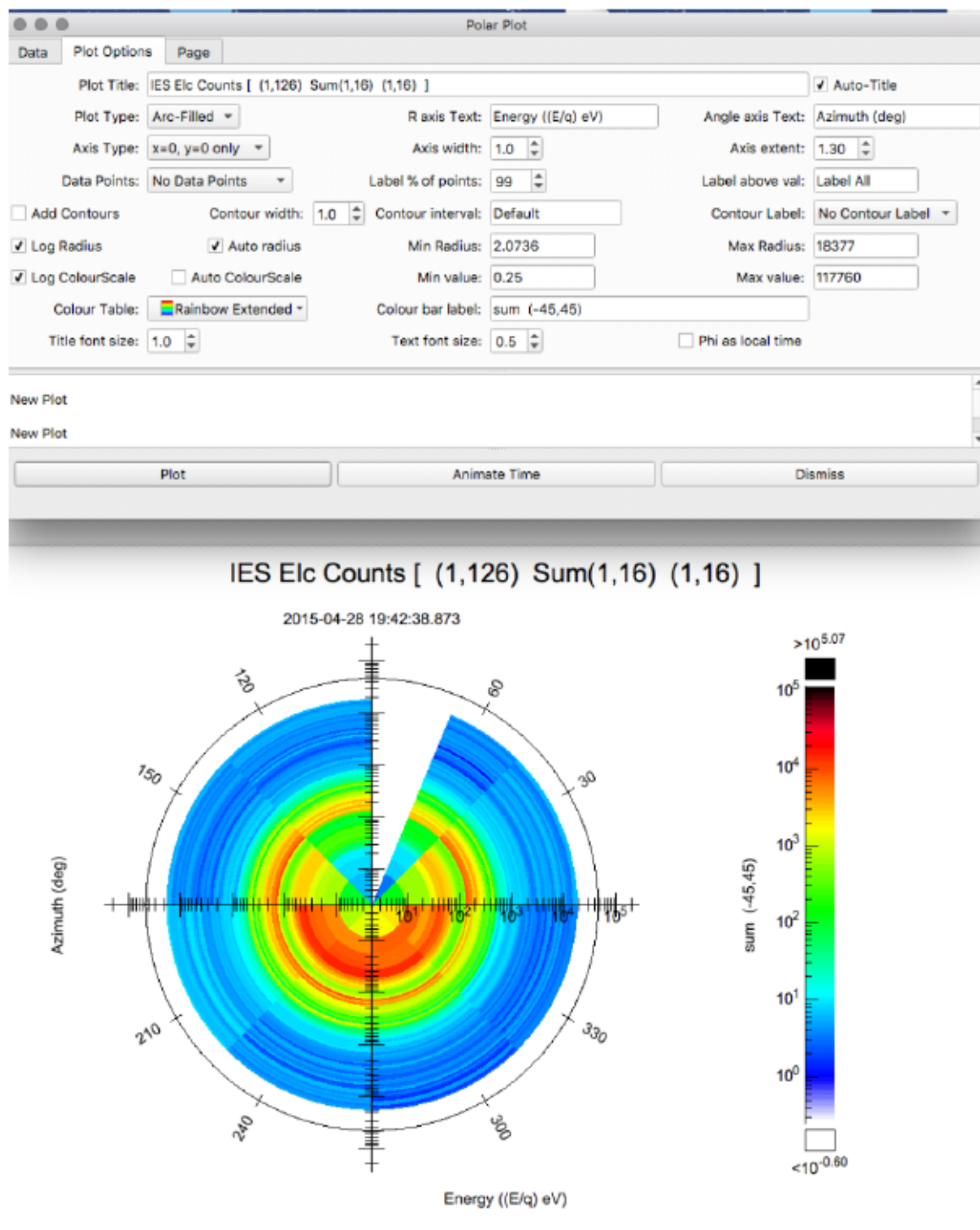


Figure 4.8: Polar plot of IES Electron data

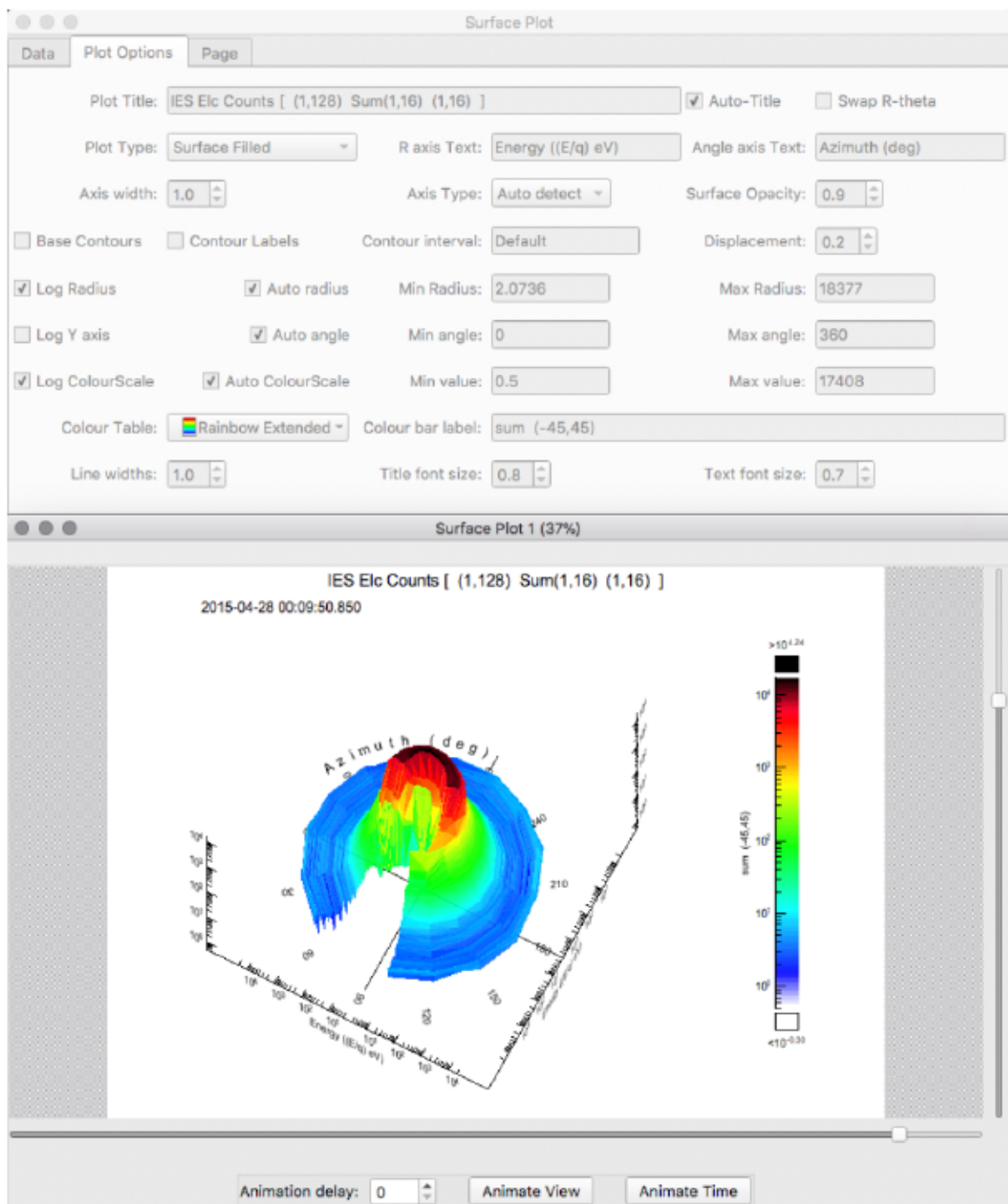


Figure 4.9: The same IES data as Fig. 4.8 in an interactive surface plot

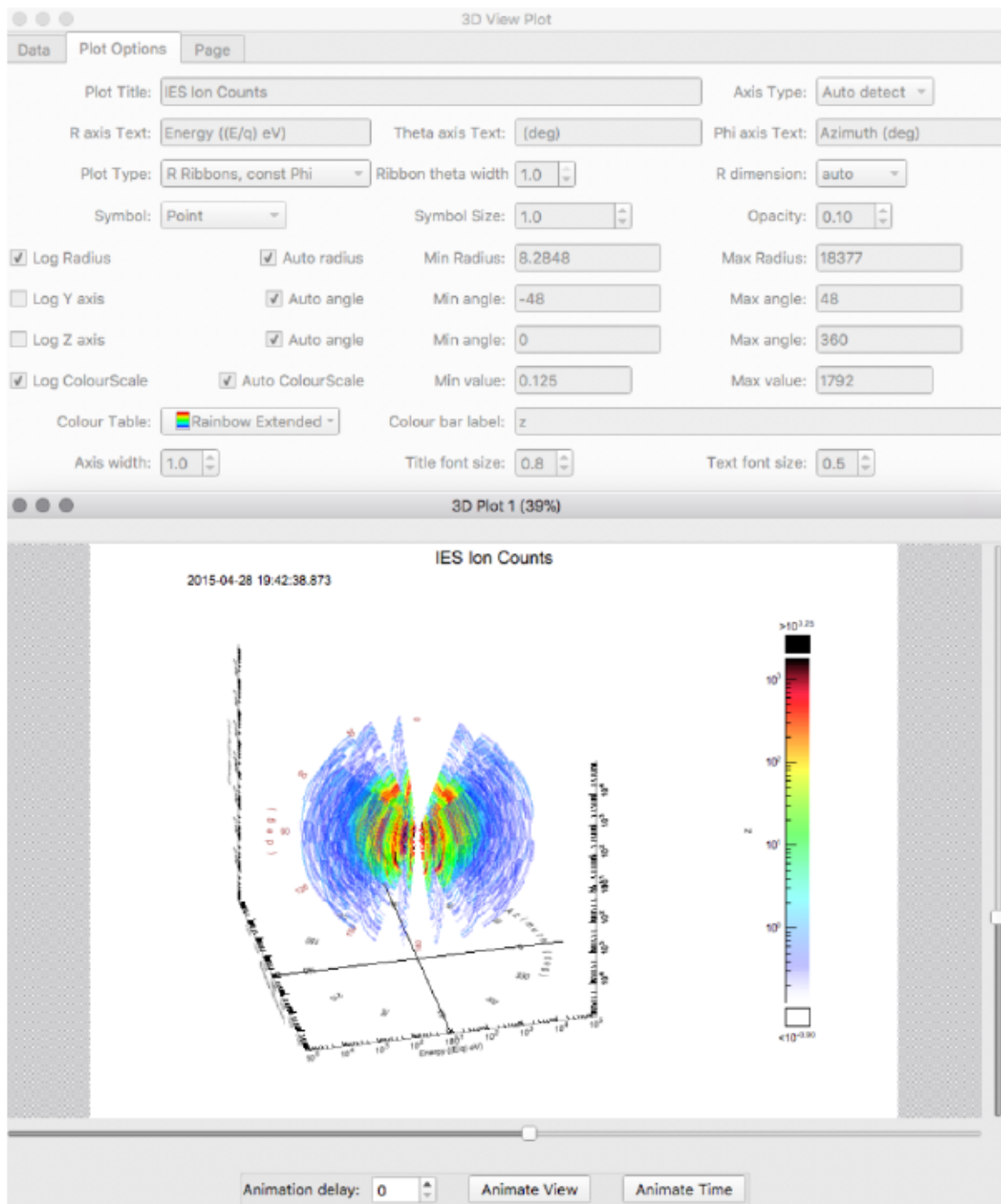


Figure 4.10: 3D interactive plot of the same IES data as Fig. 4.8 without summing over elevation

QSAS can also perform mathematical operations, combining data from different instruments to construct new parameters. The calculation shown in Fig. 4.11 (for plasma beta) was constructed by drag-and-drop and click-and-place operations. Note that the pressures are converted to nPa before division to ensure the result is dimensionless. Common fundamental constants are provided on the Working List, but note in this example the 'Temperature' is provided in Joules, so the Boltzmann constant is not needed. Calculation chains can be saved for later re-use. QSAS is units aware, and conversion to the same units is automatic for addition and subtraction, so, for example, the total pressure can be created by adding electron and magnetic pressures and then converting to nPa afterwards. All QSAS data objects know what units they are in and how to convert to base SI units.

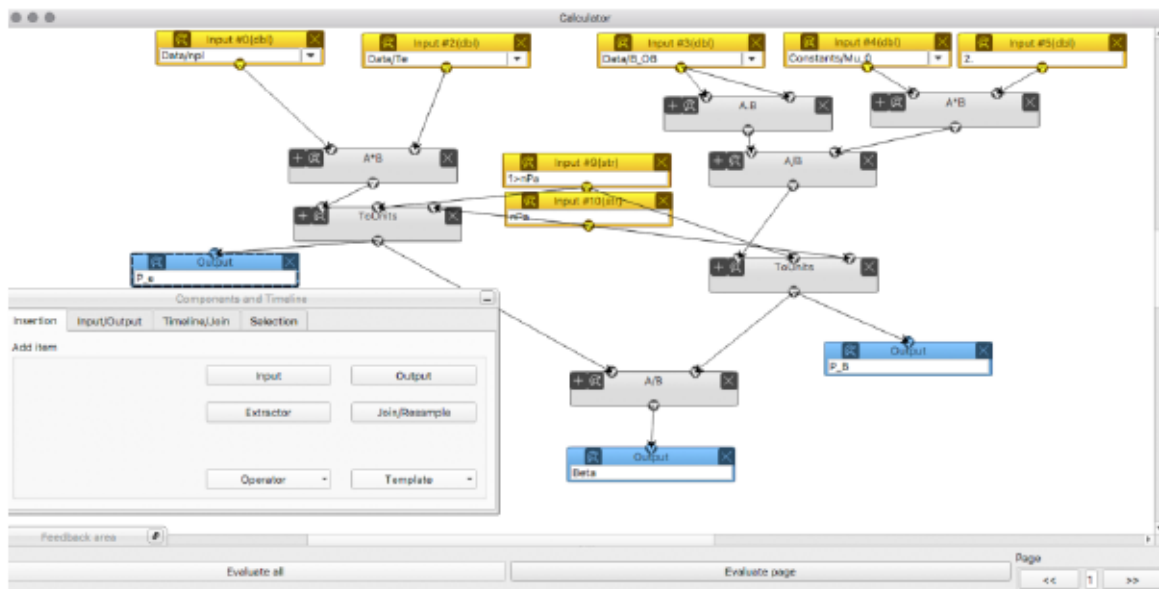
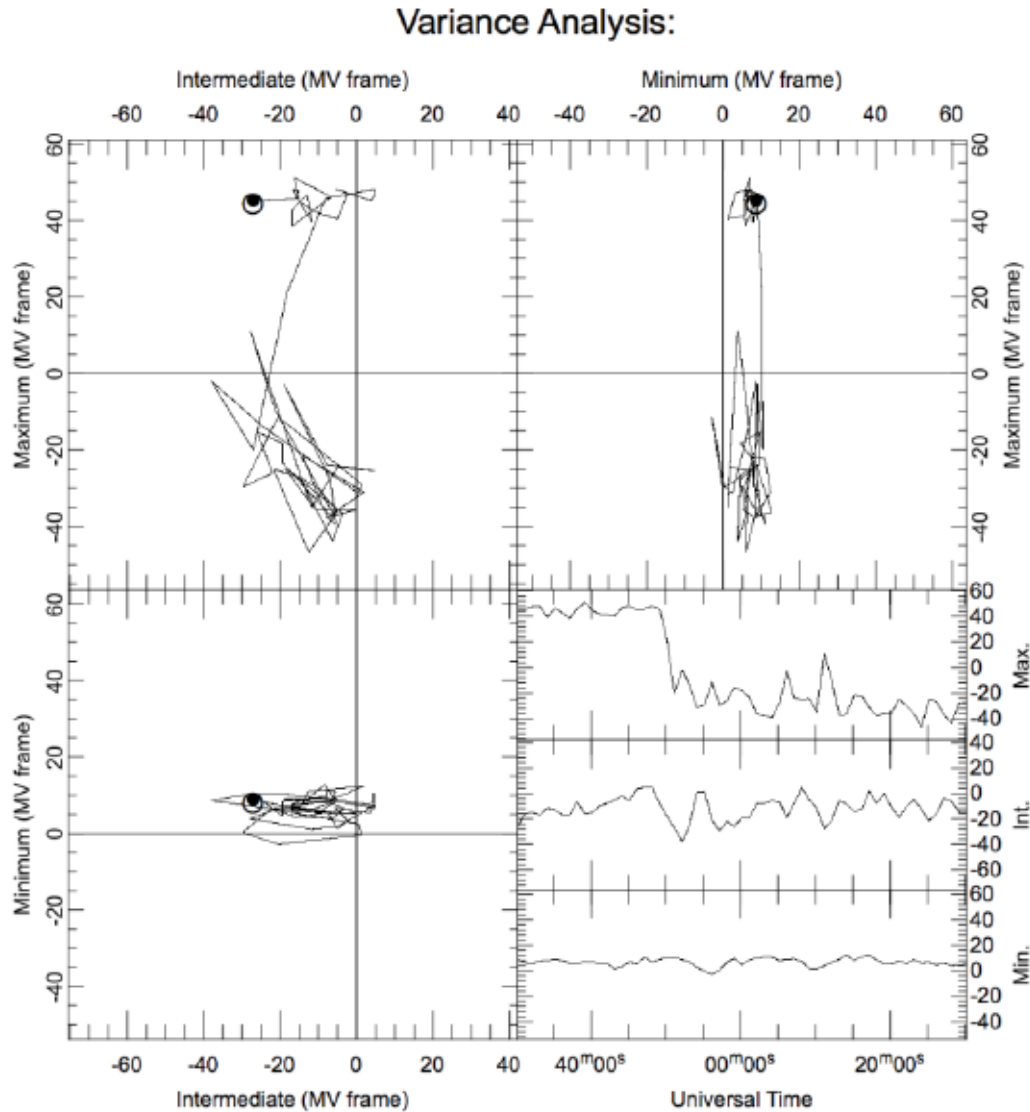


Figure 4.11: The Calculator window showing a calculation for plasma beta from particle, magnetic field data and built in constants.

QSAS can save and re-load specific calculator and plot designs. It can also run user created plugins for specialised analysis, and many plugins are shipped with QSAS, such as Power Spectrum and Minimum Variance (Figure 4.12) analysis. A full session and its data can be saved and reloaded or emailed to another QSAS user.



Time Interval (UT): 2015-10-15 00:30:09.520 - 01:30:09.520

Units: nT Frame: CSEQ_xyz

λ	Direction
9.55	(-0.687, 0.169, -0.707)
85.4	(0.225, -0.876, -0.427)
1.22e+03	(-0.691, -0.452, 0.564)

Figure 4.12: Result of QSAS Minimum Variance analysis on MAG data plotted as a hodogram and components, data rotated into MV frame.

QSAS can read several data formats, but to ensure compliant metadata is available to it, the option to download data from the PSA in CDF format should be used. QSAS will use this metadata to ensure units and coordinate frames are correct when manipulating data.

4.4 Matlab code for visualisation of illumination maps

A MATLAB has been developed by Arnaud Beth in order to exploit the ASCII files available on the PSA and to ease the visualisation. The code is available on request. However, we provide some MATLAB lines in order to use and visualise the illumination for one case.

For this example, we look the comet from the spacecraft at a latitude SLat of 45° and a longitude SLon of 30° . The subsolar latitude SSLat is 0° and the subsolar longitude SSLon is 0° . The mandatory files are the shape model CSHP_DV_130_01_LORES_OBJ.OBJ and the ASCII file ASCII_000_090.TAB for this example. For other configuration, the user has to download the corresponding file.

```

1 figure('Position',[0 0 800 800],'outerPosition',[0 0 800 800]); %creat a ...
   window for display
2
3 %Number of nodes and facets of the shape model, they are fixed. N_Faces ...
   corresponds also to the length of the ASCII file.
4 N_Nodes=52098;
5 N_Faces=104192;
6 %Predefining those values allows to save computing time.
7
8 SSLat=0; %Subsolar Latitude (in deg) to be modified accordingly
9 SSLon=0; %Subsolar Longitude (in deg) to be modified accordingly
10
11 SLat=45; %Spacecraft Latitude (in deg) to be modified accordingly
12 SLon=30; %Spacecraft Longitude (in deg) to be modified accordingly
13
14 M=importdata('CSHP_DV_130_01_LORES_OBJ.OBJ');
15
16 V=M.data(1:N_Nodes,:); %The first N_Nodes lines contain the position ...
   in 3D of each node
17 F=M.data(N_Nodes+1:end,:); %The remaining N_Faces lines give the which ...
   nodes have to be linked in order to create a facet
18
19 %ASCII files are defined by the subsolar colatitude
20
21 A=importdata(['ASCII_' num2str(SSLon,'%03.0f') '_' ...
   num2str(90-SSLon,'%03.0f') '.TAB']); %Read the corresponding ASCII ...
   (.TAB) file located in the work directory
22 %Formatting '%03.0f' rounds towards the closest integer with leading ...
   zeroes such that here it reads ASCII_000_090.TAB
23
24 trisurf(F,V(:,1),V(:,2),V(:,3),A,'linestyle','none')
25 %'none' for 'linestyle' prevents drawing lines for the edges of each facet
26
27 colormap gray
28 caxis([0 1])
29 axis off %remove the axes
30 colorbar('FontSize',20) %add the colorbar
31
32 view([90+SLon SLat]) %Put the camera at the spacecraft oriented towards ...
   the centre of mass
33 axis equal

```

Those lines generate Fig. 4.13.

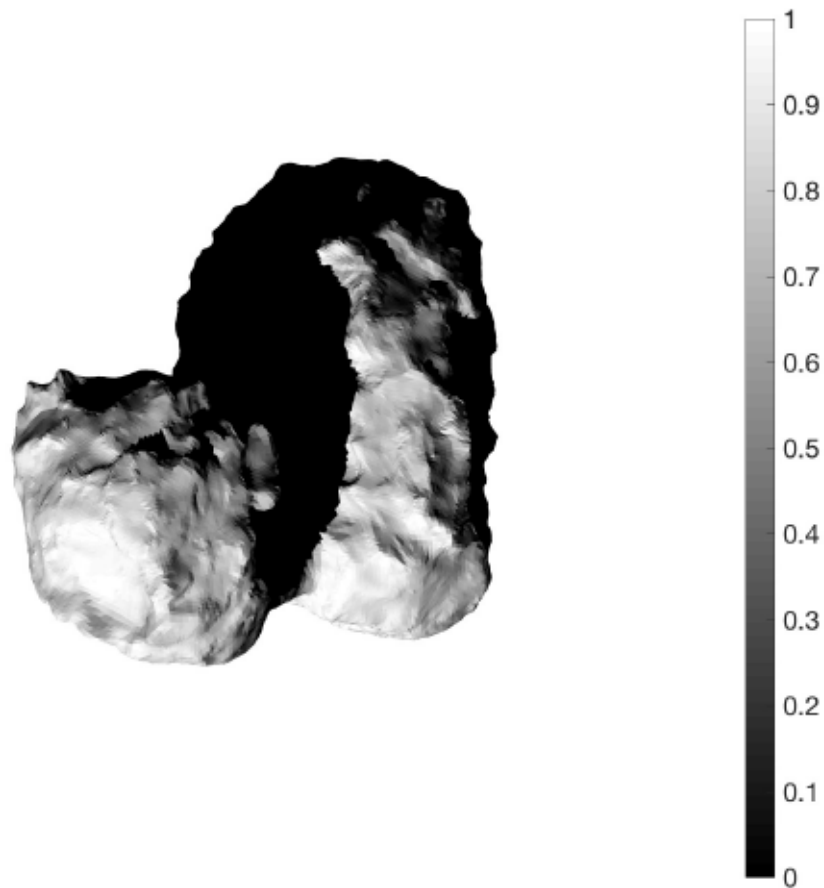


Figure 4.13: Example of image generated with MATLAB with the provided lines of code.

From the TIME2SUN.TAB file, part of this dataset, it is possible to obtain the correspondence between time of the mission and the location of the subsolar point. However, TIME2SUN.TAB does not include the spacecraft position and it is up to the user to obtain from a different source the position of the spacecraft in the rotating fixed frame or from SPICE.

Bibliography

- André, M. et al. (2017). "Lower hybrid waves at comet 67P/Churyumov–Gerasimenko". In: *Monthly Notices of the Royal Astronomical Society* 469.Suppl_2, S29–S38. DOI: 10.1093/mnras/stx868.
- Auster, H.-U. et al. (2015). "The nonmagnetic nucleus of comet 67P/Churyumov-Gerasimenko". In: *Science* 349.6247. ISSN: 0036-8075. DOI: 10.1126/science.aaa5102.
- Behar, E. et al. (2016a). "Mass loading at 67P/Churyumov-Gerasimenko: A case study". In: *Geophysical Research Letters* 43.4, pp. 1411–1418. DOI: 10.1002/2015GL067436.
- Behar, E. et al. (2016b). "Mass-loading of the solar wind at 67P/Churyumov-Gerasimenko – Observations and modelling". In: *A&A* 596, A42. DOI: 10.1051/0004-6361/201628797.
- Behar, E. et al. (2017). "The birth and growth of a solar wind cavity around a comet – Rosetta observations". In: *Monthly Notices of the Royal Astronomical Society* 469.Suppl_2, S396–S403. DOI: 10.1093/mnras/stx1871.
- Berčič, L. et al. (2018). "Cometary ion dynamics observed in the close vicinity of comet 67P/Churyumov-Gerasimenko during the intermediate activity period". In: *A&A* 613, A57. DOI: 10.1051/0004-6361/201732082.
- Broiles, T. W. et al. (2015). "Rosetta observations of solar wind interaction with the comet 67P/Churyumov-Gerasimenko". In: *A&A* 583, A21. DOI: 10.1051/0004-6361/201526046.
- Broiles, T. W. et al. (2016). "Characterizing cometary electrons with kappa distributions". In: *Journal of Geophysical Research: Space Physics* 121.8, pp. 7407–7422. DOI: 10.1002/2016JA022972.
- Burch, J. L. et al. (2007). "RPC-IES: The Ion and Electron Sensor of the Rosetta Plasma Consortium". In: *Space Science Reviews* 128.1, pp. 697–712. ISSN: 1572-9672. DOI: 10.1007/s11214-006-9002-4.
- Burch, J. L. et al. (2015). "Charge exchange in cometary coma: Discovery of H⁻ ions in the solar wind close to comet 67P/Churyumov-Gerasimenko". In: *Geophysical Research Letters* 42.13, pp. 5125–5131. DOI: 10.1002/2015GL064504.
- Carr, C. et al. (2007). "RPC: The Rosetta Plasma Consortium". In: *Space Science Reviews* 128.1, pp. 629–647. ISSN: 1572-9672. DOI: 10.1007/s11214-006-9136-4.
- Clark, G. et al. (2015). "Suprathermal electron environment of comet 67P/Churyumov-Gerasimenko: Observations from the Rosetta Ion and Electron Sensor". In: *A&A* 583, A24. DOI: 10.1051/0004-6361/201526351.
- Edberg, N. J. T. et al. (2009). "Simultaneous measurements of Martian plasma boundaries by Rosetta and Mars Express". In: *Planetary and Space Science* 57.8. European Mars Science and Exploration Conference (EMSEC), pp. 1085–1096. ISSN: 0032-0633. DOI: <https://doi.org/10.1016/j.pss.2008.10.016>.
- Edberg, N. J. T. et al. (2015). "Spatial distribution of low-energy plasma around comet 67P/CG from Rosetta measurements". In: *Geophysical Research Letters* 42.11, pp. 4263–4269. DOI: 10.1002/2015GL064233.
- Engelhardt, I. A. D. et al. (2018a). "Cold electrons at comet 67P/Churyumov-Gerasimenko". In: *A&A* 616, A51. DOI: 10.1051/0004-6361/201833251.

- Engelhardt, I. A. D. et al. (2018b). "Plasma density structures at comet 67P/Churyumov–Gerasimenko". In: *Monthly Notices of the Royal Astronomical Society* 477.1, pp. 1296–1307. DOI: 10.1093/mnras/sty765.
- Eriksson, A. I. et al. (2007). "RPC-LAP: The Rosetta Langmuir Probe Instrument". In: *Space Science Reviews* 128.1, pp. 729–744. ISSN: 1572-9672. DOI: 10.1007/s11214-006-9003-3.
- Eriksson, A. I. et al. (2017). "Cold and warm electrons at comet 67P/Churyumov-Gerasimenko". In: *A&A* 605, A15. DOI: 10.1051/0004-6361/201630159.
- Galand, M. et al. (2016). "Ionospheric plasma of comet 67P probed by Rosetta at 3 au from the Sun". In: *Monthly Notices of the Royal Astronomical Society* 462.Suppl_1, S331–S351. DOI: 10.1093/mnras/stw2891.
- Gilet, N. et al. (2017). "Electrostatic Potential Radiated by a Pulsating Charge in a Two-Electron Temperature Plasma". In: *Radio Science* 52.11, pp. 1432–1448. DOI: 10.1002/2017RS006294.
- Glassmeier, K.-H. et al. (2007). "RPC-MAG The Fluxgate Magnetometer in the ROSETTA Plasma Consortium". In: *Space Science Reviews* 128.1, pp. 649–670. ISSN: 1572-9672. DOI: 10.1007/s11214-006-9114-x.
- Glassmeier, K.-H. (2017). "Interaction of the solar wind with comets: a Rosetta perspective". In: *Philosophical Transactions of the Royal Society of London A: Mathematical, Physical and Engineering Sciences* 375.2097. ISSN: 1364-503X. DOI: 10.1098/rsta.2016.0256.
- Goetz, C. et al. (2016a). "First detection of a diamagnetic cavity at comet 67P/Churyumov-Gerasimenko". In: *A&A* 588, A24. DOI: 10.1051/0004-6361/201527728.
- Goetz, C. et al. (2016b). "Structure and evolution of the diamagnetic cavity at comet 67P/Churyumov–Gerasimenko". In: *Monthly Notices of the Royal Astronomical Society* 462.Suppl_1, S459–S467. DOI: 10.1093/mnras/stw3148.
- Goetz, C. et al. (2017). "Evolution of the magnetic field at comet 67P/Churyumov–Gerasimenko". In: *Monthly Notices of the Royal Astronomical Society* 469.Suppl_2, S268–S275. DOI: 10.1093/mnras/stx1570.
- Goldstein, R. et al. (2015). "The Rosetta Ion and Electron Sensor (IES) measurement of the development of pickup ions from comet 67P/Churyumov-Gerasimenko". In: *Geophysical Research Letters* 42.9, pp. 3093–3099. DOI: 10.1002/2015GL063939.
- Goldstein, R. et al. (2017). "Two years of solar wind and pickup ion measurements at comet 67P/Churyumov–Gerasimenko". In: *Monthly Notices of the Royal Astronomical Society* 469.Suppl_2, S262–S267. DOI: 10.1093/mnras/stx1571.
- Grün, E. et al. (2016). "The 2016 Feb 19 outburst of comet 67P/CG: an ESA Rosetta multi-instrument study". In: *Monthly Notices of the Royal Astronomical Society* 462.Suppl_1, S220–S234. DOI: 10.1093/mnras/stw2088.
- Hajra, R. et al. (2017). "Impact of a cometary outburst on its ionosphere - Rosetta Plasma Consortium observations of the outburst exhibited by comet 67P/Churyumov-Gerasimenko on 19 February 2016". In: *A&A* 607, A34. DOI: 10.1051/0004-6361/201730591.
- Hansen, K. C. et al. (2016). "Evolution of water production of 67P/Churyumov-Gerasimenko: an empirical model and a multi-instrument study". In: *Monthly Notices of the Royal Astronomical Society* 462.Suppl_1, S491–S506. DOI: 10.1093/mnras/stw2413.
- Heinisch, P. et al. (2016). "Attitude reconstruction of ROSETTA's Lander PHILAE using two-point magnetic field observations by ROMAP and RPC-MAG". In: *Acta Astronautica* 125. Rosetta and Philae at comet 67P/Churyumov-Gerasimenko, pp. 174–182. ISSN: 0094-5765. DOI: <https://doi.org/10.1016/j.actaastro.2015.12.002>.
- Heinisch, P. et al. (2017). "Reconstruction of the flight and attitude of Rosetta's lander Philae". In: *Acta Astronautica* 140, pp. 509–516. ISSN: 0094-5765. DOI: <https://doi.org/10.1016/j.actaastro.2017.09.017>.

- Henri, P. et al. (2017). "Diamagnetic region(s): structure of the unmagnetized plasma around Comet 67P/CG". In: *Monthly Notices of the Royal Astronomical Society* 469.Suppl_2, S372–S379. DOI: 10.1093/mnras/stx1540.
- Heritier, K. L. et al. (2017). "Vertical structure of the near-surface expanding ionosphere of comet 67P probed by Rosetta". In: *Monthly Notices of the Royal Astronomical Society* 469.Suppl_2, S118–S129. DOI: 10.1093/mnras/stx1459.
- Heritier, K. L. et al. (2018). "Plasma source and loss at comet 67P during the Rosetta mission". In: *A&A*. DOI: 0004-6361/201832881.
- Hoang, M. et al. (2017). "The heterogeneous coma of comet 67P/Churyumov-Gerasimenko as seen by ROSINA: H₂O, CO₂, and CO from September 2014 to February 2016". In: *A&A* 600, A77. DOI: 10.1051/0004-6361/201629900.
- Johansson, F. L. et al. (2016). "Simulations of the electrostatic potential of Rosetta at comet 67P". In: *Proceedings of the 14th Spacecraft Charging Technology Conference*. European Space Agency.
- Johansson, F. L. et al. (2017). "Rosetta photoelectron emission and solar ultraviolet flux at comet 67P". In: *Monthly Notices of the Royal Astronomical Society* 469.Suppl_2, S626–S635. DOI: 10.1093/mnras/stx2369.
- Karlsson, T. et al. (2017). "Rosetta measurements of lower hybrid frequency range electric field oscillations in the plasma environment of comet 67P". In: *Geophysical Research Letters* 44.4, pp. 1641–1651. DOI: 10.1002/2016GL072419.
- Koenders, C. et al. (2016a). "Low-frequency waves at comet 67P/Churyumov-Gerasimenko - Observations compared to numerical simulations". In: *A&A* 594, A66. DOI: 10.1051/0004-6361/201628803.
- Koenders, C. et al. (2016b). "Magnetic field pile-up and draping at intermediately active comets: results from comet 67P/Churyumov-Gerasimenko at 2.0 AU". In: *Monthly Notices of the Royal Astronomical Society* 462.Suppl_1, S235–S241. DOI: 10.1093/mnras/stw2480.
- Madanian, H. et al. (2016). "Suprathermal electrons near the nucleus of comet 67P/Churyumov-Gerasimenko at 3 AU: Model comparisons with Rosetta data". In: *Journal of Geophysical Research: Space Physics* 121.6, pp. 5815–5836. DOI: 10.1002/2016JA022610.
- Mandt, K. E. et al. (2016). "RPC observation of the development and evolution of plasma interaction boundaries at 67P/Churyumov-Gerasimenko". In: *Monthly Notices of the Royal Astronomical Society* 462.Suppl_1, S9–S22. DOI: 10.1093/mnras/stw1736.
- Nicolaou, G. et al. (2017). "Energy-angle dispersion of accelerated heavy ions at 67P/Churyumov-Gerasimenko: implication in the mass-loading mechanism". In: *Monthly Notices of the Royal Astronomical Society* 469.Suppl_2, S339–S345. DOI: 10.1093/mnras/stx1621.
- Nilsson, H. et al. (2007). "RPC-ICA: The Ion Composition Analyzer of the Rosetta Plasma Consortium". In: *Space Science Reviews* 128.1, pp. 671–695. ISSN: 1572-9672. DOI: 10.1007/s11214-006-9031-z.
- Nilsson, H. et al. (2015a). "Birth of a comet magnetosphere: A spring of water ions". In: *Science* 347.6220. ISSN: 0036-8075. DOI: 10.1126/science.aaa0571.
- Nilsson, H. et al. (2015b). "Evolution of the ion environment of comet 67P/Churyumov-Gerasimenko - Observations between 3.6 and 2.0 AU". In: *A&A* 583, A20. DOI: 10.1051/0004-6361/201526142.
- Nilsson, H. et al. (2017). "Evolution of the ion environment of comet 67P during the Rosetta mission as seen by RPC-ICA". In: *Monthly Notices of the Royal Astronomical Society* 469.Suppl_2, S252–S261. DOI: 10.1093/mnras/stx1491.
- Odelstad, E. et al. (2015). "Evolution of the plasma environment of comet 67P from spacecraft potential measurements by the Rosetta Langmuir probe instrument". In: *Geophysical Research Letters* 42.23, pp. 10, 126–10, 134. DOI: 10.1002/2015GL066599.

- Odelstad, E. et al. (2017). "Measurements of the electrostatic potential of Rosetta at comet 67P". In: *Monthly Notices of the Royal Astronomical Society* 469.Suppl_2, S568–S581. DOI: 10.1093/mnras/stx2232.
- Odelstad, E. et al. (2018). "Ion velocity and electron temperature inside and around the diamagnetic cavity of comet 67P". In: *Journal of Geophysical Research: Space Physics* 0.ja. DOI: 10.1029/2018JA025542.
- Richter, I. et al. (2015). "Observation of a new type of low-frequency waves at comet 67P/Churyumov-Gerasimenko". In: *Annales Geophysicae* 33.8, pp. 1031–1036. DOI: 10.5194/angeo-33-1031-2015.
- Richter, I. et al. (2016). "Two-point observations of low-frequency waves at 67P/Churyumov-Gerasimenko during the descent of PHILAE: comparison of RPCMAG and ROMAP". In: *Annales Geophysicae* 34.7, pp. 609–622. DOI: 10.5194/angeo-34-609-2016.
- Simon Wedlund, C. et al. (2016). "The atmosphere of comet 67P/Churyumov-Gerasimenko diagnosed by charge-exchanged solar wind alpha particles". In: *A&A* 587, A154. DOI: 10.1051/0004-6361/201527532.
- Stenberg Wieser, G. et al. (2017). "Investigating short-time-scale variations in cometary ions around comet 67P". In: *Monthly Notices of the Royal Astronomical Society* 469.Suppl_2, S522–S534. DOI: 10.1093/mnras/stx2133.
- Trotignon, J. G. et al. (2007). "RPC-MIP: the Mutual Impedance Probe of the Rosetta Plasma Consortium". In: *Space Science Reviews* 128.1, pp. 713–728. ISSN: 1572-9672. DOI: 10.1007/s11214-006-9005-1.
- Tzou, Chia-Yu (2017). "Calibrations of ROSINA-COPS and Observations at Comet 67P/Churyumov-Gerasimenko". e-Dissertation (edbe). PhD thesis. Universität Bern.
- Vigren, E. et al. (2016). "Model–Observation Comparisons of Electron Number Densities in the Coma of 67P/Churyumov-Gerasimenko during January 2015". In: *The Astronomical Journal* 152.3, p. 59.
- Vigren, E. et al. (2017). "Effective ion speeds at $\sim 200 - 250$ km from comet 67P/Churyumov-Gerasimenko near perihelion". In: *Monthly Notices of the Royal Astronomical Society* 469.Suppl_2, S142–S148. DOI: 10.1093/mnras/stx1472.
- Volwerk, M. et al. (2016). "Mass-loading, pile-up, and mirror-mode waves at comet 67P/Churyumov-Gerasimenko". In: *Annales Geophysicae* 34.1, pp. 1–15. DOI: 10.5194/angeo-34-1-2016.
- Volwerk, M. et al. (2017). "Current sheets in comet 67P/Churyumov-Gerasimenko's coma". In: *Journal of Geophysical Research: Space Physics* 122.3, pp. 3308–3321. DOI: 10.1002/2017JA023861.
- Volwerk, M. et al. (2018). "A tail like no other - The RPC-MAG view of Rosettas tail excursion at comet 67P/Churyumov-Gerasimenko". In: *A&A* 614, A10. DOI: 10.1051/0004-6361/201732198.
- Yang, L. et al. (2016). "Observations of high-plasma density region in the inner coma of 67P/Churyumov-Gerasimenko during early activity". In: *Monthly Notices of the Royal Astronomical Society* 462.Suppl_1, S33–S44. DOI: 10.1093/mnras/stw2046.